SYNTHESIS AND CHARACTERIZATION OF MESOPOROUS $LiMPO_4$ (Mn(II), Fe(II), Co(II), AND Ni(II))

A THESIS SUBMITTED TO

THE GRADUATE SCHOOL OF ENGINEERING AND SCIENCE

OF BILKENT UNIVERSITY

IN PARTIAL FULFILLMENT OF THE REQUIREMENTS FOR

THE DEGREE OF

MASTER OF SCIENCE

IN

CHEMISTRY

By

Tuluhan Olcayto Çolak

March 2018

SYNTHESIS AND CHARACTERIZATION OF MESOPOROUS $LiMPO_4$ (Mn(II), Fe(II), Co(II), AND Ni(II))

By Tuluhan Olcayto Çolak

March 2018

We certify that we have read this thesis and that in our opinion it is fully adequate, in scope and in quality, as a thesis for a degree of Master of Science.

_____

Ömer Dağ (Advisor)

_____

Ayşen Yılmaz

_____

Ferdi Karadaş

Approved for the Graduate School of Engineering and Science:

_____

Ezhan Karaşan

Director of Graduate School

ABSTRACT

SYNTHESIS AND CHARACTERIZATION OF MESOPOROUS LITHIUM METAL PHOSPHATES ($LiMPO_4$) (M= Mn, Fe, Co, Ni)

Tuluhan Olcayto Çolak

M. S. in Chemistry

Advisor: Ömer Dağ

March 2018

Synthesis of mesoporous lithium metal phosphates have been studied extensively in past after the emerge of lithium iron phosphate as a cathode material in the lithium ion batteries. These materials are proved to be modifiable and useful in lithium ion batteries. This study encompasses synthesis and characterization of the mesoporous $LiMPO_4$ (M= Mn(II), Fe(II), Co(II), and Ni(II)) from lyotropic liquid crystalline (LLC) mesophases, utilizing a method which can be described as a modified molten salt assisted self-assembly (MASA) method. Preparation of clear solutions and LLC mesophases afterwards are quite an effortless process, once optimized, which in its order starts with the clear solution prepared for the synthesis of lithium transition metal phosphate, then the coating of the solution over glass substrate using two methods, the spin coating and drop-casting. The coated films are then calcined to fabricate the mesoporous lithium metal phosphate products. In this thesis, the mesoporous $LiMPO_4$ (M = Mn(II), Fe(II), Co(II), and Ni(II)), are synthesised using the modified MASA method using 10-lauryl ether as the soft template and characterized using multi-analytical techniques (such as FTIR, PXRD, SEM, EDX, and N_2 adsorption-desorption).

In the initial part of the thesis, the solution stability over time, pH dependence, and concentration of the ingredients were investigated. It was found that through time these solutions precipitate ranging from weeks to hours with an inverse relation with the concentration of used salts, and acid relative to the surfactant. Continued in this part, it was observed that solution stability is also dependent on pH, which was tested using LiOH instead of $LiNO_3$ as the lithium source. It was revealed that, at higher pH values, the solutions are less stable and produce more precipitate.

The solutions, prepared using Mn(II), Fe(II), Co(II), and Ni(II), were coated on glass substrates by drop-cast coating and spin coating methods. These two methods were used to determine the best method for a desired amount and morphology of the corresponding products. After testing a broad range of ingredient concentrations, using the Mn(II) system, three concentrations were selected to represent dilute, medium and concentrated ratios of salt and acid versus the surfactant. The aging and temperature dependent changes were monitored using FT-IR spectroscopy; the effect of temperature on both the formation of mesophase and the reactions taking place in the mesophase has been investigated. It appears that the temperature has some profound effects on the mesophase. The mesophase gets disordered by increasing temperature. This trend also correlates well with increasing salt concentration in the media. As the salt concentration increases the temperature required to disrupt the mesophase decreases. The FT-IR spectroscopy study shows that; significant amount of nitrate species and surfactant molecules have been removed from the media at around 160^{o}C. To remove the surfactant completely, minimum temperature of calcination determined to be 250^{o}C. Samples, prepared with low concentration solution of Mn(II) salt coated with both methods, were calcined at 250, 350, and 450^{o}C and characterized using XRD, FT-IR spectroscopy and SEM techniques. It was found that the drop-casting method is favourable over the spin coating method, because the spin coating method failed to produce the desired compound and created metal pyrophosphate instead of lithium metal phosphates.

$LiMnPO_4$, $LiFePO_4$, $LiCoPO_4$, and $LiNiPO_4$ were synthesised using drop-cast coating method and characterized by XRD, FT-IR spectroscopy, SEM, EDX, and N_2- adsorption-desorption techniques. It was found that these materials are mesoporous and have noticeable surface areas with some by-products. The pores are large and non-uniform in $LiMnPO_4$ and $LiCoPO_4$, but the pores are small (3-6 nm range) in the iron and nickel samples. The surface area also accords with observation and highest (96 m^2/g) surface area was recorded from nickel samples. The pores gradually expand with annealing the samples and becomes non-uniform all cases. The undefined crystalline phases require more work to determine their structure and more optimization to obtain the desired material.

Keywords: Mesoporous Materials, Lyotropic Liquid Crystals, Soft Templating Method, Lithium Metal Phosphate, Lithium Manganese Phosphate, Lithium Iron Phosphate, Lithium Cobalt Phosphate, Lithium Nickel Phosphate.

ÖZET

MEZOPORLU LİTYUM METAL FOSFATLARIN ($LiMPO_4$) SENTEZLERİ VE KARAKTERİZASYONLARI (M= Mn, Fe, Co, Ni)

Tuluhan Olcayto Çolak

Kimya, Yüksek Lisans

Tez Danışmanı: Ömer Dağ

Mart 2018

Lityum demir fosfatların, lityum iyon pilleri için katod malzeme olarak ortaya çıkmasının ardından, mezogözenekli lityum metal fosfat tuzları kapsamlı bir şekilde çalışıldılar. Bu malzemeler adapte edilebilir ve lityum iyon bataryalar için kullanışlı bulundular. Bu çalışma mezogözenekli $LiMPO_4$'ların (M= Mn(II), Fe(II), Co(II) ve Ni(II)) eriyik tuz yardımlı kendiliğinden oluşma (EYKO) yöntemi kullanılarak, liyotropik sıvı kristal (LSK) ara fazlarından sentezlenmelerini ve karakterizasyonlarını kapsamaktadır. Bir kere optimize edildikten sonra şeffaf çözeltilerin ve LSK'ların hazırlanması oldukça zahmetsiz bir işlemdir. Sırası ile önce şeffaf çözelti, lityum metal fosfatın sentezi için hazırlanır ardından çevirme veya damlatıp kurutma yöntemi ile cam üzerine kaplanır. Kaplanmış filmler mezogözenekli lityum metal fosfat yapmak için yakılır. Bu tezde, mezogözenekli $LiMPO_4$ (M= Mn(II), Fe(II), Co(II) ve Ni(II)) uyarlanmış EYKO metodu ve yumuşak taslak olarak 10-lauryl eter kullanılarak hazırlanmış ve çoklu analitik teknikler yardımı ile karakterize edilmiştir. (FTIR, PXRD, SEM, EDX ve N_2 adsorpsiyon-desorpsiyon).

Tezin başında çözeltilerin kararlılıkları zamana, pH'a ve derişime bağlı değişimleri incelendi. Yüzey aktif ajanın tuz ve asit miktarına olan oranına bağlı olarak çözeltilerin derişimleri ve zaman içinde çökme süreleri arasında bir ters ilişki bulundu. Bu bölümde devam edilerek, çözelti dengesinin aynı zamanda pH'a bağlı olduğu $LiNO_3$ yerine LiOH kullanılarak bulundu. Fark edildiği üzere yüksek pH değerlerinde çözeltiler daha karasız olduğu ve daha çok çökelti oluşturdu.

Mn(II), Fe(II), Co(II) ve Ni(II) kullanılarak hazırlanan çözeltiler cam üzerine çevirme ve damlatıp kurutma yöntemleri ile kaplandılar. Bu iki yöntem içinden istenilen malzemeyi, istenilen miktarda ve morfolojide veren seçildi. Mn(II) sistemi kullanılarak, geniş bir derişim aralığında deneme yapıldıktan sonra seyreltik, orta ve derişik

tuz ve aside karşı yüzey aktif ajanın oranları temsilen üç derişim seçildi. Yaşlandırma ve sıcaklığa bağlı değişimler, mezofazların oluşumu ve tepkimeler FTIR ile takip edildi. Sıcaklığın mezoyapı üzerinde ciddi bazı etkileri olduğu bulundu. Mezofaz sıcaklık artışı ile yapısal düzenini kaybettiği belirlendi. Aynı davranış biçimi tuz asit miktarlarının arttırılması sonrasında da gözlemlendi. Tuz derişimleri arttıkça, mezofazı bozmak için gereken sıcaklıkta düşmektedir. FTIR spektroskopi çalışması, ciddi miktarda nitrat türünün ve yüzey aktif ajanın moleküllerinin 160^{o}C'de ortamdan atıldıklarını tespit etmiştir. Yüzey aktif ajanını tamamen atmak için en düşük yakma sıcaklığı 250^{o}C olarak belirlenmiştir. Mn(II) tuzunun seyreltik çözeltilerinin her iki yöntem ile kaplamasından sonra elde edilen numuneler 250, 350 ve 450^{o}C'lerde yakıldılar ve XRD, FTIR ve SEM teknikleri ile karakterize edildiler. Damlatıp kurutma yönteminin, çevirme yöntemine yerine, çevirme yöntemi istenilen malzemeyi üretmede başarısız olduğu ve başka metal fosfatlar ürettiği için seçildi.

$LiMnPO_4$, $LiFePO_4$, $LiCoPO_4$ ve $LiNiPO_4$ damlatıp kurutma yöntemi ile sentezlendiler ve XRD, FTIR, SEM, EDX ve N_2 adsorpsiyon-desorpsiyon teknikleri ile karakterize edildiler. Bu malzemelerin mezogözenekli oldukları ve bazı yan ürünler ile kayda değer yüzey alanlarına sahip oldukları anlaşıldı. $LiMnPO_4$ ve $LiCoPO_4$ için gözenekler geniş ve düzensiz ancak $LiFePO_4$ ve $LiNiPO_4$ için gözeneklerin dar (3 – 6 nm) olduğu belirlendi. Yüzey alanı, yapılan gözlemlere uygun olarak en yüksek nikel numunelerinde 96 m^2/g olarak kaydedildi. Gözenekler numunelerin tavlama sıcaklıklarına bağlı olarak adım adım genişlemekte ve her durum içinde düzensiz olmaktadır. Tespit edilememiş kristal fazlar yapının tanımlanması ve istenilen malzemenin elde edilebilmesi için daha çok optimizasyon gerektirmektedir.

Anahtar kelimeler: Mezogözenekli malzemeler, Liyotropik Sıvı Kristaller, Yumuşak Taslak Yöntemi, Lityum Metal Fosfat, Lityum Mangan Fosfat, Lityum Demir Fosfat, Lityum Kobalt Fosfat, Lityum Nikel Fosfat.

Acknowledgement

I would like to thank my supervisor Ömer Dağ for his guidance and patience in this three years course of study and the writing if this thesis. He taught me the fundamentals of scientific method and guided the through the chaos and confusions I often found myself in. I thank him especially for providing a point of view that is not clouded with dogmas and mentoring on observing with an open mind. Even in the times of my hopelessness, his support has gotten me through my work and I cannot thank him enough for his patience with me.

I would like to thank my group members Işıl Uzunok, Irmak Karakaya, Assel Amirzhanova, Fadime Mert Balcı, and Nüveyre Canbolat for their friendship and company. In the years passed, with them, it was a time well spent together and I consider myself lucky to have them as friends and co-workers.

I want to thank Ezgi Yılmaz for her care on me as I wrote this thesis and prepared my presentation, for her friendship since I entered the lab as a senior and for the free food in her wedding. I would like to thank, Muammer Yusuf Yaman for his help with opening holes in my hypothesis and sense of humour that can accompany mine and I also thank the late-night snacks he seemed to be quite found of. I thank to Elif Perşembe for being my company in the long nights in the lab. I thank her for the friendship that never faded since our freshmen years, for the better and for the worse she has been there for me and with me. I would like to thank Menekşe Liman for her friendship and counselling she constantly provided without an effort to reaching for her. She was and is a pleasure to be friends with. I would like to thank Merve Balcı for being there whenever I needed a friend or whenever she wanted an overpriced coffee. I also thank her helping me with understanding the difference between a dot and a “das”. I also would like to thank my bro Satiya Vijay Kumari, for his help with many instruments, and the time and tales he shared with me.

I would like to thank my family. My parents whom always pushed me for higher goals for the better amount of time. Though they are not acquainted with my work, their support, advice and kitchen had brought me to finishing my work. I also thank my brother for the night rides and all the labour I got from him. He is a treasure to have.

Contents

List of Figures

List of Tables

CHAPTER 1

1 INTRODUCTION

There are three common states of matter known in our daily life, solid, liquid, and gas (see Figure 1.1). Three of them can be arranged in terms of molecular order, mobility, and intermolecular attractive forces. Solids have the most order among the three and has the least amount of motion and therefore the intermolecular attraction prevails in its structure, whether it would be crystalline or amorphous. In fluids, inter molecular attraction fails to hold the molecules tightly together, however it evens out with their kinetic energy, forming a state which can hold its particles together but cannot retain a shape without assistance from outside. In between the solid crystals and fluids, there is another phase called liquid crystalline phase, mesophase. In this phase, intermolecular attraction is strong enough to attain an orientation for a certain direction, however, it is also weak enough to allow fluidity.

Liquid crystalline phase is formed when the molecules form fluid structures; the phase displays an orientation of the molecules in a certain direction. The LC structures could be in anisotropic form, unlike the isotropic liquid phases. They have more structural order than liquids but less than solids. Because of this property they are also

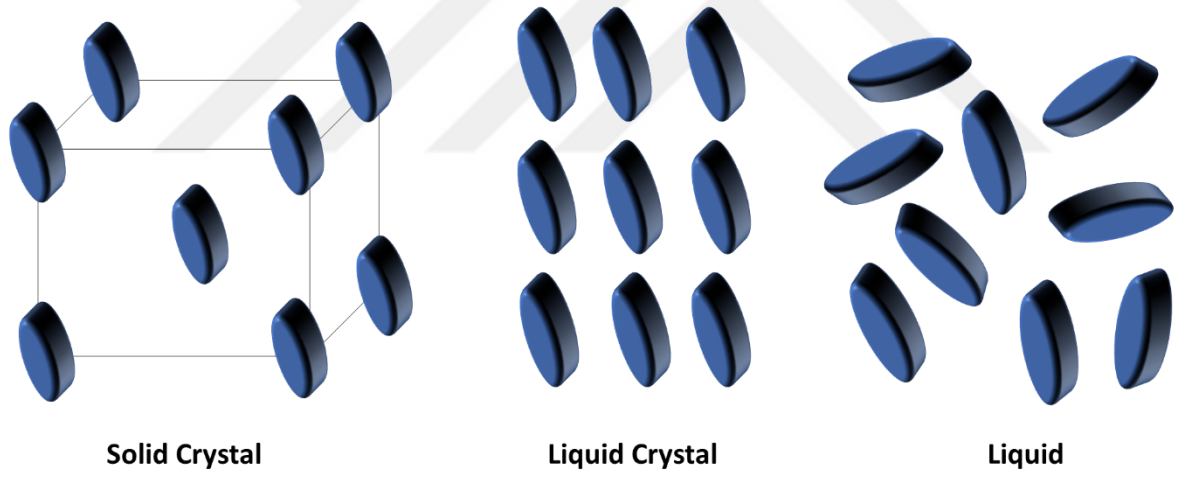

Figure 1.1 A schematic representation of solid crystal, liquid crystal, and liquid phases of a matter.

named as mesophase, an intermediate state which stands between solid and liquid, two of the three conventional states of matter. Their anisotropic structure depends on the forces among the molecules, which forms the liquid crystal [1].

Liquid crystals gather under the distinct types, thermotropic liquid crystals (TLC) and lyotropic liquid crystals (LLC). The TLC structures depend on heat for formation and they make nematic, smectic and columnar phases and usually observed in organic molecules in certain structures. There are various molecules, which can form TLC. They can be small elongated molecules, discoid compounds, long rod like molecules, polymers, and amphiphilic molecules. Small elongated molecules usually form nematic type mesophase. They are inherently anisotropic.

These structures break down with heat and thusly, they are called thermotropic [2]. The TLC are not the topic of this thesis; therefore, they will not be introduced further.

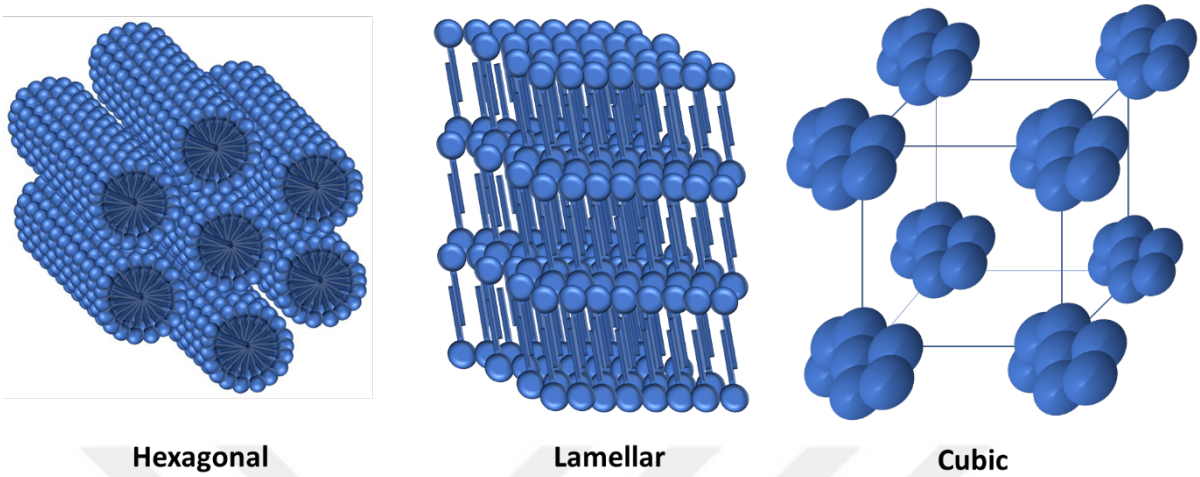

Figure 1.2 Structures those can be formed by lyotropic phases.

Amphiphilic molecules constitute a polar and apolar ends, known as surfactants. They form structures depending on the polarity of the medium, see Figure 2. The structures, they form, become the building blocks of the mesophase. Amphiphilic molecules form hexagonal cylindrical, lamellar layered, cubic, and micellar structures, depending on the surfactant and solvent concentration and known as lyotropic liquid crystals.

1.1 Lyotropic Liquid Crystals

Lyotropic liquid crystals (LLC) are formed by amphiphilic molecules. Structures formed by LLC are depending on the type and the concentration of the secondary substance which could be water [3], non-polar organic solvent [4], ionic liquids [5], and hydrated salts [6]. These amphiphilic molecules can lower the surface tension and form mesophases.

Figure 1.1.1 Generalized structure of an amphiphilic molecule.

Aside from the type o the secondary substance, the main parameters controlling the structures, formed by LLC, are temperature and concentration. In a water – surfactant system for example, at lower concentrations amphiphilic Molecules dissolve in water and stay separate. As the concentration increases, these molecules start to form various structures form simple micelles to hexagonal tubular formations.

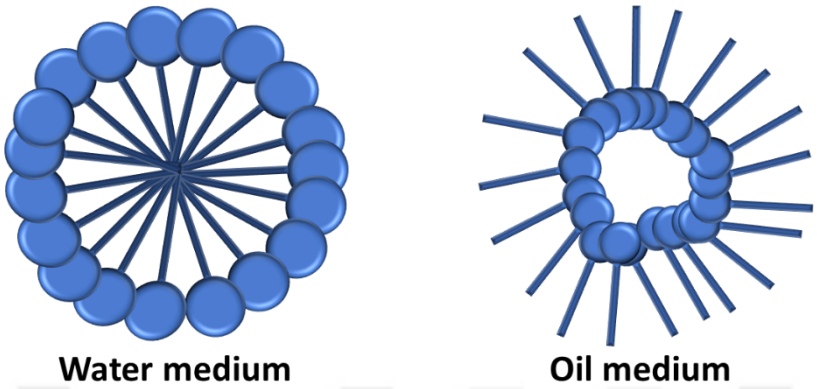

Figure 1.1.2 Diagram for micellar structures formed in polar and non-polar mediums.

[1]Depending on the solvent, the amphiphilic molecules arrange themselves, if the media is an aqueous media, the polar hydrophilic regions turn to outside and hydrophobic (water hating) nonpolar parts turn to inside. If the solvent is nonpolar this trend is the nonpolar regions turn to outside and polar parts turn to inside of the structure. Because of the polarity difference, these structures are quite stable. The concentration at which they form micelles is called

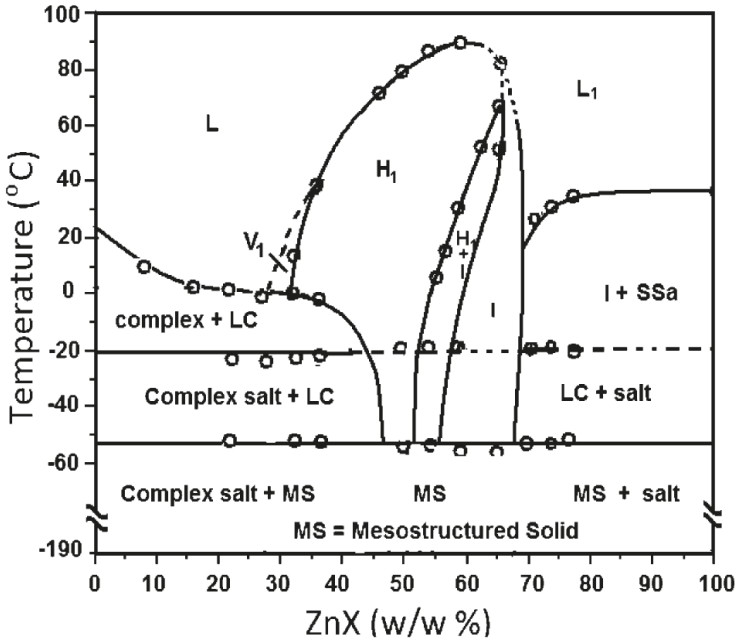

Figure 1.1.3 Phase diagram of $C_{12}EO_{10}$ with zinc nitrate.[1]

[1] Reprinted from Origin of Lyotropic Liquid Crystalline Mesophase Formation and Liquid Crystalline to Mesostructured Solid Transformation in the Metal Nitrate Salt−Surfactant Systems. Cemal Albayrak, Necati Özkan, Ömer Dag, Langmuir, 2011, American Chemical Society, Copyright © 2011, American Chemical Society. Reprinted with permission.

critical micelle concentration (CMC). After this point structures formed by surfactants may change, but number of micelles increase.

Further increase of the surfactant in the media may produce lyotropic liquid crystalline mesophases. The mesophases are quite ordered in mesoscale and diffract x-rays at small angles. Depending on the surfactant/solvent ratio, the mesophase exists in lamella (layered, only layer axis is ordered, and the other two axes are disordered), bicontinuous cubic (3D mesostructure), 2D-hexagonal (two axes are ordered, packing of rod-like micelles, birefringent and can be observed under a polarizing microscope), micellar cubic, and finally disordered fluid phase upon increasing the solvent in the media. Figure 1.1.3 shows a typical phase diagram of a salt-surfactant mesophase [7].

1.1.1. Lyotropic Liquid Crystalline Mesophases of Transition Metal Salt-Surfactants

Many transition metal salts may be used as a solvent to form LLC mesophases with non-ionic surfactants. These salts usually have low melting points and can be easily mixed and homogenised in surfactants to form the LLC phase, see Figure 1.1.3. In the mesophase, the salt species are in their molten phase and act as a solvent. Soft confinement effect reduces melting point of the salts for the assembly process, such that the salt species remain in the hydrophilic domains of the mesophase down to -52^{o}C, see Figure 1.1.3[1]. The solvents can also be acids, such as phosphoric acid, for the assembly of non-ionic surfactants. Phosphoric acid and 10-lauryl ether forms stable LLC mesophase in a broad range of concentrations [2][3]. Mixing acid with salts does not disrupt the phase and could be used as reaction media for the synthesis of metal phosphates. Salts are not limited to transition metal salts. Many lithium salts can also be self-assembled into LLC mesophase. Even though these salts have high melting points, the soft confinement effect also enhances the solubility of salts. Enhanced solubility of lithium salts enables and stabilize the lithium salt-surfactant mesophases [4].

The LLC mesophases, described above, can be used to produce mesoporous metals [8], metal oxides [6], and metal phosphates [2] upon calcination at elevated temperatures. Stability, thermal behaviours, and salt content of these mesophases are important to form stable mesoporous materials. At low salt contents the formed mesostructured may not be stable to elevated temperature treatments and at high salt concentrations, the mesophases are usually disordered or have very low melting points and therefore may not be appropriate for further heat treatments for the formation of mesopores. Therefore, optimum salt content and stability of the salt-surfactant mesophase is critical to be able to use these LLC phase for the synthesis of porous materials.

1.2 Mesoporous Materials

Mesoporous materials have been investigated thoroughly due to their large applicability in various areas. After their introduction by Beck et al. [9], and Attard *et al.*[10], using soft template, significant attention diverted to this area. First synthesis of mesoporous materials was demonstrated using charge surfactants above their CMC by using tetraethyl ortho silicate as silica source for the synthesis of mesoporous silica. The mesostructured silica (surfactants are in the structure) is precipitated from the basic aqueous precursor solutions and then calcined at 450^{o}c to obtain the mesoporous silica [7][11]. In the later process, the LLC media was created by using water and

non-ionic surfactant in the presence of the silica source for the synthesis of mesostructured silica [10]. The process is called liquid crystalline templating [10] The LCT process also allowed to make mesoporous monoliths of silica and some other metal oxides [10][12]. Later, several other methods have been developed to produce many porous materials that may be not possible by micelle or LCT methods and also to make mesoporous thin films. These include hard templating (HT) [13][14][15], evaporation induced self-assembly (EISA) [16][17][18], and molten salt assisted self-assembly (MASA) [19][20][21].

1.3 Hard Templating – Nano Casting Method

In hard templating method, pre-prepared mesoporous silica powders or carbon have been used as a hard template [22]. The method has been developed to produce transition metal oxides that cannot be directly assembled using known methods. The transition metal salts are infiltered into the pre-formed mesopores of silica or carbon and then calcined to produce metal oxides on the pore-walls of these templates that can be removed by either washing in a highly basic or HF solutions. The later process produces mesoporous metal oxides. Using HT method, mesoporous Co_3O_4 [23][24], CeO_2 [25][26], Cr_2O_3 [27][28], Fe_2O_3 [29], MnO_2 [30][31], NiO [29] have been prepared.

Figure 1.3.1 Three steps of hard templating method.

This method has three steps. First the precursor of precursors of the desired material infiltrated into the pores of the hard template particles, then by calcination the desired material, mostly transitions metal oxides, formed within the pores of the hard template. Then the template gets to be removed to form a porous desired material. Templates are usually removed by etching with a selective reactant, for example HF and NaOH are generally used for silica. Hard templates are usually mesoporous silica such as SBA-15 or mesoporous carbon. This process is the reverse of the process for building mesoporous hard template. In their synthesis the template gets removed forms the cavities which are pores in the particles whereas here the surface are comes from the removal of the walls, therefore the structure formed after the calcination is the reverse of the original template. Empty parts are filled and filled parts are empty. Pore structures can be various, depending of the template.

However, it is very difficult to produce thin films and monoliths of metal oxides using this method. There is yet no examples of metal oxide films produced from HT method. Therefore, new methods are needed for the synthesis of porous thin films that are more useful for many technologies.

1.4 Evaporation Induced Self Assembly (EISA) Method

Evaporation induced self-assembly was introduced in 1999 [17]. Process was designed to make porous materials faster and in the form of thin films [16]. Starting with a soluble silica and surfactant in a water/ethanol medium, system forms a denser material as evaporation of ethanol pushes the concentration of the surfactant molecules to the critical micelle concentration limit. The progress of increasing surfactant concentration, initiates the self-assembly of surfactant molecules with silica precursor molecules, then the structure further goes to the LLC mesophase. In this way, it was possible to rapidly make thin films of mesostructured materials, which are highly oriented and as with the case of many surface-active reagents, the concentration inside the composition determines the final structure in the mesophase [15].

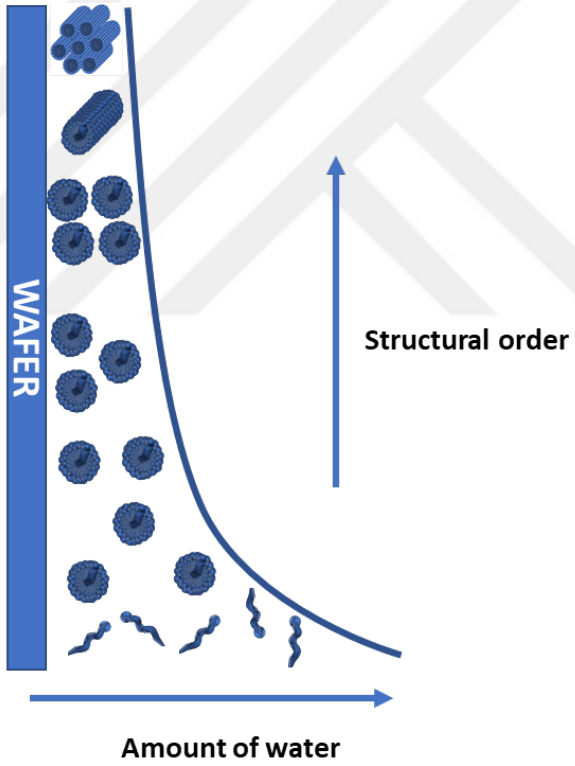

Figure 1.4.1 Schematic representation of EISA process.

This method developed to form mesoporous materials from LLC media faster and convenience. Two ways of coating, which employ this method are dip coating and drop-cast coating. The film thickness in the methods depends on the solution concentration and the rate of evaporation of the solvent. The precursors assemble as evaporation continues and the structure formation is mostly dominated by the weak forces (such as dipole moments, hydrogen bonding, van der Waals interactions). Of course, there are some drawbacks of this method, such as it takes a significant amount of time to form the ordered mesostructure and heat may be required. However,

heating also have an effect that would disrupt and eventually destroy the ordered mesophase. It was shown that the method is applicable to make mesoporous metal oxide films such as FeO_x [32], TiO_2 [33], Al_2O_3 [33], and $CoTiO_3$ [34].

1.5 Molten Salt Assisted Self Assembly (MASA) Method

Molten salt assisted self-assembly was developed by Dag et al in 2011 [20]. They have also shown that $[M(H_20)_n](NO_3)_m$ type transition metal aqua complexes ($[Cd(H_2O)_4](NO_3)_2$, $[Zn(H_2O)_6](NO_3)_2$, $[Ni(H_2O)_6](NO_3)_2$, $[Co(H_2O)_6](NO_3)_2$) can be the secondary component of an LLC mesophase in 2001 [6]. The water molecules surrounding the transition metal can trigger the aggregation of the self-assembly of the surfactant molecules to form hexagonal or micellar cubic structures. Later, these mesophases have been employed to produce mesoporous metal oxides with further development of the salt-surfactant LLC mesophases. In the MASA process, salt stays molten and act as if it is a solvent for the surfactant. The hydrophilic space among micelle in the micellar cubic or the rods in the hexagonal tubular structures are very small (a few manometer). In such small space, the salt species stay molten due to restricted space or confinement effect.

It was first shown by Mieko Takagi [35] who prepared Pb, Si, and Bi films and observed that there is trend between lowering particle size and their melting point. Later in 1986, G. L. Allen *et al.* [36] observed a similar trend by studying on Pb, Sn, In and Bi crystals. They observed almost a linear relationship in a way that confirms the initial observations of Takagi et al. Findings of G. L. Allen also confirmed by Gupta *et al.* in 2008 [37][35]. In their study they have also shown that shape influences the melting point of nanoparticles. These studies show that there is a

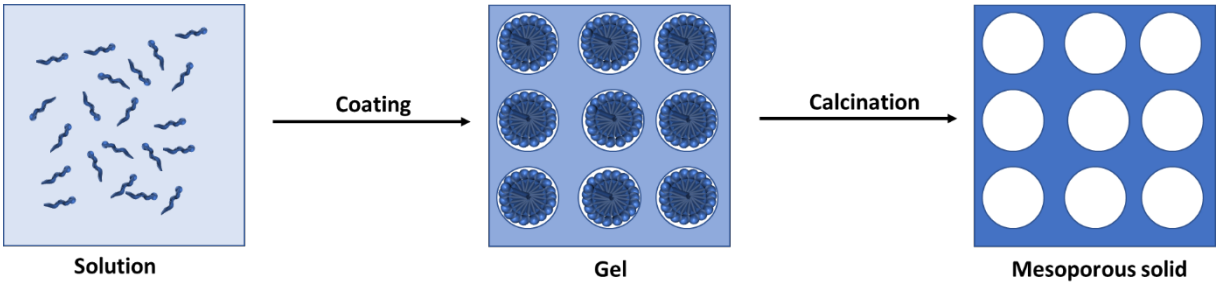

Figure 1.5.1 Schematic representation of MASA process.

critical size for each particle, below that size there is a logarithmic decrease in the melting point, above that size no matter the radius of the grain, particle exhibits bulk behaviour.

In the MASA method, the confined space not only reduces the melting point of the salts, it also hinders the formation of salt crystals. Salt species never crystallize in the salt-surfactant LLC mesophase, because the hydrophilic spaces among the micelle surfactant domains are much smaller than the seed size of a salt to grow. The LLC mesophase in the MASA process eliminate the seeding step as a result eliminates the growth process of the salt crystals and create a proper media for the synthesis of metal oxides of these salts. So far mesoporous thin

films of $MTiO_3$ (M is Co(II), Mn(II), Zn(II), and Cd(II)), $Li_4Ti_5O_{12}$, $LiCoO_2$, and $LiMn_2O_4$ have been developed for various purposes.

1.6 $LiMPO_4$ (M = Mn(II), Fe(II), Co(II), Ni(II)) Development and Examples

After the discovery of $LiFePO_4$ by Padhi and his colleagues, lithium metal phosphates and metal phosphates had drawn significant attention [38]. These materials draw attention because of their possibility to become high voltage cathodes [39]. S. Okada *et al.* shown the capacities of $LiCoPO_4$ and $LiNiPO_4$ are good enough to be comparable with $LiFePO_4$ and in some cases capacities could be higher than that of $LiFePO_4$ [40]. Experiments conducted by Rissouli *et al*. on $LiMnPO_4$, $LiCoPO_4$, $LiNiPO_4$ and their mixtures has shown that these materials are poor conductors in their bulk form, but they have room for improvements [41] with possible increase in the freedom of lithium cation's movements [42]. After the phosphates got introduced by Goodenough *et al.,* Piana *et al.* in 2004 offered a sol-gel synthesis method for phospho-olivine, (olivine structured phosphates) [43]. Method was designed on the idea of smaller particles improve the performance. They have also argued that the carbon placed or left inside the particles improves the electrochemical performance. This was necessary because, while the $LiFePO_4$ has shown excellent properties for a conductor, $LiMnPO_4$ is an insulator. Though it is very stable $LiMnPO_4$ has a wide band gap [44]. This was the reason for the propositions like carbon building [43] or Fe doping [45]. Osorio-Guillen *et al.* proposed that the conductivity problem of $LiMnPO_4$ can be solved with Fe doping. Then in the same year, $LiCoPO_4$ and $LiNiPO_4$, and their mixtures were offered as cathodes [46]. Mixtures were used as a mean of bringing different properties together [47][48], like performance and benevolent behaviour towards the environment. Also, Mn(II) doping into $LiFePO_4$ was tried and interesting enough Mn(II) in low substitutions, have increased the conductivity [49].

The synthesis method, of course, plays a crucial part in the conductivity and property of metal phosphates. In order to improve discharge capacity, and/or conductivity, researches have tried many different synthesis methods. One step low temperature precipitation method was one of the earliest approaches for the synthesis of lithium metal phosphates [50]. This method consists of simply mixing the precursors and let them precipitate. Then there was also hydrothermal synthesis developed for these materials [51]. Autoclaves were used to treat the samples with the intention of forming precipitates in gel phases that would allow some control over particles. Polyol method was also employed on $LiMnPO_4$ [52]. The acetate salts of precursors mixed with $NH_4H_2PO_4$ were used in polyol medium. This method provided very small crystals and cemented the idea of the reverse relationship between crystal size and conductivity.

Many methods form bulk material [53][54][43]. However, as stated before surface area is also very important for the property. So porous olivine structured phosphates were synthesised [55]. In the study conducted by Dominko *et al*. citrate ion was used to form a gel phase, which then created the porous structure. Importance of small particle size was already known and since the delithiation process from other lithium metal phosphates besides Fe(II) [56] was shown [50][57][58][59][60]. Then porous, carbon containing/coated $LiFePO_4$ samples were synthesised by others as well [61][62][63][64].

Carbon coating was proved to be a satisfactory solution for the conductivity issues. Investigations on the electronic conductivity and discharge capacity concluded that the added carbon or built in carbon, depending on the method,

increases both discharge capacity and conductivity [65][66]. However, these methods were in effective in the thin films of $LiMnPO_4$, $LiFePO_4$ and their mixtures and another method have been established to increase the conductivity. The films were crystalline and the capacity of mixed phosphate thin films exceeded their pure counterparts [67]. Mixtures including Ni and Co were also made. These have shown that the properties of the material can be adjusted with cation substitution [68][69][70]. Although these materials have problems with their conductivity [71][72] or limited reversible capacities [54], these challenges are not without solutions and with these materials showing promising properties, further studies could improve them enough to replace the batteries that are used today.

In this thesis, we have developed a method for the synthesis of mesoporous lithium metal phosphates, using a modified version of molten salt assisted self-assembly (MASA) approach. In this synthesis method, non-ionic surfactant 10-lauryl ether ($C_{12}EO_{10}$) with lithium and transition metal salts ($LiNO_3$, $Mn(NO_3)_2$, $FeCl_2$, $Co(NO_3)_2$, $Ni(NO_3)_2$) precursors mixed with water into clear solutions that can be coated over a substrate to produce mesophases. The confinement effect that takes place within the mesophase makes metal salts stay in molten form thus creating a two-solvent system. Evaporating solvent, water, leaves an ordered mesophase with the help of the non-volatile solvent, molten metal salts. The mesophase, upon calcination, forms lithium metal phosphates. This modified synthesis approach has been investigated with x-ray diffraction (XRD), Fourier transform infrared spectroscopy (FT-IR), scanning electron microscopy (SEM), energy dispersive x-ray spectroscopy (EDX), N_2-adsorption-desorption analysis.

CHAPTER 2

2 EXPERIMENTAL

2.1 Materials

All chemicals were purchased from Sigma-Aldrich and used without further purification. Phosphoric acid, used in the solutions, was 85-88 %(w/w) and all the salts were at 99 % purity. In this study, $LiNO_3$ and LiOH were used as the lithium source. $Mn(NO_3)_2.4H_2O$ was used as the manganese source, $FeCl_2$ was used as the iron source, $Co(NO_3)_2.6H_2O$ was used as the cobalt source $Ni(NO_3)_2.6H_2O$ was used as the nickel source. All solutions were prepared using deionized water. Through the study, fresh solutions (prepared each time) were used fresh to prepare the desired materials to avoid the aging effect in the solution phase. Following table lists the amount of each ingredient of each solution.

	$Mn(NO_3)_2.4H_2O$	H_3PO_4	$LiNO_3$	$C_{12}EO_{10}$
1:1	0.251 g	0.115 g	0.068 g	0.626 g
2:1	0.502 g	0.230 g	0.136 g	0.626 g
3:1	0.753 g	0.345 g	0.205 g	0.626 g
4:1	1.004 g	0.460 g	0.272 g	0.626 g
5:1	1.255 g	0.575 g	0.340 g	0.626 g
6:1	1.506 g	0.690 g	0.410 g	0.626 g
7:1	1.757 g	0.805 g	0.476 g	0.626 g
8:1	2.008 g	0.920 g	0.544 g	0.626 g
9:1	2.259 g	1.035 g	0.615 g	0.626 g
10:1	2.510 g	1.150 g	0.680 g	0.626 g
	$FeCl_2$	H_3PO_4	$LiNO_3$	$C_{12}EO_{10}$
3:1	0.596 g	0.345 g	0.205 g	0.626 g
6:1	1.192 g	0.690 g	0.410 g	0.626 g
9:1	1.788 g	1.035 g	0.615 g	0.626 g
	$Co(NO_3)_2.6H_2O$	H_3PO_4	$LiNO_3$	$C_{12}EO_{10}$
3:1	0.873 g	0.345 g	0.205 g	0.626 g
6:1	1.1746 g	0.690 g	0.410 g	0.626 g
9:1	2.619 g	1.035 g	0.615 g	0.626 g
	$Ni(NO_3)_2.6H_2O$	H_3PO_4	$LiNO_3$	$C_{12}EO_{10}$
3:1	0.872 g	0.345 g	0.205 g	0.626 g
6:1	1.744 g	0.690 g	0.410 g	0.626 g
9:1	2.616 g	1.035 g	0.615 g	0.626 g

Table 2.1.1 Amounts of precursors used for the solutions of respective molar ratios in terms of grams.

2.2 Sample preparation

2.2.1 Solution Preparation

Ten samples were prepared using the Mn(II) salt. These samples were prepared in the concentrations ranging from 1:1:1:1 mole ratio of Li(I):Mn(II):H_3PO_4:$C_{12}E_{10}$ ($C_{12}E_{10}$ is 10-lauryl ether, $C_{12}H_{25}(OCH_2CH_2)_{10}OH$) to 10:10:10:1 mole ratios of Li(I):Mn(II):H_3PO_4:$C_{12}E_{10}$ by increasing Li(I), Mn(II) and H_3PO_4 by 1 mole ratio to surfactant in each increments. In all solutions, the mole ratios of Li(I), Mn(II) and H_3PO_4 were kept 1 for the stoichiometry of the final product, $LiMnPO_4$, therefore the ingredients (salts and acid) to surfactant ratio is denoted as n:1 throughout the text to simply the notations. These solutions were examined for their stability as solutions as well as upon coating over a substrate and for the formation of mesophases. After the study on those ten samples, three ratios (3:1, 6:1, 9:1) were selected to run the further experiments for all four metal salts (Mn(II), Fe(II), Co(II), Ni(II)) as low, intermediate and high ingredient concentrations. Solutions for the synthesis of each lithium metal phosphate were prepared using given quantities in Table 2.1. Solutions are prepared by dissolving the amounts of each ingredient, listed above, in 10 g of deionized water and stirring for about 10 minutes until they become clear and homogenous solutions (total 12 solutions). The order of putting each precursor into water is as follows; surfactant ($C_{12}E_{10}$), phosphoric acid, and transition metal and lithium salts.

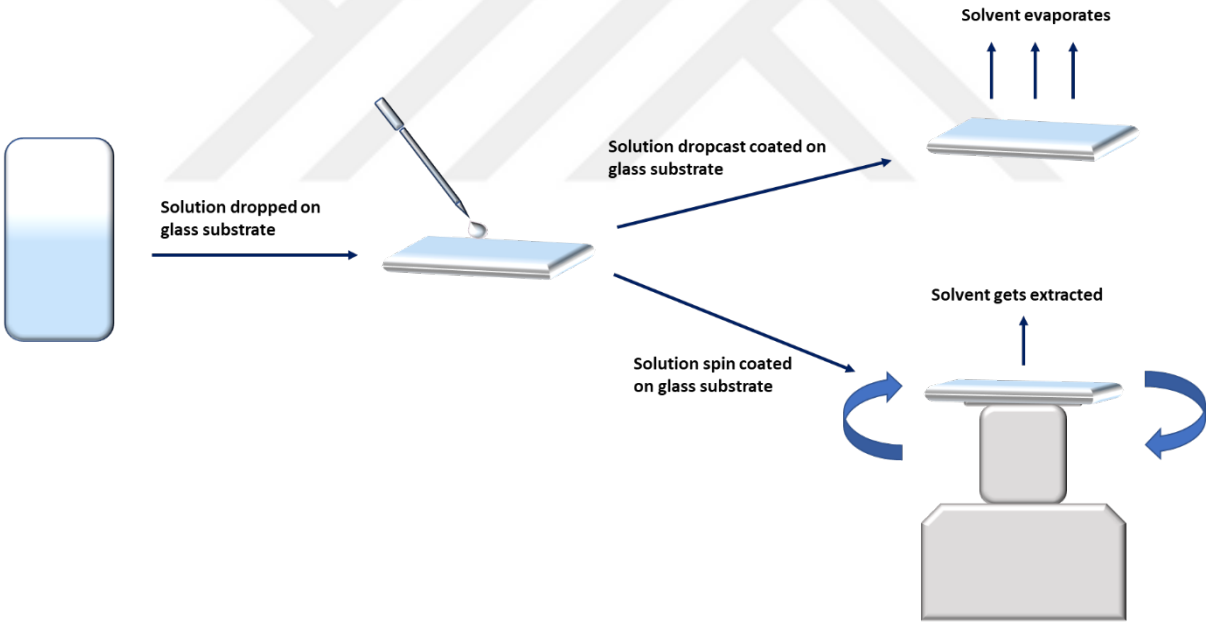

Figure 2.2.1 Schematic representation of spin coating and drop-casting methods.

2.2.2 Preparation of Mesophases Using Spin Coating

Each clear solution above was separately spin coated over glass slides using a WS-400B-6NPP/LITE/AS spin coater of Laurell Technologies Company. Each sample is coated at 1000 RPM on a glass substrate by first locating the substrate and dropping a few drops of the above solution. Fast spinning of the substrate ensures a fast evaporation of water, leaving a gel like film over the substrate.

2.2.3 Preparation of Mesophases Using Drop-Cast Coating

Drop-casting method is applied by slowly dropping each above clear solution on a glass substrate. Then the liquid droplets are spread on the glass to fully cover the glass and finally the excess amount is dripped back into the vial. Substrates with sprawled solution on them dried at room temperature for a time length ranging from about 5 to 20 min, depending on the sample, to allow the formation of an ordered mesophase. Drop-casting provides significantly more samples per batch compared to the spin coating because of the coating' thickness.

2.2.4 Preparation of porous $LiMPO_4$ (M= Mn(II), Fe(II), Co(II), and Ni(II))

Spin coated (coated at 1000 rpm for 10 sec) and drop-casted films are prepared as described above from each solution. Then the freshly prepared films are calcined at various temperatures (250, 350, and 450^{o}C) for a certain duration (2, 4, 8, and 12 hrs). The calcined samples are scraped off from the substrates and collected for XRD, N_2 adsorption-desorption, FT-IR and SEM characterization. Total of 72 samples were prepared from each metal ion system (Mn(II), Fe(II), Co(II), and Ni(II), from total of 288 sets of samples).

2.3 Instrumentation

2.3.1 Temperature Controlled Balance

A balance with a heater, IR35M built by Denver Instruments, was used to determine the mass change of each sample under constant temperature. Samples were prepared using 2 g of solutions of 3:1, 6:1, 9:1 of Mn(II) salt on glass substrate. Then the desired temperature was set, and the mass change was manually recorded every 20 second.

2.3.2 X-Ray Diffraction (XRD)

XRD patterns were recorded on a Rigaku Miniflex diffractometer equipped with a Cu-Kα source operating at 30kV/15mA and a wavelength of 1.5405 Å using the freshly coated samples between 1 and 5^{o}, 2 theta (2θ^{o}) with a scan rate of 1.0^{o}/min at a 0.01 data interval. For the calcined samples, the patterns were recorded using Panalytical X'pert^{3} Powder equipped with a Cu-Kα source operating at 45kV/40mA and a wavelength of 1.5405 Å at wide angles with a scan rate of 2^{o}/min at 0.01 data intervals.

For measurements of low angle diffractions, samples over the glass slides were directly used for the measurements For the wide angle diffraction measurements, the samples were first grinded in a mortar in order to uniformly pack the samples. Then the samples were placed on a single crystal silicon wafer, which was specially cut to make sure none of its crystal planes are looking up in a direction to diffract the x-ray. Then these samples are locked with a stainless-steel frame then measured using Pananalytical X pert diffractometer.

2.3.3 Fourier Transform – Infrared (FT-IR) Spectroscopy

FT-IR spectra were recorded using a Bruker Tensor 27 model FT-IR spectrometer. A Digi Tect TM DLATGS detector was used with a resolution of 4.0 cm^{-1} in the 400 cm^{-1} – 4000 cm^{-1} (mid IR) range with 64 scans. The samples were prepared either as a KBr pellet or spreading on a IR transparent silicon wafer. Samples, prepared as KBr pellet were prepared by mixing 0.150 gr of KBr with an amount of sample that would not change the weight on a three-digit balance. Then the samples are pressed with stainless-steel press with a pressure of 10 tons. Samples on silicon wafers, were prepared by spin coater, under the same conditions as the samples prepared for calcination. These wafers were placed inside a custom-made holder, attached to a heater controller unit and two thermocouples, one attached to the heater controller and the other attached to an independent controller to double check the temperature of the samples during FT-IR measurements.

2.3.4 Scanning Electron Microscopy (SEM)

The SEM images were collected using a FEI Quanta SEM operating at 5kV, 10kV, 15kV and 30 kV. Powder samples were prepared by dispersing in pure ethanol using a sonicater and dropping the dispersion on a silicon wafer attached to a SEM holder. The samples were dried at room temperature before it is inserted into the microscope.

2.3.5 Energy Dispersive Spectroscopy (EDX)

Bruker AXS XFlash EDS detector 4010 attached to the SEM was utilized to determine the elemental composition of the individual particles. EDX was used at 5kV, 10kV, 15kV, 30kV with a spot size of 3 and 5 nm. These conditions are determined by the thickness or the size of individual particles.

2.3.6 N_2 Adsorption-Desorption Measurements

The N_2 adsorption-desorption measurements were carried out by using a Tristar 3000 automated gas sorption analyser of Micrometrics in a relative pressure range of P/P_o from 0.01 to 0.99 atm. The saturated pressure was measured over 9 hours. Samples for this technique were prepared in several steps. Initially, sample holders were washed using aqua-Regia and base bath diluted with water, then rinsed with de-ionized water and ethanol. These tubes were dried and then placed inside a degas chamber at 200^oC for 2 hours, vacuum reaches to 35 mTorr. Then the weights of tubes measured to have the empty mass. Then the samples, prepared and weighed around 0.2 g, were place inside the tubes. The tube with the sample was degassed again to remove the adsorbed water and other volatile species to get the sample's true mass. The degas time was variable, depending on the sample. The sample was evacuated until the vacuum reaches to 35 mTorr vacuum; it was kept at least 2 hours to make sure all volatile species were removed and reweighted to determine the mass of the sample. Tubes then placed inside the instrument with insulating jackets. These jackets make sure the temperature is even through the tube. Then the sample tube was kept in the liquid nitrogen container during the measurement.

CHAPTER 3

3 RESULTS AND DISCUSSION

3.1 Solution Phase

Clear aqueous solutions of salts ($LiNO_3$ and $[M(H_2O)_6](NO_3)_2$, where M is Mn(II), Fe(II), Co(II), or Ni(II)), surfactant ($C_{12}E_{10}$), and phosphoric acid (H_3PO_4) were prepared in stoichiometric ratios of salts and acid and various concentration of surfactant. These solutions, prepared for the synthesis of lithium metal phosphates, are examined for their stability; it was tested for the duration of these solutions as a clear solution. The solution that precipitate overtime is considered to be unstable. The stability of the solutions is extremely important for the synthesis of mesoporous lithium metal phosphates. Because, unstable solutions produce a precipitate of large non-porous solid particles. To prevent the formation of bulk particles of any size, the reaction conditions that may create instability to the solutions have been investigated to elucidate their origin. It was determined that there are three reagents that may be responsible for declining stability of the solution. These are time, salt concentrations, and pH. Solutions of Mn(II) and Fe(II) have tendency to form precipitates in time regardless of the concentration. The precipitation enhances with increasing salt concentrations and pH of the solutions.

Nitrate ions of the salts, dissolved in the solution, get reduced and form nitric oxides then evaporate from the solution. As they evaporate they oxidize the metal ions and this way metal ions start to react and form precipitates. Increased concentrations of salt also increase the concentration of nitrate ions present which will in turn oxidize the transition metal ions to enhance precipitation. The hydronium ion (H_3O^+) in the solution stabilize the nitrate ions. Increasing the pH of the media enforces the second and third dissociation of phosphoric acid, increases the phosphate ion concentration in the media, and enhances the reaction with metal ions to form $LiMPO_4$ particles.

3.2 Solution Behaviour in Time

Solutions, those prepared using Mn(II) salt, precipitate over time and the time length for the precipitation to occur is inversely proportional to the concentration of manganese nitrate salt. Concentrated solutions are less stable because of the higher concentration of nitrate ion, which reacts to oxidize transition metal ion, present in the solution. In solutions prepared using iron chloride salt, nitrate ion in the media coordinates to iron (II) ion present and form a dark coloured solution. The dark colour disappears if the solution kept open, which indicates that the nitric oxides, produced from the nitrate ions, evaporates, where the dark colour disappears (solution become clear and colourless). However, both Co(II) and Ni(II) solutions at all concentrations are stable indefinitely.

3.3 Solution Behaviour by Increasing pH

The pH of the solution determines the amount of phosphate ion in the media. Lower pH values prevent H_3PO_4 to partially disassociate and create phosphate ion that reacts with the metal ions to form precipitate. Solution of 3:1 ratio precipitated quickly, however, solution of 9:1 ratio did not. Lower concentration solution precipitated because of the lower hydronium ion concentration, relatively higher pH; the transitional metal phosphates and lithium metal

phosphates are not soluble in water; however, they disassociate in acidic medium. Low hydronium ion concentration creates an effect that will be mentioned in the section, where lithium dihydrogen phosphate is added into water as the Li^+ and PO_4^{3-} ions source. Solution with higher acid concentration does not form precipitate because of the higher hydronium ion concentration in the media.

3.4 Lyotropic Liquid Crystalline (LLC) Mesophases

Drop casting or spin coating of above clear solutions form lyotropic liquid crystalline (LLC) mesophases. Upon coating, time dependent stability of the LLC mesophases were monitored by using x-ray diffraction (XRD) and polarized optical microscopy (POM) techniques. In the initial part of these experiments, efforts were focused on determining a range of salt and acid ratios with respect to the surfactant concentration. To do so, solutions with range from 1:1 to 10:1 ratio, (Li(I)-M(II)-H_3PO_4):$C_{12}E_{10}$, have been prepared, where the Li(I):M(II):H_3PO_4 ratio is always 1:1:1. Upon homogeneously mixing the solutions, they are spin coated on glass slides to form the LLC mesophase and then monitored by recording their XRD patterns over time, see Figures 3.4.1-3. Results have shown effects over time and concentration on the stability of mesophase and the unit cell parameter of the LLC phase.

In low concentration ratios, the mesophases are unstable. They form an ordered mesostructure, however, over time they fail to keep their mesophase that becomes disordered. This could be due to the amount of water, salts, and acid vs the amount of surfactant in the samples. As the water evaporates, initially, surfactant loses its hydration water but with the assistance of salt species, remaining water, and acid, the LLC mesophase form, but, as remaining water continues to evaporate, there are not enough reagents to hold the mesophase together and the diffraction line, at small angles, disappears. It was observed that in a 3:1 ratio, the film is stable enough and holds the meso-order over time, see Figure 3.4.1. Continued observations of other systems with increasing the inorganic ingredients (salts and acid) in the samples revealed some aspects. As the ingredient concentration goes up it takes some time to form an ordered mesostructure, compare patterns in Figure 3.4.1. Excess water evaporates later at higher ingredients ratios then the lower ratios. Therefore, the water evaporation behaviour makes the difference in period of formation of the mesophase. Regardless of the ingredient/surfactant mole ratio, the diffraction line intensity decreases in time, as shown in Figure 3.4.1. After the formation of the ordered mesophase, it is likely that the loss of water continuous that reduces the unit cell d-spaces in the mesophase. This could be due to formation of $LiMPO_4$ and reduction on the ingredient/surfactant ratio in the mesophase. Note also that the small angle diffraction line shifts from 1.85 to 1.70^o, 2θ, corresponding d-spacing have changed from 4.76 to 5.19 nm as the ingredient ratios increases. This is due to the amount of ingredients and water in the mesophase. With the increase of salt and acid, the amount of water kept also increases, which then occupies more space than it would have compared to low ingredient ratio. Since small angle XRD patterns consist of a single line, it is very difficult to determine the structure and unit cell parameters of the mesophase in all compositions.

Mesophases made by using solutions of low concentrations have demonstrated low stability through time, see Figure 3.4.1 A and B. Samples initially formed very ordered mesophases, which diffract instantly upon coating, however, these phases started to lose order within 5 minutes and lost their order completely in 20 to 30 minutes. In 2:1 ratio, it was observed that while the mesophase is losing order, it was also shrinking. This is a possible result because of the water lost from the mesophase, leaves the space it occupies between the structures formed by the surfactant, hence lowering the unit cell dimension, and as water evaporates, the system starts to collapse because

of the lack of water. This trend changes as concentration of solutions increase, see Figures 3.4.1 C and D and 3.4.2. With an increase in the ingredient concentrations, system starts to require a bit of time to form the mesophase, which appears to be robust through time. In 3:1 ratio, see Figure 3.4.1 C, the mesophase appears in 5 minutes and remains for an extended period. The order decreases with time and also the diffraction angle shifts to higher angles, which states that the unit cell of the mesophase shrinks with the loss of water. Yet, the phase stands as is, with the assistance of water molecules coordinated around the metal ions.

The trend of 3:1 ratio, in terms of the stability and mesophase, shows that the unit cell shrinkage is similar. In concentrations from 3:1 to 5:1 ratios, see Figure 3.4.1 C and D and 3.4.2 A, there is a steep fall of order in mesophase, which gradually shifts to smaller unit cells as it loses water. The mesophases, formed by the highest concentrations, have shown that the structural order is mostly intact. The samples made from solutions of 6:1 to 10:1 have shown similar trends. At higher concentrations the time required to form the mesophase is also increased.

Wide angle XRD patterns were also recorded to monitor if there is any salt crystallization during aging the mesophases, see the patterns in the right columns in Figures 3.4.1 to 3.4.3. The XRD patterns at high angles consist of a broad future due to glass substrate under the samples, indicating no salt crystallization from the mesophases. However, the sample with a 10:1 mole ratio was deemed unstable because the change in the colour of the coating turns from opaque white, which consists with the colour of the gel, to pinkish brown. This suggests that there is a formation of product at room temperature, inside the gel phase, but no diffraction was observed due to amorphous nature of the product. So, at the end of these investigations, we have decided to limit further investigations to 3:1, 6:1, and 9:1 ratio for the synthesise of mesoporous lithium metal phosphates, to represent low, medium, and high concentrations, respectively.

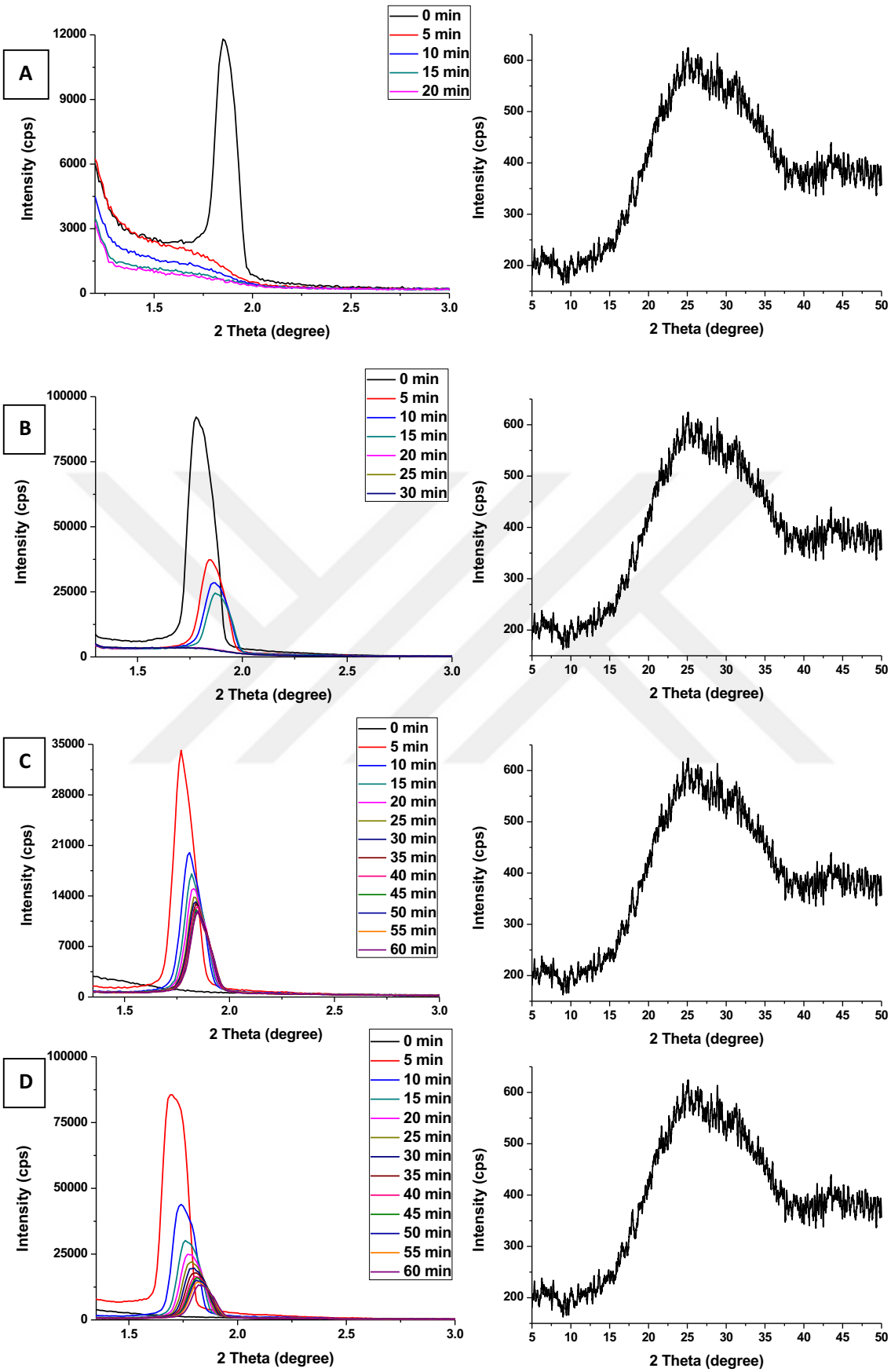

Figure 3.4.1 Time dependent small (left column) and wide angle (right column) XRD patterns of LLC mesophases of Mn(II) system with an ingredient: surfactant mole ratio of (A) 1:1, (B) 2:1, (C) 3:1, and (D) 4:1.

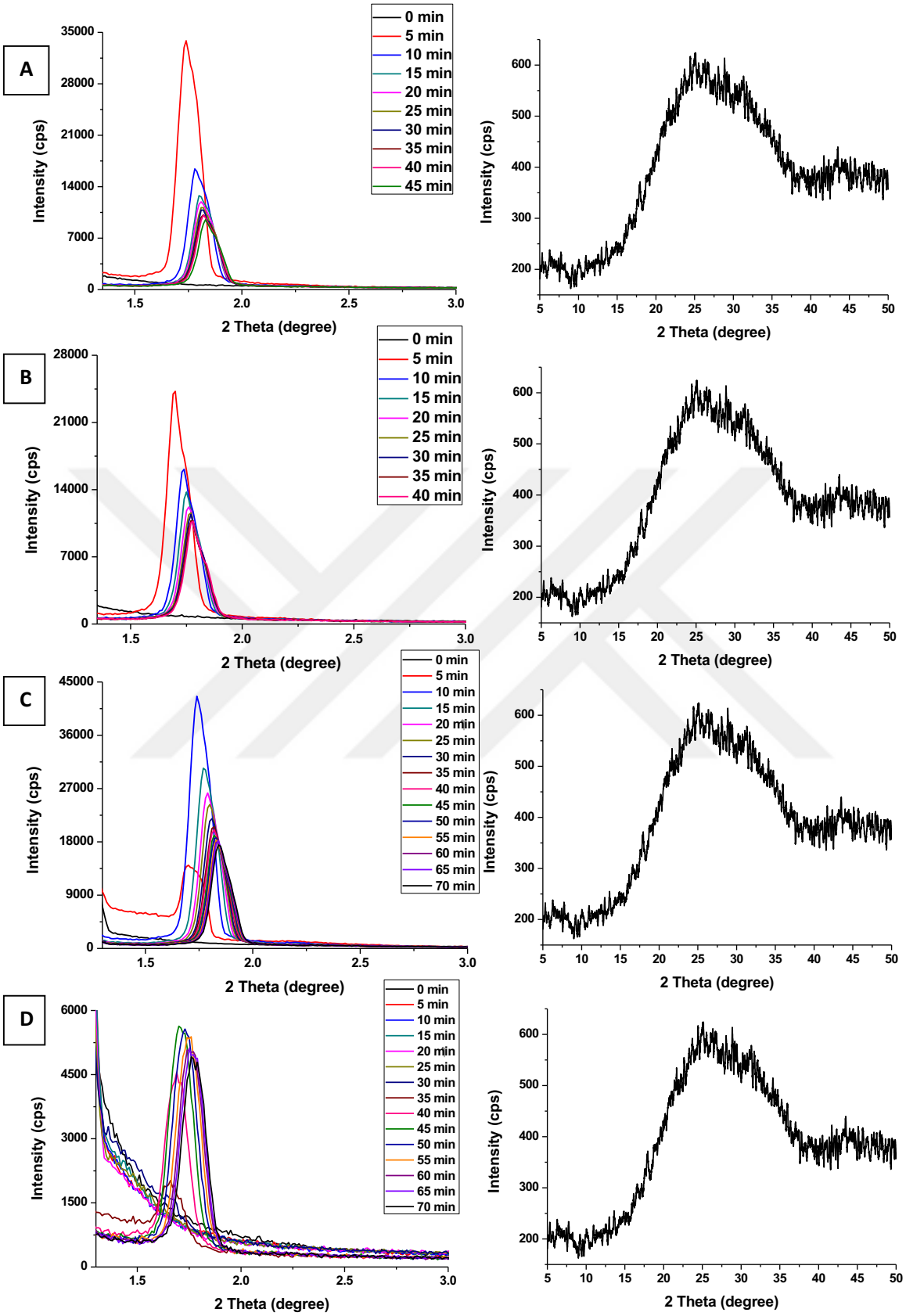

Figure 3.4.2 Time dependent small (left column) and wide angle (right column) XRD patterns of LLC mesophases of Mn(II) with an ingredient: surfactant mole ratio of (A) 5:1, (B) 6:1, (C) 7:1, and (D) 8:1.

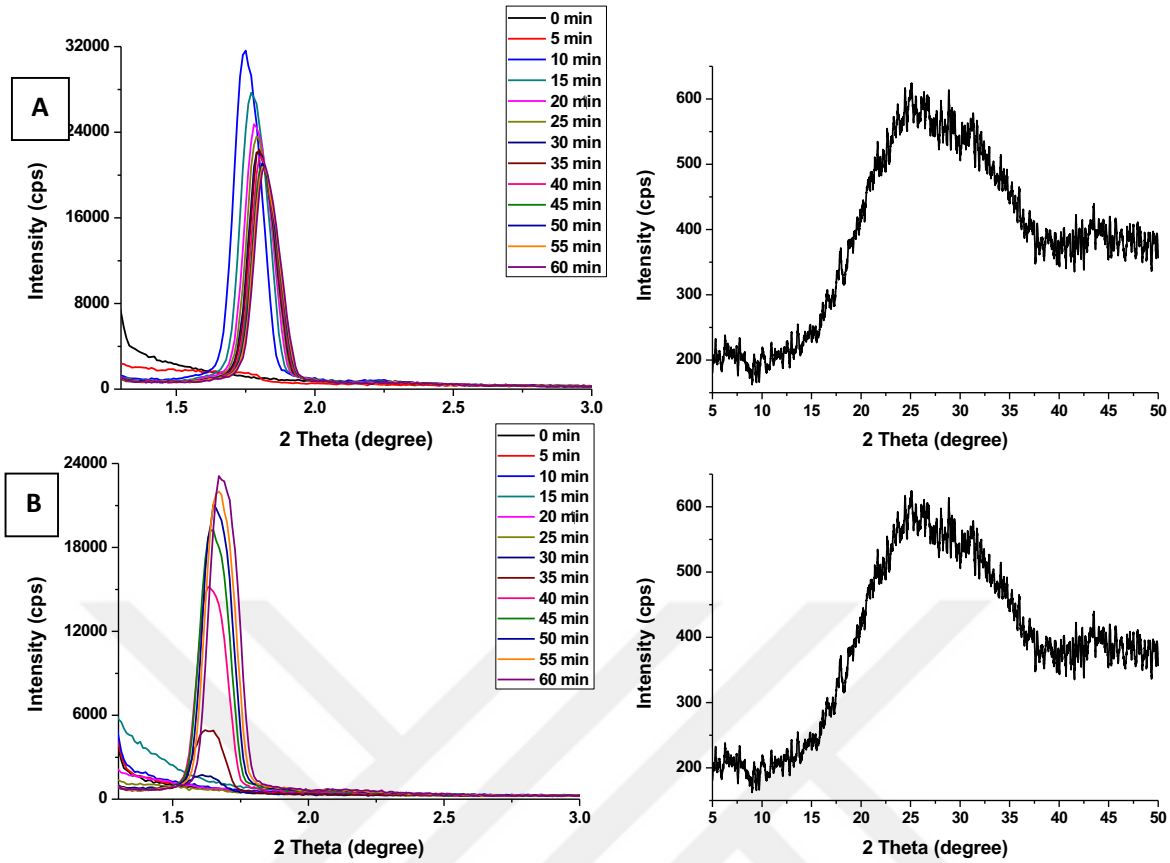

Figure 3.4.3 Time dependent XRD measurements of LLC mesophases of Mn(II) with an ingredient: surfactant mole ratio of (A) 9:1 and (B) 10:1.

The LLC mesophases were obtained by spin coating and drop-casting methods using clear stable solutions. The clear solutions lose the volatile solvent quickly upon coating over substrates, to form gel like LLC mesophases. Spin coating and drop-casting methods were employed to observe possible differences that may occur between the coatings. In spin coating, the lithium metal phosphate formation, upon calcination, speeds up with lowered water amount. Before the calcination, the mesophase forms faster in spin coating; the reason is the removal of solvent is much faster in spin coating. Also, during the coating, the fast spinning of the glass substrate provides enough force for the orientation of the mesostructure. Thickness of the coating is also more restrained in spin coating. Two main variables determine the thickness, first is the concentration of the solution and second is spin rate, the amount of round per minute (rpm). Increasing the amount of solvent in the clear solutions and/or increasing coating rate produce thinner coatings. Drop casting method produces thicker gels, where the reactions are slow due to higher amount of water left in the gels. Evaporation of the solvent takes much longer time to be removed, therefore the mesophase formation takes more time to form. The gel samples from 3:3:3:1, 6:6:6:1, and 9:9:9:1 (corresponding to Li(I):M(II):H_3PO_4:$C_{12}E_{10}$) mole ratios of solutions were used for the synthesis of lithium metal phosphates through the mesophases. To make the labelling short, these samples are called 3:1, 6:1, and 9:1, respectively. The coating of the solutions produces a gel like films that diffract at small angles. However, the mesophase formation, upon coating, is not instant. Maybe, a small amount of water present in the coatings prevents the formation of the mesophase as the micelles of the surfactant molecules are still too far apart from each other to form an ordered gel-phase.

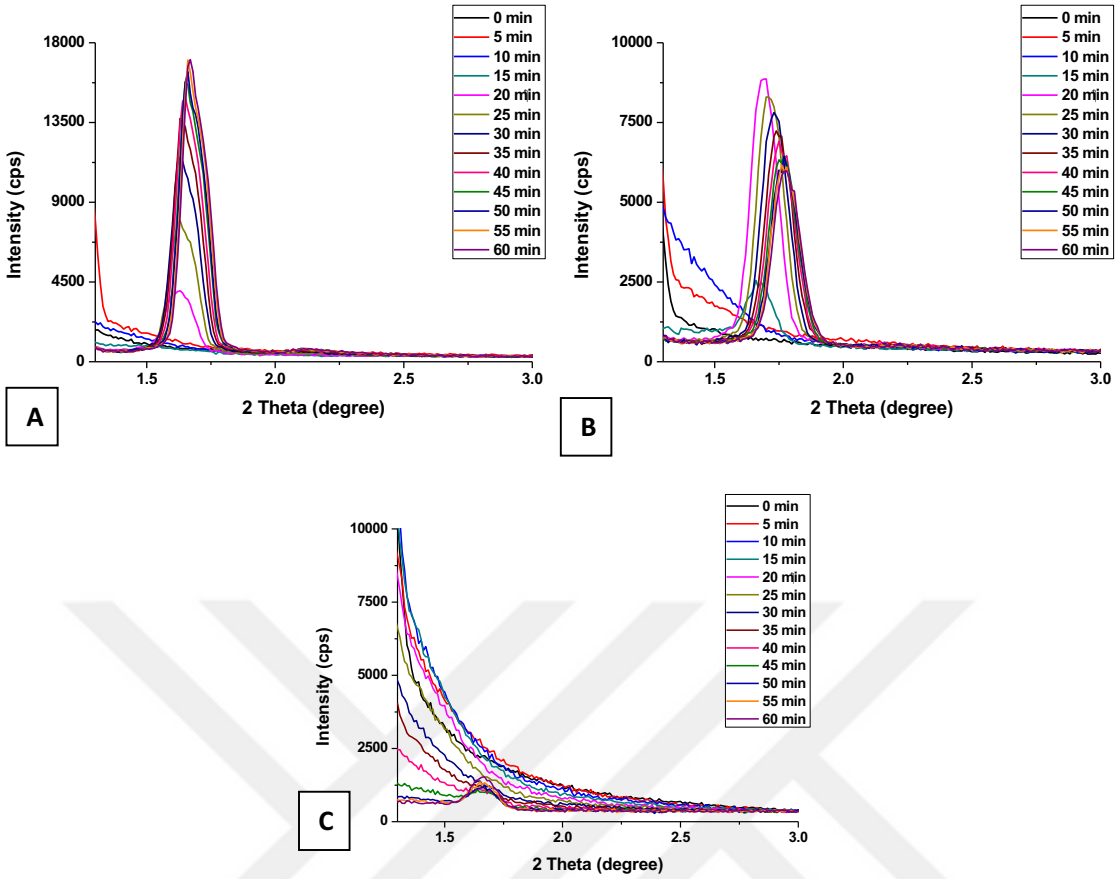

Figure 3.4.4 Time dependent XRD patterns of LLC mesophases of drop cast coated Mn(II) solutions with an ingredient: surfactant mole ratio of (A) 3:1, (B) 6:1, and (C) 9:1.

As the water molecules further evaporate from the coatings, the micelles closely pack into an ordered LLC mesophase. The mesophase reaches an equilibrium with the water in and out-side of the gel and therefore stabilizes over time. For 3:1 ratio, small angle diffraction line of the LLC mesophase, changes from 5.20 to 4.84 nm, for 6:1 ratio, 5.31 to 4.98 nm. For 9:1 ratio, the signal stayed at 5.31 nm. In the 9:1 ratio, the mesophase diffraction lines are quite low in intensity.

The changes in the LLC mesophase of the 6:1 ratio in the Mn(II) system was also followed by FT-IR spectroscopy, see Figure 3.4.5. It was observed that the broad bulk water peak at around 3400 cm^{-1} diminishes in time. This was expected since bulk water is excess in the initial media and it would evaporate over time. Also, the peak at around 2400 cm^{-1}, due to protonated water, diminishes [73]. The signals belonging to the surfactant molecules at around 2900 cm^{-1} display some minor changes, due to formation of mesophase. The amount of water first lost from the surroundings of the surfactant. After the initial loss of water, the LLC phase is pretty much in balance between the atmospheric water and the water in the mesophase, at which the change in the water peak stops. During the water evaporation step, there is a noticeable change in the nitrate region of the spectrum [74], 1200-1500 cm^{-1}, see Figure 3.4.5. Intensity of the nitrate peaks drop over time and likely due to transformation and decomposition of some of the nitrate ions as nitric acid and nitric oxides during the drying step.

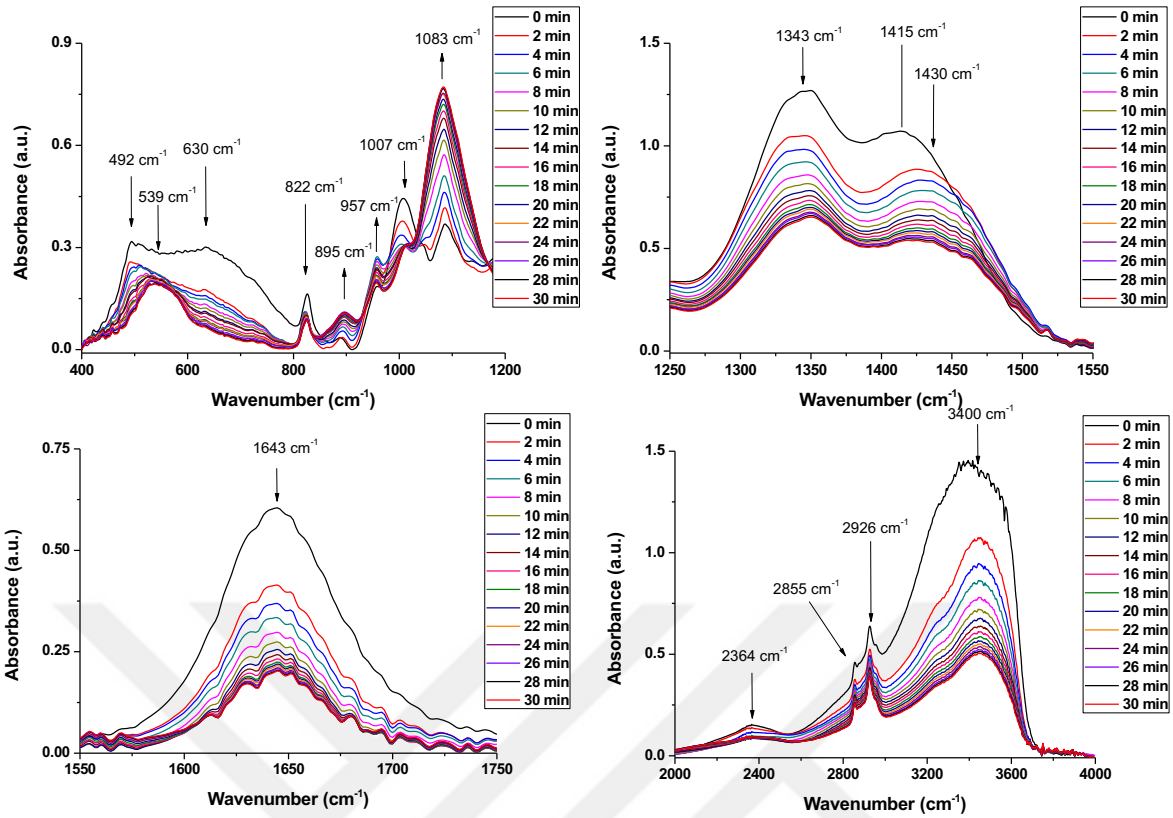

Figure 3.4.5 Time dependent FT-IR study of the LLC mesophase of solution prepared from 6:1 mole ratio for Mn(II) salt. Arrow indicate the change in time. The phosphate region of the spectrum (upper left), nitrate region of the spectrum (upper right), water region (lower left & right) and surfactant absorbances lower right.

Phosphate ions of the acid related peaks change their intensity as the mesophase lose water, which also indicates an interaction between the phosphate ions and metal ions/surfactant molecules. The phosphate ion asymmetric stretching mode, at 1083 cm^{-1}, increases in intensity while another asymmetric stretching mode at 1007 cm^{-1} disappears [75]. Symmetric stretching at 957 cm^{-1} gets more pronounced in time. Symmetric bending signal at 492 cm^{-1} and asymmetric bending signal at 630 cm^{-1}, which belong to phosphate, are slowly degrading over time and a peak close to symmetric bending mode emerges at 539 cm^{-1}. Two peaks at 1343 cm^{-1} and 1415 cm^{-1}, are due to nitrate ion interacting with metal species in the media and the latter peak shifts to 1430 cm^{-1} over time, showing an increase of the nitrate metal ion interaction [76]. The 1643 cm^{-1} peak corresponds to the bending mode of free water, 2364 cm^{-1} corresponds to the presence of hydronium ion and the broad peak centred around 3400 cm^{-1} includes symmetric and asymmetric stretching of water [77][73]. Disappearance of the peak at 1007 cm^{-1} and the intensity increase of the peak at 1083 cm^{-1} show the formation of metal phosphates [78][75].

3.5 LLC Mesophase Behaviour with Temperature

The order on the mesophase disappears by heating the samples at higher temperatures. As the temperature increases, water further evaporates, and the system starts to lose its hydration water, which surrounds the transition metal salt ions, phosphate species and solvates these species in the LLC mesophase. Amount of water is important for the stability of the mesophase and without water the phase collapse, see Figure 3.5.1. Here the coatings are treated at their respective temperatures for an hour.

When looked at in detail, the differences in behaviour with increasing concentration, the relation of mesophase order with temperature is more explicit. In the case of 3:1 ratio, it is observed that this case contradicts with the cases of 6:1 and 9:1 ratios. The reason for this difference are explained by the presence high water concentration that is correlated by our findings. The 3:1 ratio case has way too much water in the beginning. Water hydrates the surfactant molecules and reduces the meso-order, however by heating the coatings, water evaporates and first reduces the hydration water as a result the order of the mesophase increases; heat at moderate levels helps the surfactant to form micelle structures. The resulting structure is more ordered. Increasing the temperature further causes more water lost and loss of meso-order. The loss of order increases by increasing the temperature and concentrations of the ingredients in the mesophase. This is due to required amount of water vs the water present in the system under the influence of temperature. At high concentrations, water present in the system is enough for maintaining the mesophase, however further heating disrupts the meso-order by further evaporation of the water in the media (see Figure 3.5. 1.).

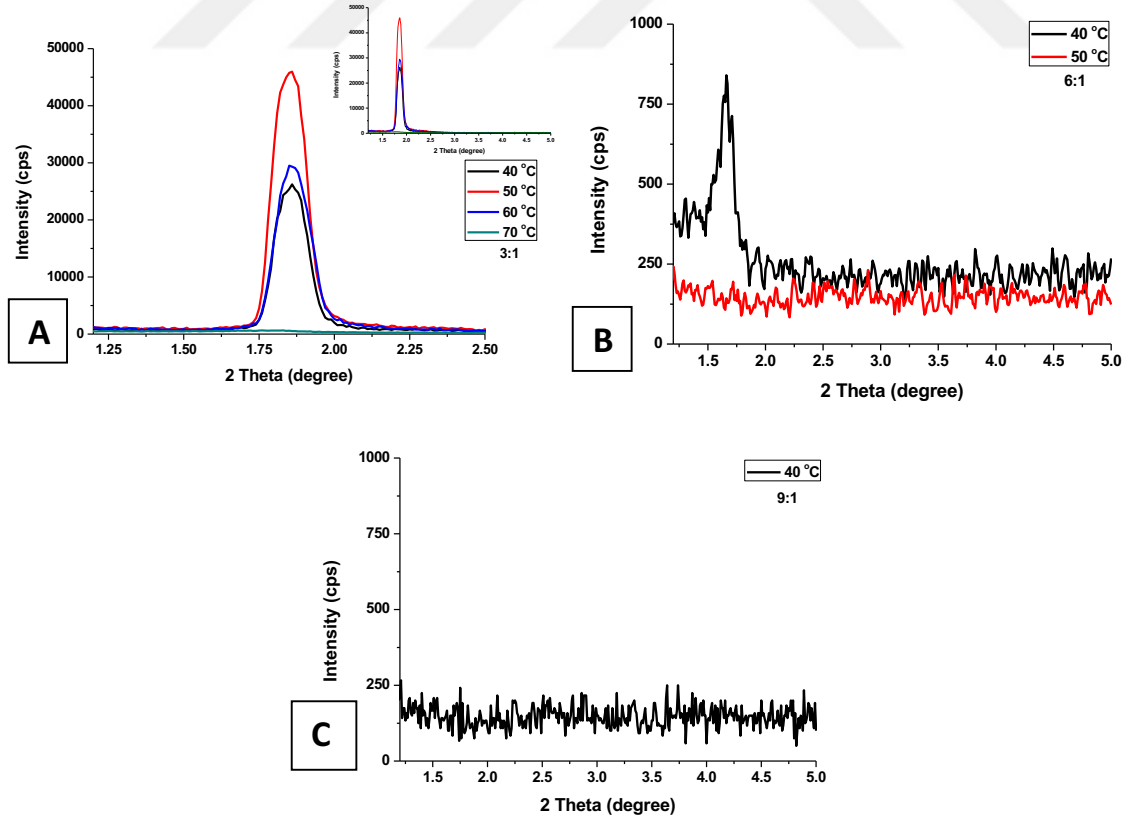

Figure 3.5.1 XRD patterns: Respond of LLC mesophase to heating at indicated temperatures of the Mn(II) samples with an ingredient: surfactant mole ratio of (A) 3:1, (B) 6:1, and (C) 9:1.

The effect of varying temperature on the mesophase was also followed by FT-IR spectroscopy, see Figure 3.5.2. During heating, we observed many changes in the FTIR spectra. Symmetric bending modes of phosphate are observed at 470 and 498 cm^{-1}. The asymmetric bending modes are observed at 602, 614, and 635 cm^{-1}, see Figure 3.5.2 (A). Bending peaks of lithium manganese phosphate at 250°C, convoluted to show multiple peaks, see Figure 3.5.2 (C). The asymmetric bending modes dominate the spectra. The bending mode has its most intense peak at 602 cm^{-1} with shoulders at 572 and 615 cm^{-1}. The symmetric bending peaks consisted of two peaks at 470 and 498 cm^{-1}. Initially at low temperatures the bending signals of phosphate are broad due to presence of various form of phosphate in the media. This broad peak also corresponds to the phosphate bending, observed during time dependent experiment at room temperature. With increasing temperature of the media, these peaks split into two peaks, one peak has very low intensity compared to the other. The first peak is due to the symmetric bending and the other is due to the asymmetric bending modes [75][78][79][76][18]. In the asymmetric bending region, there is a notable change by increasing temperature. As the broad initial peak disappears, a broad shoulder at around 525 cm^{-1} starts to shift and disappears; the signal shifts to around 600–650 cm^{-1} starts gaining intensity with a shoulder towards the higher energy, at 614 cm^{-1}. There is also another peak emerging by increasing temperature at 635 cm^{-1}.

These changes start to occur at 70°C. At that temperature, the asymmetric and symmetric bending peaks start to emerge, and initial hydrated phosphate peaks significantly diminished. The symmetric stretching signals of phosphates are observed at 900, 957, and 1002 cm^{-1} and the asymmetric stretching modes are observed at 1029, 1084, and 1127 cm^{-1}, see Figure 3.5.2 (B). The symmetric stretching signals at 900 and 1002 cm^{-1} disappears with increasing temperature, indicating the formation of lithium metal phosphate. The stretching peaks of phosphate was also convoluted to evaluate its components, see Figure 3.5.2 (D). This fitting was successful, and the sum of generated peaks fitted perfectly to the original data. From the fitting data it was understood that the signal with the highest intensity was composed of two large signals at 1046 and 1115 cm^{-1} and a weak signal at 1084 cm^{-1}. At RT, the 1127 cm^{-1} peak did not exist. By increasing the temperature of the media, a shoulder emerges in the asymmetric stretching region of phosphate. Shoulder at 1002 cm^{-1} loses its intensity but the fitting shows that it still there inside the larger stretching peak. The symmetric stretching mode at 957 cm^{-1} loses its intensity.

PO_4^{3-}	Frequency (cm^{-1})
v_1	968
v_2	530
v_3	1000-1150
v_4	650

Table 3.5.1 IR signal frequencies of phosphate ion**.**

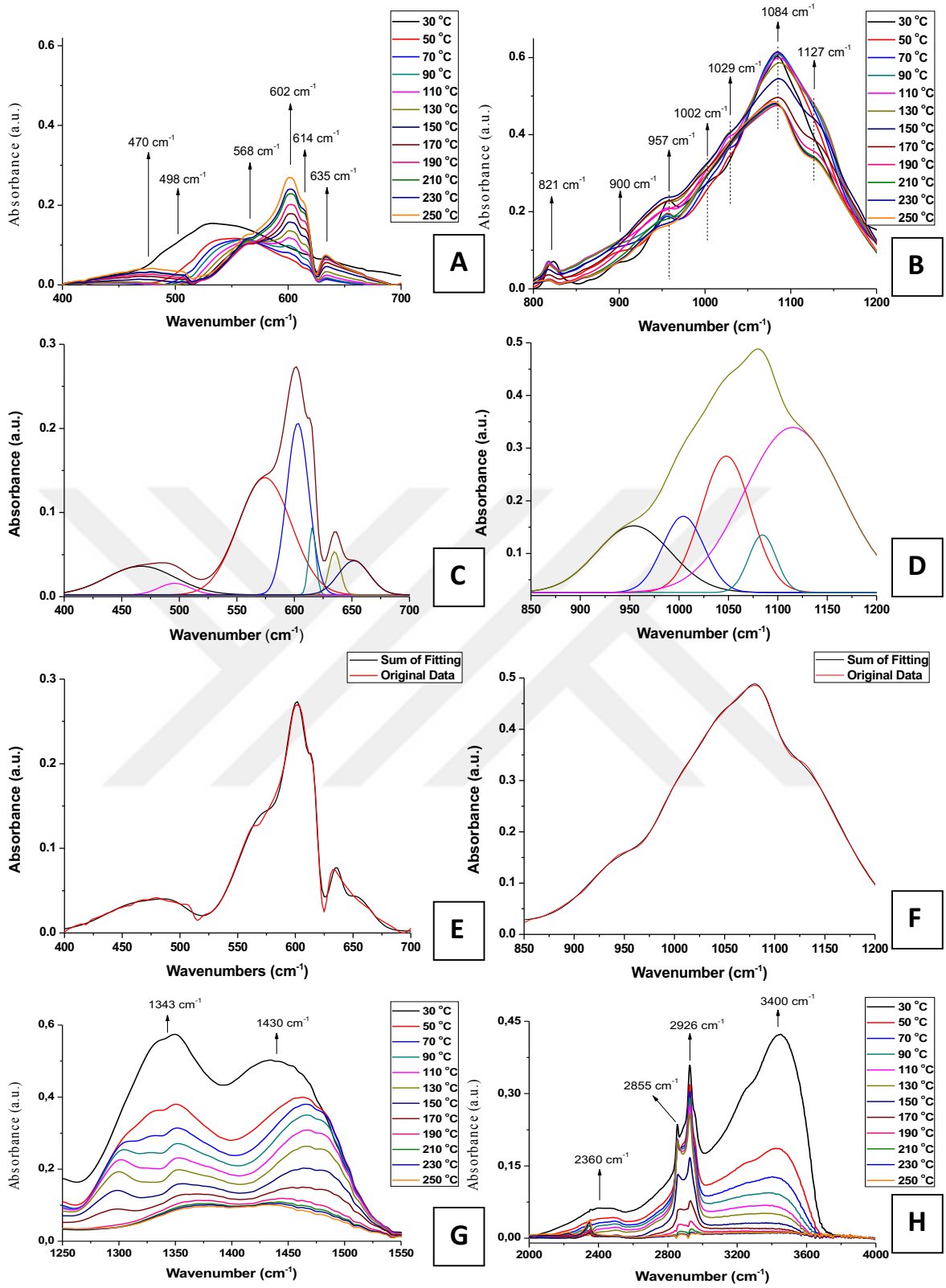

Figure 3.5.2 Temperature dependent FT-IR study of the LLC mesophase, prepared from 6:1 mole ratio of Mn(II) salt. (A) absorbances of bending modes of phosphate. (B) absorbances of stretching modes of phosphate. (C) Fittings of the bending modes of phosphate. (D) Fittings of the bending modes of phosphate. (E) comparison of the sum of the fitting results with the actual data for the bending modes of phosphate. (F) comparison of the sum of the fitting results with the actual data for the stretching modes of phosphate. (G) Absorbance signals of nitrates. (H) absorbance signals of water stretchings and hydronium ions with absorbances from surface agent.

Nitrate species and water molecules inside the system are also examined using the FT-IR data. The detected mode of nitrate at 1343 cm^{-1} and 1430 cm^{-1} belongs to its asymmetric stretching modes [74], see Figure 3.5.2 (G). Both peaks disappear by heating the samples. The high energy peak appears upon coordination of nitrate ion to a metal centre with the evaporation of water from the media. Furthermore, the nitrate species decomposes into nitrous oxide and leave from the media. This is clearly observed in the spectra of the nitrate region by heating; the intensity in the nitrate region gradually decreases by increasing the temperature of the media

Two peaks, one at 2360 cm^{-1} and the other around 3400 cm^{-1} are signals from water, see Figure 3.5.2 (H) [77] [73]. First peak originates from hydronium ion and the later broad peak is due to stretching modes of water. Signals at 2855 and 2926 cm^{-1} belong to surfactant molecules, which are simply burn out by heating near 250°C.

3.6 Measurements of Mass Change at Selected Temperatures

The change in mass over time and temperature, provides information regarding our reactions. The experiment was carried on a balance with a heater. Examination of the mass change over time for each temperature, a step is observed at 50°C shifts on the time axes with increasing temperature, see Figure 3.6.1. This initial step at 50°C shows the loss of water and nitrate species. While the loss of initial volatile species continues, another step is observed at 100°C. Before that point, the step regarding water and nitrate merges into the main curve as temperature increased, this is possible because at these temperatures water and nitrate evaporates so fast, they do not take enough time to create a step in the data. However, at 100°C there is another step observed, which is not the step that belongs to free water and nitrate species. This step is the removal of coordinated water molecules in the media. After this point, there is another significant step at 160°C. At this point, parts of surfactant molecules start to burn out.

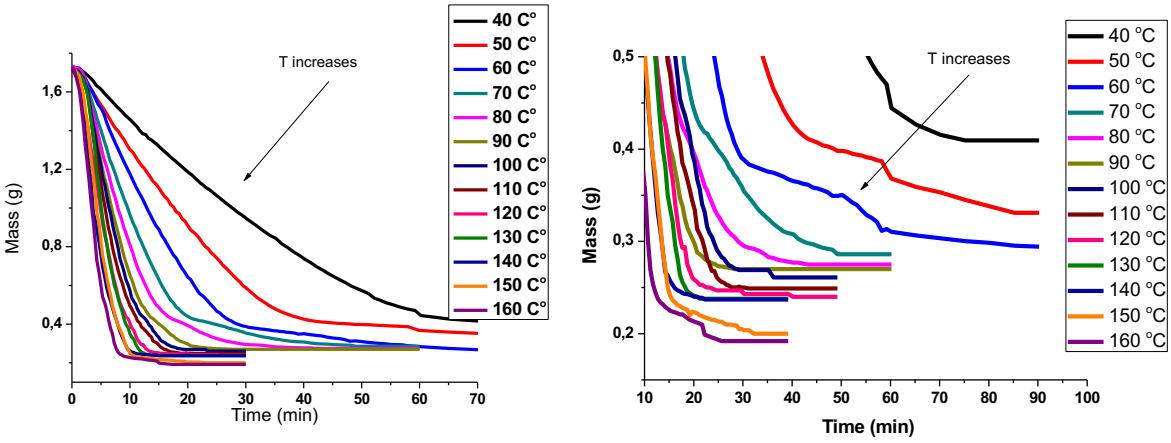

Figure 3.6.1 Mass change over time under constant temperatures. Normalized values (left). Enhanced data for observing the steps of nitrate and surfactant loss.

Above proposals were supported by the FT-IR spectroscopy. The same samples were investigated using FT-IR spectroscopy to understand how the samples respond to temperature. The spectra were collected at the end of each temperature and pressed using KBr into a pellet to run the FTIR spectrum. Results, obtained from these measurements are normalized using the phosphate stretching signals to evaluate the changes, in the intensities of nitrate, carbon species, and water molecules, relative to the phosphate signals. These measurements have shown that the initial FTIR study on the thermal behaviour of the mesophase are consist with the previous temperature

dependent FT-IR study, compare Figure 3.5.2 and 3.6.2. With increasing temperature, both nitrate ion and bulk water removal from the samples are enhanced. The only difference, using KBr, is that the nitrate species formed a sharp single peak instead of broad double peaks at around 1380 cm^{-1}. When the samples are mixed and pressed with KBr, there is an exchange of Br^- and NO_3^- ions and a formation of KNO_3 crystals in the samples. The sharp peaks at 1380 cm^{-1} originates from KNO_3 crystals, see Figure 3.6.2. This is commonly observed if the nitrate containing samples are mixed and pressed with KBr. Signals that are between 2800 cm^{-1} and 3000 cm^{-1} are originated from surfactant molecules and the changes in these are also consistent with the previous temperature dependent FT-IR measurements.

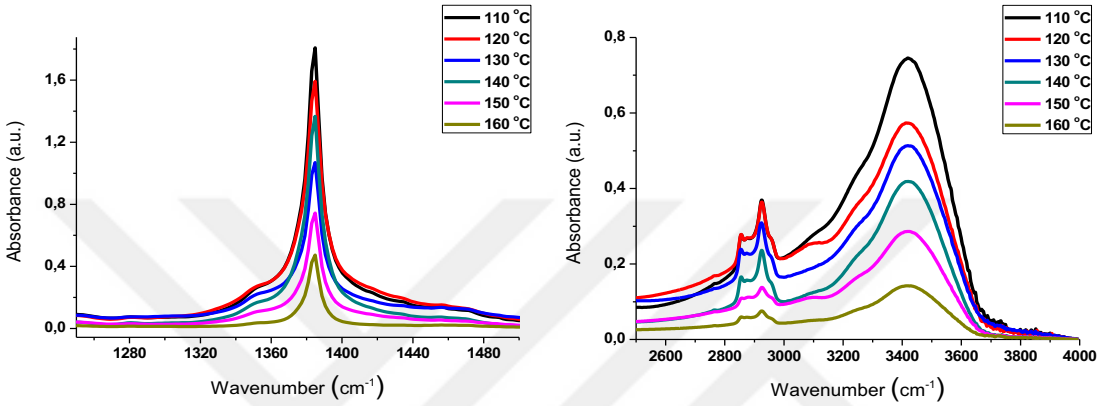

Figure 3.6.2 FT-IR spectra of the heated Mn(II) samples prepared using KBr. Nitrate absorbances (left), water, and surfactant absorbances (right).

3.7 Method Selection

Spin and drop-cast coatings have shown to form LLC mesophases at all three mole ratios. To make sure which method is more feasible for this work, both methods were used at 3:1 mole ratio for the synthesis of $LiMnPO_4$. The main difference between the spin and drop-casting methods is the removal of solvent from the media and the methods provide varying film or coating thicknesses. Differences in the film thickness and formation duration create significant differences in the calcination process of these samples. The speed of evaporation, burning of surfactant away from the system would be the important qualities of the method selected. Also, the purity of the sample formed after calcination is a criterion for deciding on the method. There are two items to it, the initial one is to make the sample of a single compound of lithium metal phosphate and the second one to make sample in a single form, either crystalline or amorphous.

As mentioned before if there is a formation of lithium metal phosphate nanoparticles in early stage of coating, it must be determined before moving further in the study. To select the proper method for the synthesis of $LiMPO_4$ (M = Mn(II), Fe(II), Co(II), and Ni(II)), the 3:1 mole ratio Mn(II) solution was spin coated and calcined at 250, 350, and 450^oC for 2, 4, 8, and 12 hours. The XRD patterns and SEM images were recorded to predict the proper method. Figures 3.7.1 to and 3.7.4 display a set of XRD patterns recorded at different temperatures and calcination durations of the Mn(II) system. First, coatings using both methods were calcined at 250^oC in an oven. The XRD patterns show that the structure is amorphous without a second phase in the drop-casted samples, see Figure 3.7.1. In the spin coated samples, only the one sample that was calcined for 12 hours has shown a possible second phase. Three diffraction lines are detected at 32.47, 34.33, and 48.11^o, 2θ. These lines were not matched with any

reference. After subtracting the instrumental broadening from the FWHM (full width half maximum) value of the lines, crystallite size calculated from Scherer equation to be around 4.3 nm.

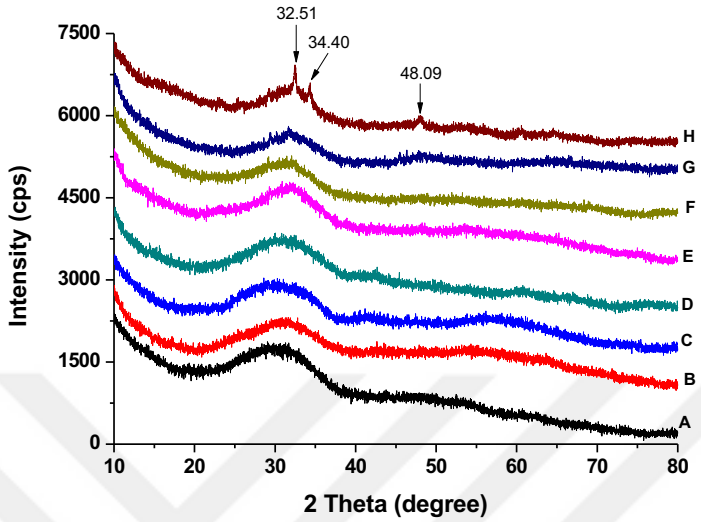

Figure 3.7.2 Wide angle XRD patterns of 3:1 samples of manganese prepared using both coating methods and calcined at 250°C. (A) dropcast coated sample calcined for 2 hours. (B) dropcast coated sample calcined for 4 hours. (C) dropcast coated sample calcined for 8 hours. (D) dropcast coated sample calcined for 12 hours. (E) spin coated sample calcined for 2 hours. (F) spin coated sample calcined for 4 hours. (G) spin coated sample calcined for 8 hours. (H) spin coated sample calcined for 12 hours.

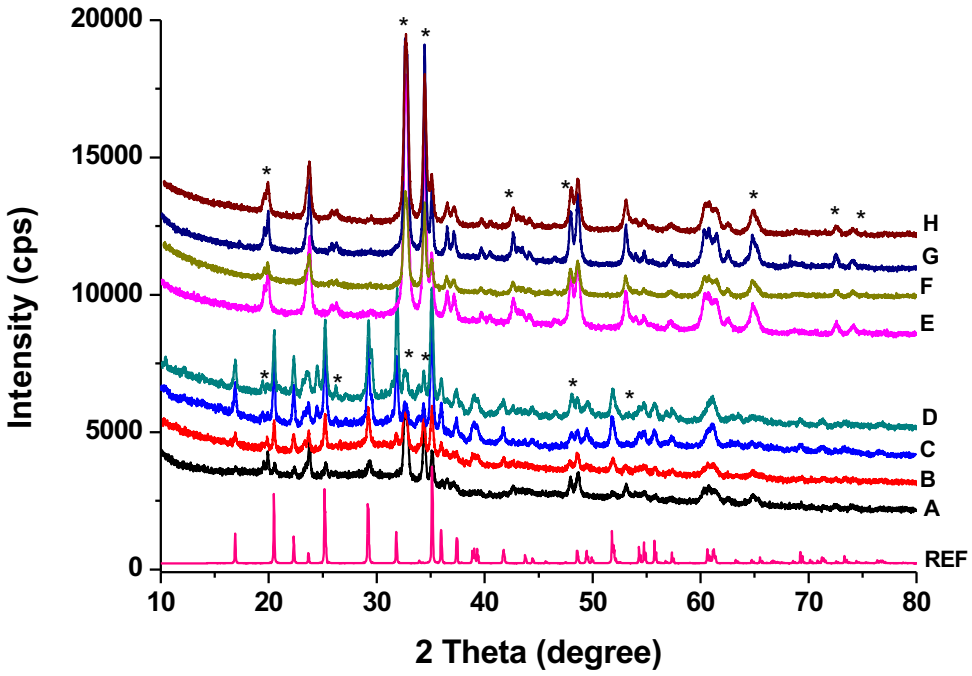

Figure 3.7.1 Wide angle XRD patterns of 3:1 samples of manganese prepared using both methods calcined at 350°C. (A) dropcast coated sample calcined for 2 hours. (B) dropcast coated sample calcined for 4 hours. (C) dropcast coated sample calcined for 8 hours. (D) dropcast coated sample calcined for 12 hours. (E) spin coated sample calcined for 2 hours. (F) spin coated sample calcined for 4 hours. (G) spin coated sample calcined for 8 hours. (H) spin coated sample calcined for 12 hours. (*) shows signals those do not belong to the reference. Reference is of $LiMnPO_4$ (PDF Card No. 01-072-7844).

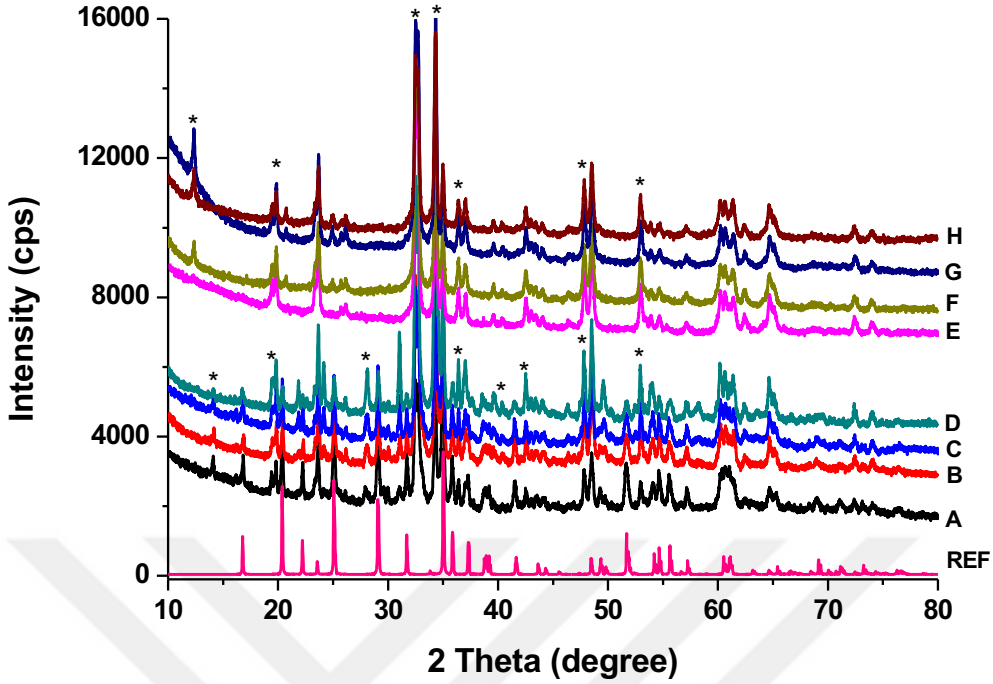

Figure 3.7.3 Wide angle XRD patterns of 3:1 samples of manganese prepared using both methods calcined at 450°C. (A) dropcast coated sample calcined for 2 hours. (B) dropcast coated sample calcined for 4 hours. (C) dropcast coated sample calcined for 8 hours. (D) dropcast coated sample calcined for 12 hours. (E) spin coated sample calcined for 2 hours. (F) spin coated sample calcined for 4 hours. (G) spin coated sample calcined for 8 hours. (H) spin coated sample calcined for 12 hours. (*) shows signals those do not belong to the reference. Reference is of $LiMnPO_4$ (PDF Card No. 01-072-7844).

The XRD diffraction of spin coated sample calcined at 250°C for 12 hours, supports the claim that there would be particles forming outside the main phase. Three diffraction lines in the sample are from a secondary phase which was, judged by the signal intensity, formed with very low yield. Yet the duration of time under the given temperature to form this secondary phase suggests that it will not be an issue for the purposes of this study. After heated to 350°C, these samples have become crystalline. The XRD patterns of the samples, prepared by drop-cast coating at this temperature matches to the reference data for the $LiMnPO_4$ (PDF Card No. 01-072-7844), however the samples are mixture of more than one phase. Several signals those do not belong to the $LiMnPO_4$ have been found in the diffraction pattern. These signals are found to be matching a different phosphate product. Instead of staying as the lithium metal phosphate, phosphate anion has reacted into a pyrophosphate and within the reaction, rearranged the ionic balance. As a result, there is also $Li_2MnP_2O_7$ present in the samples as a second phase. The pyrophosphate usually forms around 250°C. The formation of pyrophosphate is only so much in the drop-cast coated samples, it can only be considered as impurity. Indexing most of the diffraction lines to various planes of olivine structure of $LiMnPO_4$ show that we have successfully synthesised $LiMnPO_4$ by using drop-cast coating method. On the other hand, we can also look at the signals those do not belong to the $LiMnPO_4$. Some of the lines at 19.85, 32.85, 34.20, 36.52, 37.13, 48.09, and 53.09 can be indexed to (120), (222), (-313), (213), (-421), (224), and (-613) planes of $Li_2MnP_2O_7$, respectively These signals show the presence of the second phase and identify it as stated. Spin coated samples formed a completely different ratio of compounds than drop-cast coated samples, see Figure 3.7.5, and they also have a second phase. The second phase forms after 2 hours of calcination with the main phase. The diffraction lines gain intensity with further annealing at 350°C. These samples did not form

$LiMnPO_4$ as major product, instead $Li_2MnP_2O_7$ (PDF Card No. 00-058-0738) formed and the $LiMnPO_4$ phase appear as a secondary phase with signals at 23.77 and 48.65°, 2θ, originating from (011) and (022) planes. XRD patterns of the spin-coated and drop-cast coated samples, calcined at 450°C, are similar to the ones, calcined at 350°C, which allows us to say that there is no other phase as a tertiary product. In the case of drop-cast coating, the diffraction line at 12.14°, 2θ, that did not exist in the samples calcined at 350°C, belongs to $Li_2MnP_2O_7$'s (110)

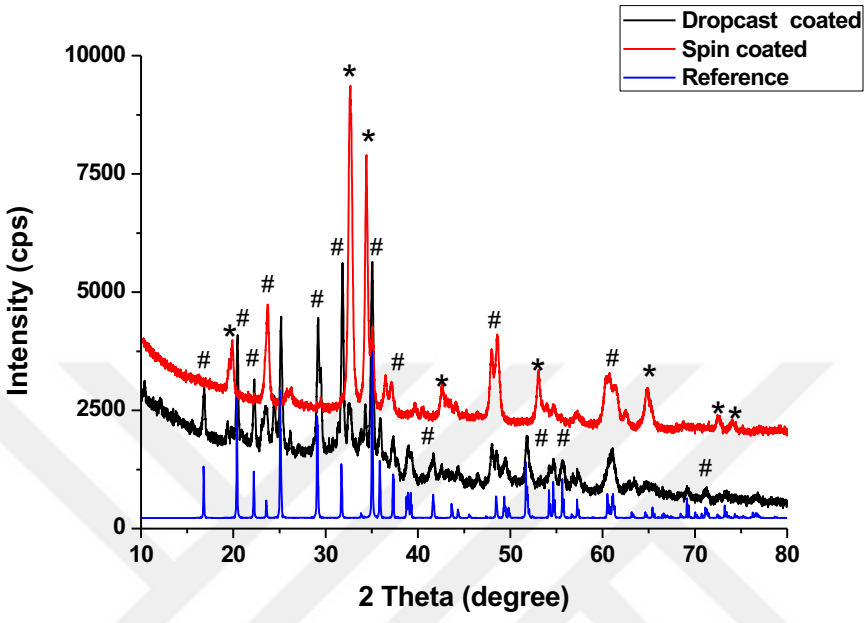

Figure 3.7.4 Wide angle XRD patterns of 3:1 samples of Mn(II) prepared using spin and drop-casting methods. Samples calcined at 350°C. (#) shows signals belong to the LiMnPO4 and (*) shows signals those do not. Reference is of $LiMnPO_4$ (PDF Card No. 01-072-7844).

plane. This evidence shows that the formation of pyrophosphate around that temperature. At 450°C, by comparing the relative intensities of both compounds, it can be said that $LiMnPO_4$ turns into $Li_2MnP_2O_7$ and becomes major product with increasing temperature. These experiments have shown that the method employed would be the drop-cast coating. Even though the method has been decided, it is also crucial to know their effects on the particle shape, size, and general morphology. To observe the effect of coating methods on morphology, SEM images were collected from all samples. At 250°C, the particles are sphere like, see Figure 3.7.6-8. These particles did not change shape or size at 250°C during heating over time. In the drop-casted samples with an increase in temperature, at 350°C, pores on the samples become visible. Structures in sponge like morphology are resilient for 2, 4, and 8 hours long calcinations. The SEM images of the spin coated samples calcined at 350°C show much finer particles compared to the drop-cast samples, Figure 3.7.7. Morphology in the spin coated samples did not change even with calcination time lengths such as 12 hours, see Figure 3.7.7. At even higher temperatures, 450°C, the difference between two methods can be observed, see Figure 3.7.8. For 2 and 4 hours long calcination there is a significant difference between spin and drop-casting methods. Particles of drop-cast coatings are much larger compared to spin coated samples. The major difference in the samples calcined at low versus elevated temperature is their morphology. The particles are spherical at low temperature calcination and worm-like at higher temperatures, compare the images in Figures 3.7.6-8. The worm-like future is a good indication of mesostructure formation. Worm-like particles are impossible to from bulk materials, it only appears by templating inorganics with surfactants.

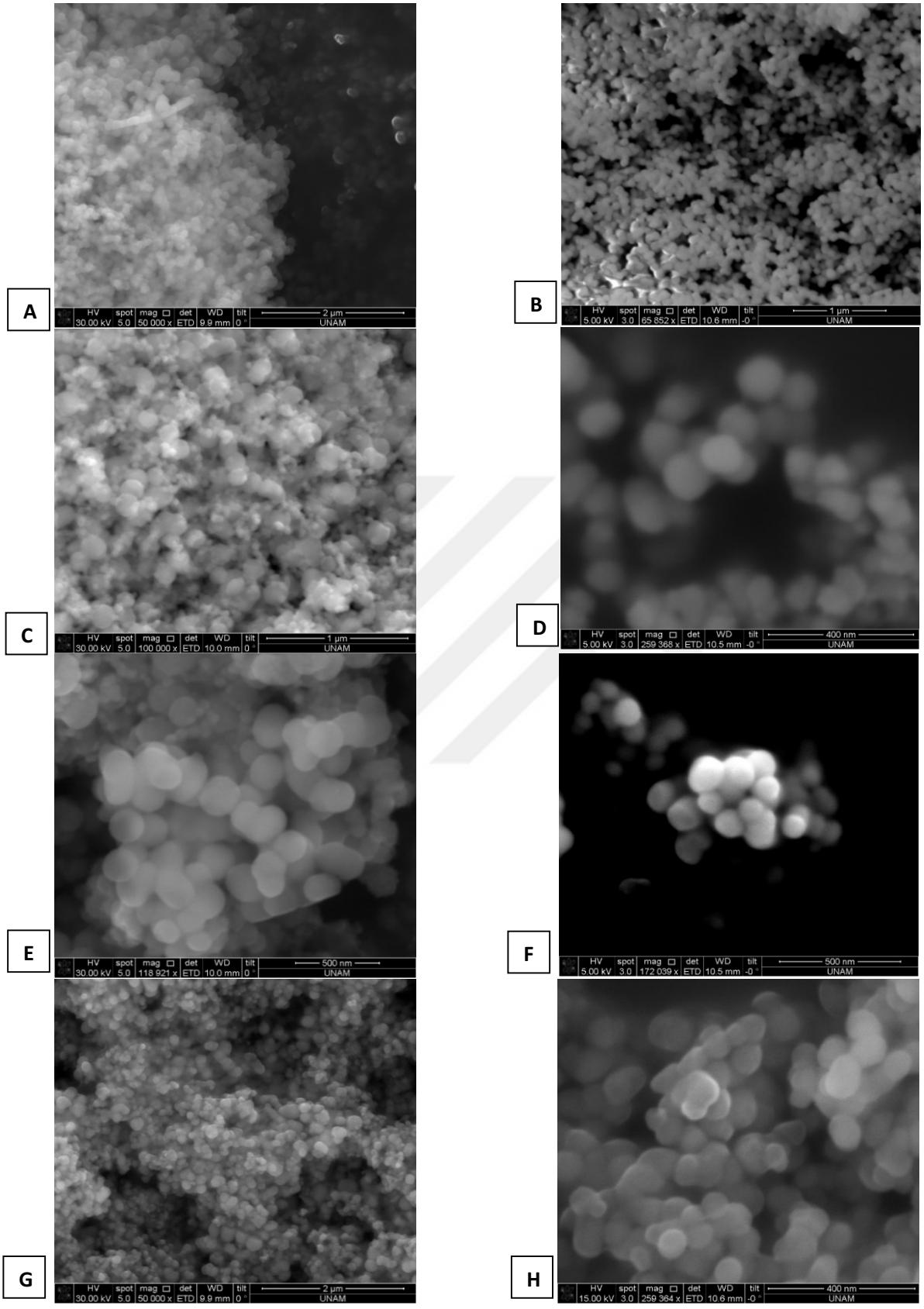

Figure 3.7.5 SEM images of samples those are drop-cast and spin coated and calcined at 250^{o}C from of 3:1 molar ratio of manganese solution. (A) dropcast coated for 2 hours, (B) spin coated for 2 hours, (C) dropcast coated for 4 hours, (D) spin coated for 4h, (E) dropcast coated for 8 hours, (F) spin coated for 8 hours, (G) dropcast coated for 12 hours, and (H) spin coated 12 hours.

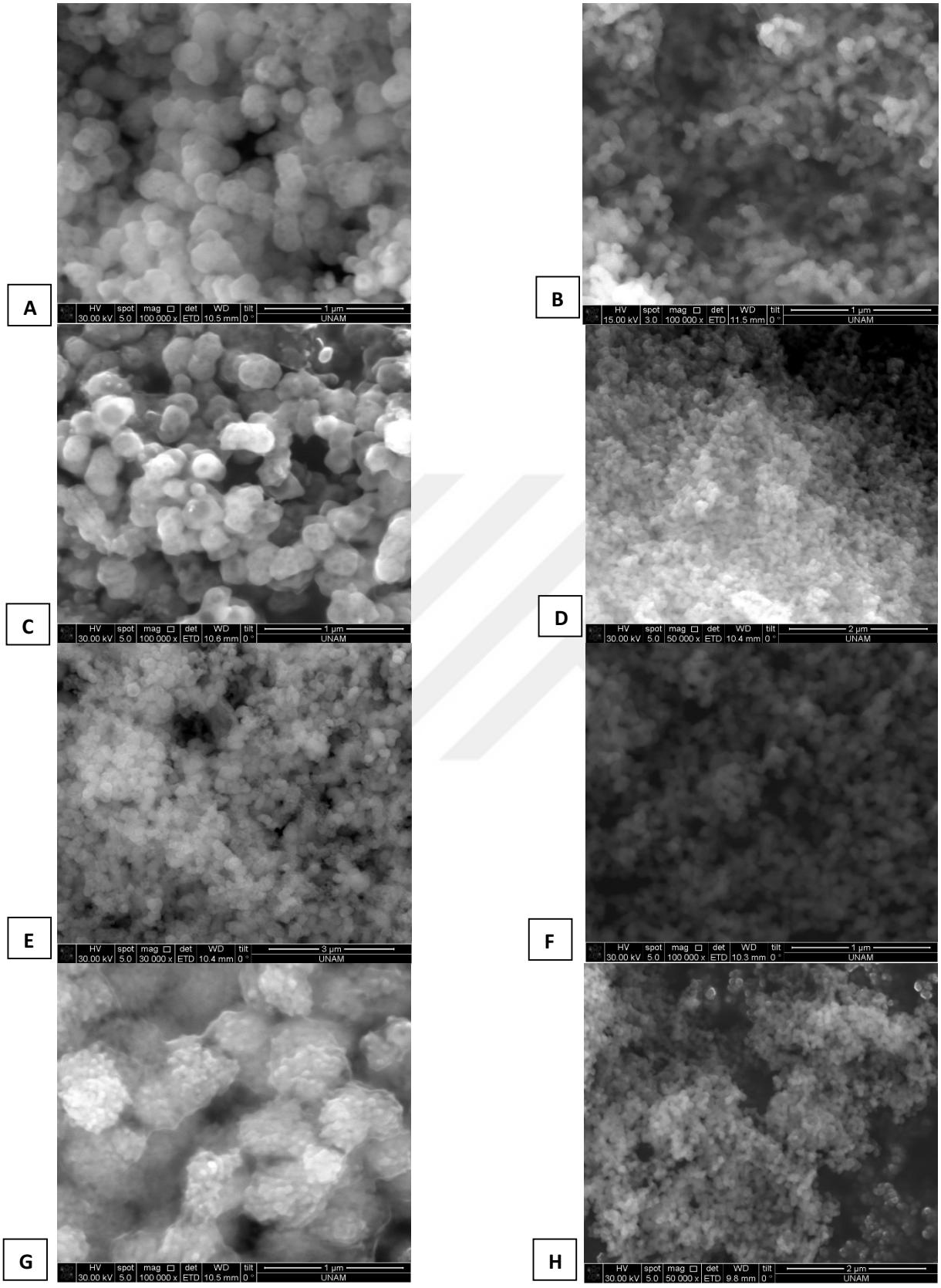

Figure 3.7.6 SEM images of samples those are drop-cast and spin coated and calcined at 350^{o}C from of 3:1 molar ratio of manganese solution. (A) dropcast coated for 2 hours, (B) spin coated for 2 hours, (C) dropcast coated for 4 hours, (D) spin coated for 4h, (E) dropcast coated for 8 hours, (F) spin coated for 8 hours, (G) dropcast coated for 12 hours, and (H) spin coated 12 hours.

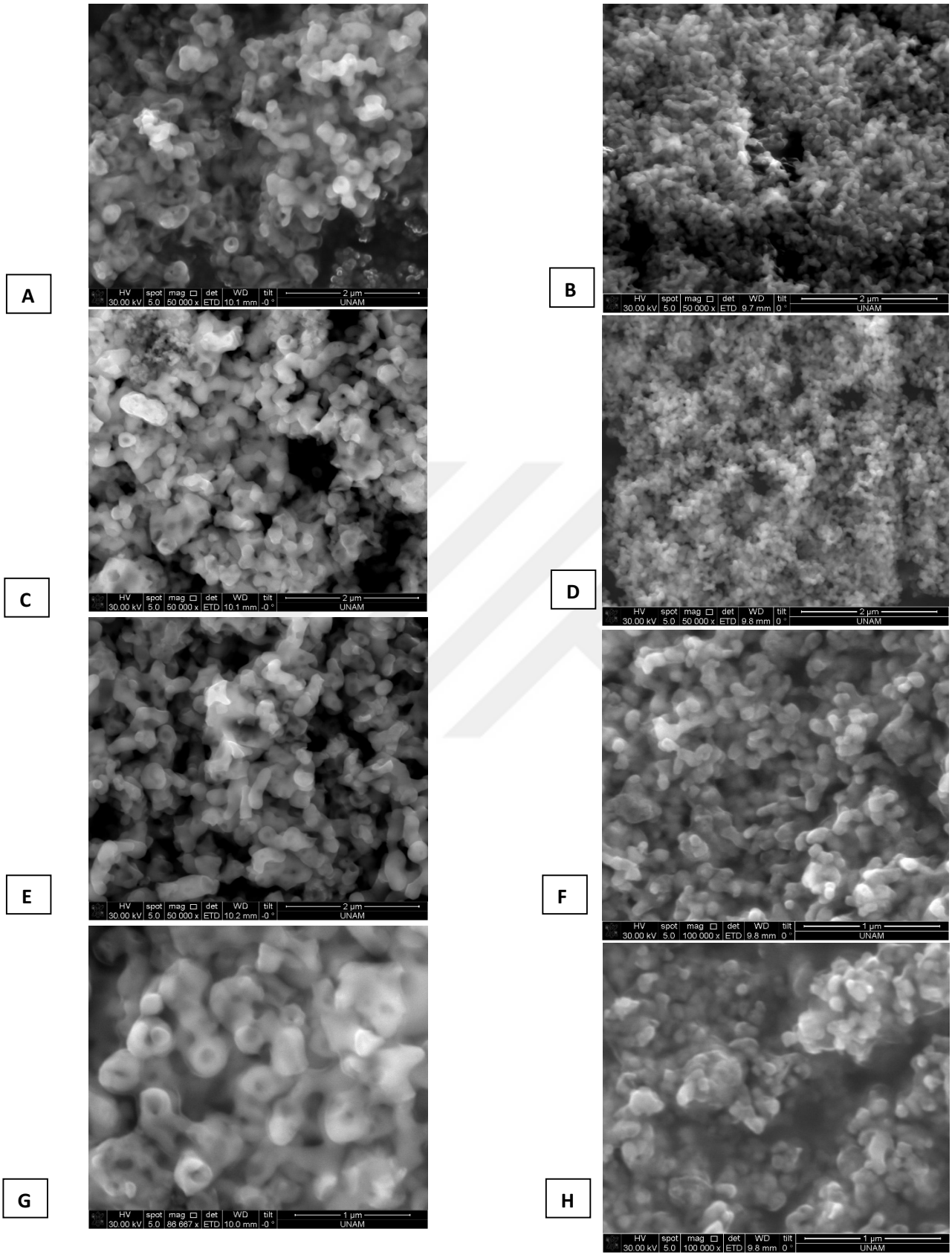

Figure 3.7.7 SEM images of samples those are drop-cast and spin coated and calcined at 450^{o}C from of 3:1 molar ratio of manganese solution. (A) dropcast coated for 2 hours, (B) spin coated for 2 hours, (C) dropcast coated for 4 hours, (D) spin coated for 4h, (E) dropcast coated for 8 hours, (F) spin coated for 8 hours, (G) dropcast coated for 12 hours, and (H) spin coated 12 hours.

3.8 Mesoporous Lithium Manganese Phosphate

Since drop-casting is found to be a more effective method, a set of samples were prepared by using solutions of 6:1 and 9:1 mole ratios by drop-casting method and calcined at 250, 350, and 450°C to test the role of ingredient concentration. We found that the LLC mesophase forms without salt crystallization at both salt concentrations. The 6:1 mole ratio sample is like the 3:1 ratio; there was only amorphous structure. However, the 9:1 mole ratio samples showed a second phase in the XRD patterns upon calcination at 250°C, see Figure 3.8.1. The XRD patterns can be indexed to $LiMnPO_4$. At higher ingredient concentrations, our method produces crystalline $LiMnPO_4$ embedded within the amorphous phase at low calcination temperatures. If we compare both sets of data, the 9:1 mole ratio coatings produced an additional undesired crystal phase in addition to amorphous $LiMnPO_4$ phase. Sharp diffraction lines over the amorphous features are indication of the formation of bulk $LiMnPO_4$ in the solution phase. The solution phase produces small amount of bulk $LiMnPO_4$, however, the remaining ingredients form gel-phase upon coating and amorphous $LiMnPO_4$ upon calcination at low temperatures. The wide-angle diffraction of freshly coated sample of 9:1 ratio has shown that there is no crystal formation within the gel phase. So, the only explanation at this point is that there is a formation of bulk $LiMnPO_4$ during heating and/or evaporation stage. This little amount of bulk then crystallizes with temperature and provides the diffractions lines that we observe, see Figure 3.8.1(B).

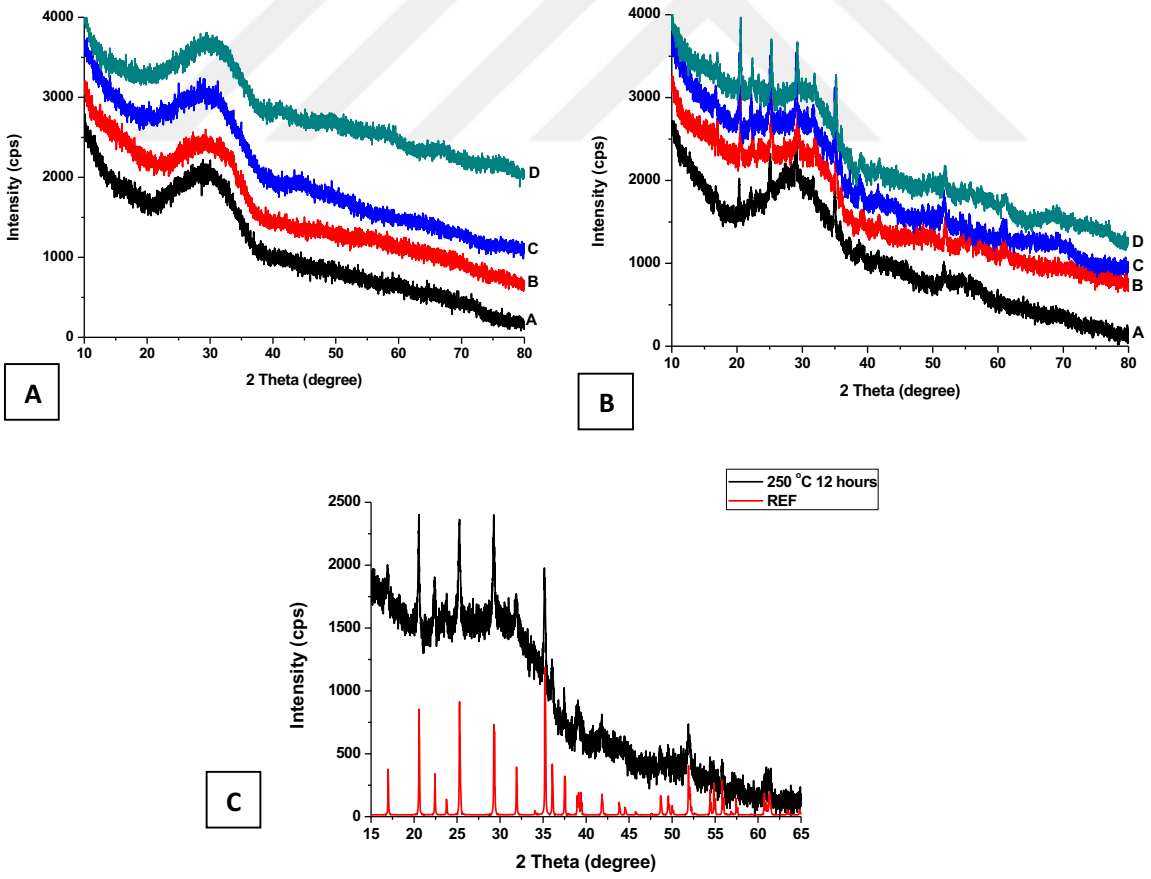

Figure 3.8.1 The XRD patterns of the 6:1 (A) and 9:1 (B & C) mole ratio Mn(II) samples, calcined at 250°C with different durations. (A) sample calcined for 2 hours. (B) sample calcined for 4 hours. (C) sample calcined for 8 hours. (D) sample calcined for 12 hours. Reference is of $LiMnPO_4$ (PDF Card No. 01-072-7844).

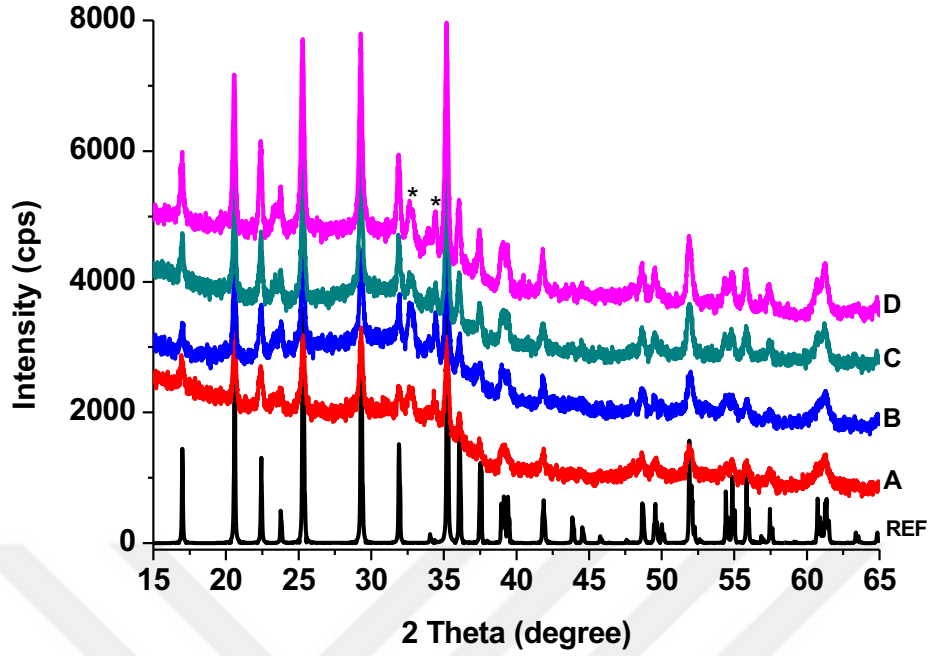

Figure 3.8.3 The XRD patterns of the 6:1 mole ratio Mn(II) samples, calcined at 350°C with different durations. (A) sample calcined for 2 hours. (B) sample calcined for 4 hours. (C) sample calcined for 8 hours. (D) sample calcined for 12 hours. (*) labels signals those do not belong to $LiMnPO_4$. Reference is of $LiMnPO_4$ (PDF Card No. 01-072-7844).

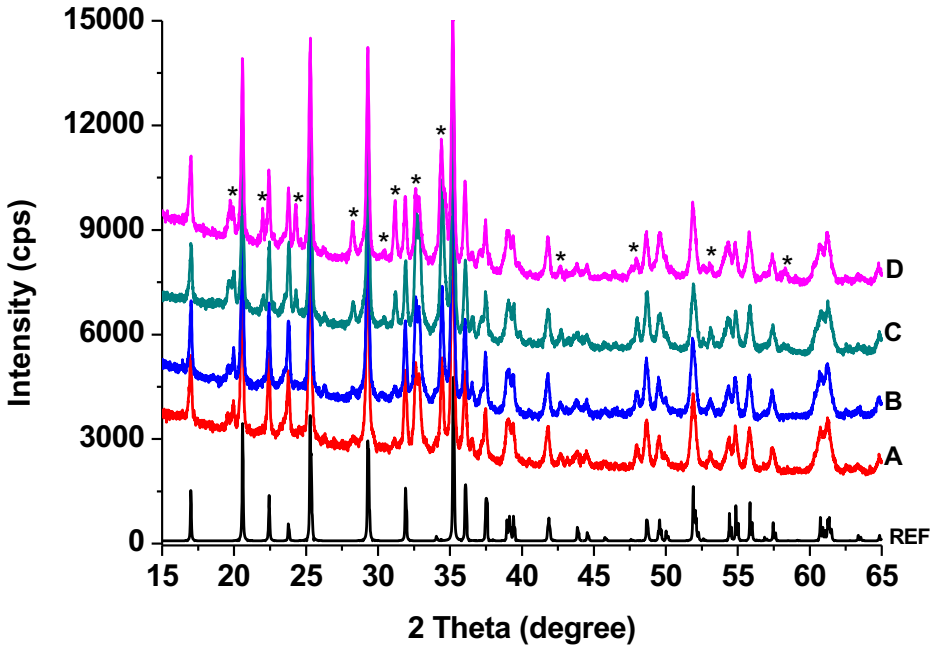

Figure 3.8.2 The XRD patterns of the 6:1 mole ratio Mn(II) samples, calcined at 450°C with different durations. (A) sample calcined for 2 hours. (B) sample calcined for 4 hours. (C) sample calcined for 8 hours. (D) sample calcined for 12 hours. (*) labels signals those do not belong to $LiMnPO_4$. Reference is of $LiMnPO_4$ (PDF Card No. 01-072-7844).

The formation of bulk particles, which then crystallized in the amorphous sample, has reduced the 9:1 ratio to a level of redundancy. Therefore, here on, the investigation has been continued using 6:1 ratio. This will also be the case for following metals (Fe, Co, Ni). The samples, calcined at 350°C, has shown the formation of another phase with two signals at 32.85 and 34.20°, 2θ, these signals are identical to those matched with $Li_2MnP_2O_7$, originated from [222] and [313] planes, respectively. Rest of the diffraction lines can be indexed to olivine $LiMnPO_4$. The trend of signals, those emerged from pyrophosphate phase, is regular with the rest of the sample. Samples are quite crystalline, and their intensity trends also match to the reference, as well.

Samples calcined at 450°C show XRD patterns, indexed to olivine $LiMnPO_4$ reference with some lines from the $Li_2MnP_2O_7$ phase, see Figure 3.8.3. There is also some amount of $Mn_3(PO_4)_2$ present in these samples. The diffraction lines with very low intensities, at 24.23, 28.44, 31.18, 34.45, 36.60, and 48.07°, 2θ, corresponds to [002], [-122], [-222], [-312], [-321], and [410] planes of $Mn_3(PO_4)_2$ (PDF Card No. 00-031-0827), respectively. It is also a crucial to point out that the lines at 24.42°, due to [220] plane of $Li_2MnP_2O_7$), 28.44 and 31.18°, 2θ (due to [-122] and [-222] planes of $Mn_3(PO_4)_2$) are diminishing with further annealing. This evidence shows, despite the high yield of desired phosphate product, at elevated temperatures, gel phase can form various products.

The IR spectra of the samples were also recorded using the samples calcined at 250, 350, and 450°C. The water peaks at 3400 cm^{-1} and 2900 cm^{-1} diminished noticeably with increasing temperature, see Figure 3.8.4. Presence of a large amount of water, even though these samples were heated to 250, 350, and 450°C, suggests that the material synthesised is porous with a significant surface area and the porosity decrease with increasing temperature. It is expected from these propositions that the elevated temperatures would increase the wall

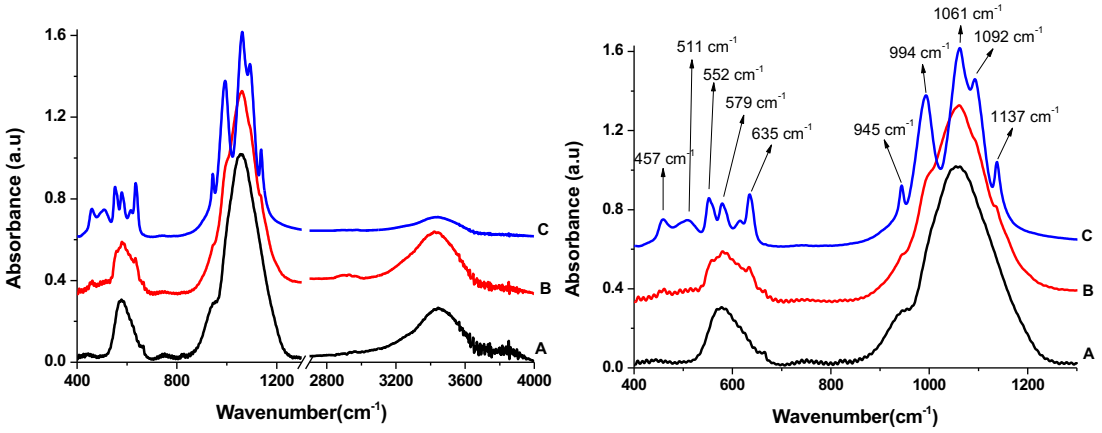

Figure 3.8.4 FTIR spectra of $LiMnPO_4$, prepared with 6:1 ratio, calcined at different temperatures. (A) 250°C, (B) 350°C, and (C) 450°C.

thickness, lowers the porosity and thus reducing the surface area. Main changes as the temperature increase are the amount of water present and the significant resolving of individual stretching and bending modes of phosphate, Figure 3.8.4. Asymmetric stretching modes are present at 1061, 1092, and 1137 cm^{-1}, while the symmetric stretching modes are

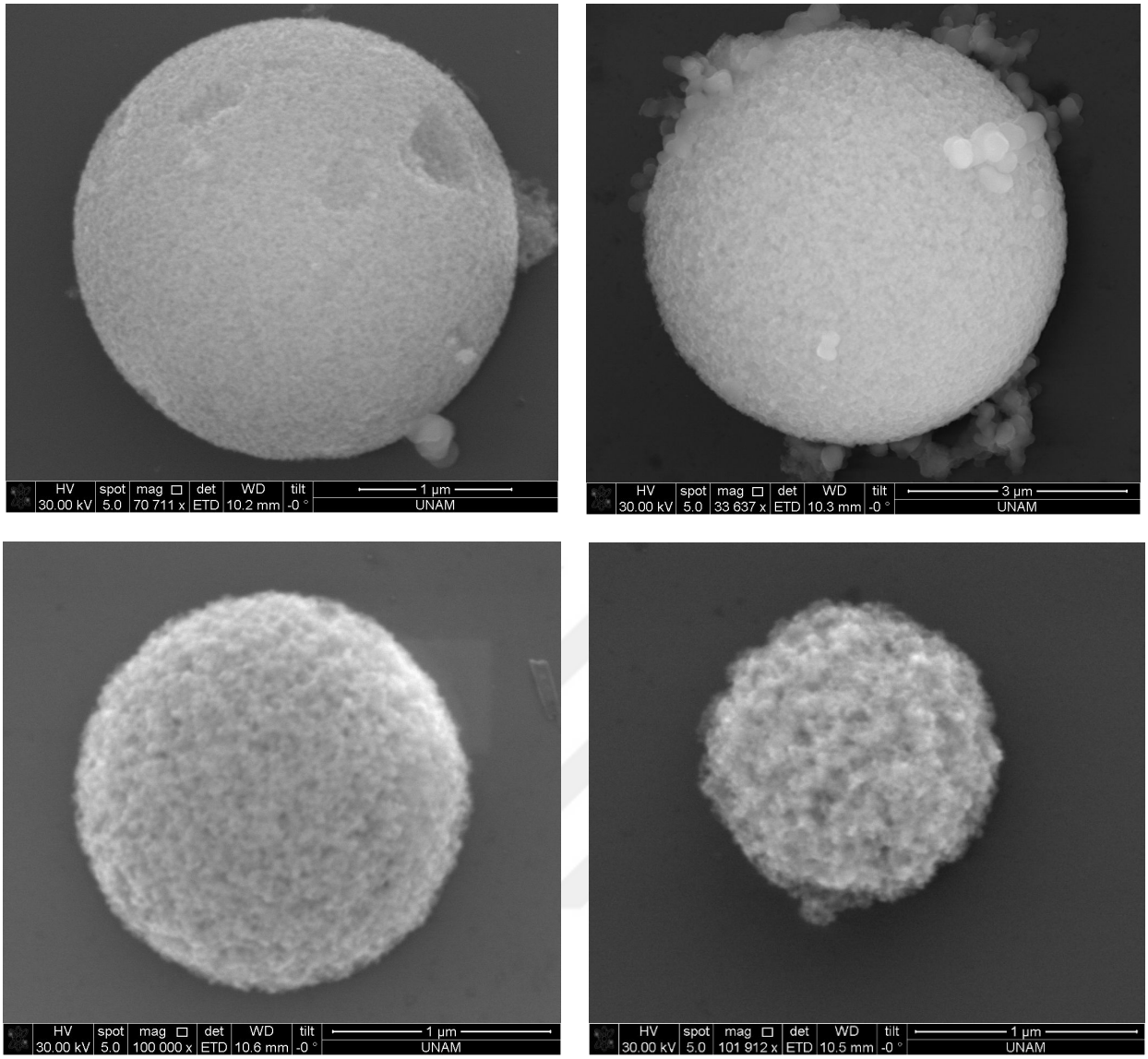

Figure 3.8.5 The SEM images of $LiMnPO_4$ samples, prepared from 6:1 mole ratio and calcined at 250^{o}C. Upper left; sample calcined for 2 hours. Upper right; sample calcined for 4 hours. Lower left; sample calcined for 8 hours. Lower right; sample calcined for 12 hours.

present at 945 and 994 cm^{-1}. Asymmetric bending modes have given signals at 635, 579, and 552 cm^{-1} and the symmetric bending modes are at 511 and 457 cm^{-1}, see Figure 3.8.5. The resolving of individual signals is an expected result since temperature increase also improves crystallinity of our samples. We have not been able to detect the characteristic signal of pyrophosphates [22] around 750 cm^{-1}, which shows that our initial statement on the small number of by-products is true, see Figure 3.8.4.

Figures 3.8.5-7 show a set of SEM images from $LiMnPO_4$ calcined at different temperatures and durations. Particles are spherical and become smaller with increasing calcination temperature. Notice also that the worm like structures could not form without the assistance of micellar mesophase. The images clearly show porous nature of the particles. From the XRD data, we know that there is no difference in the crystallite size with increasing calcination temperature, however the SEM images show that the structures are quite different. At a medium

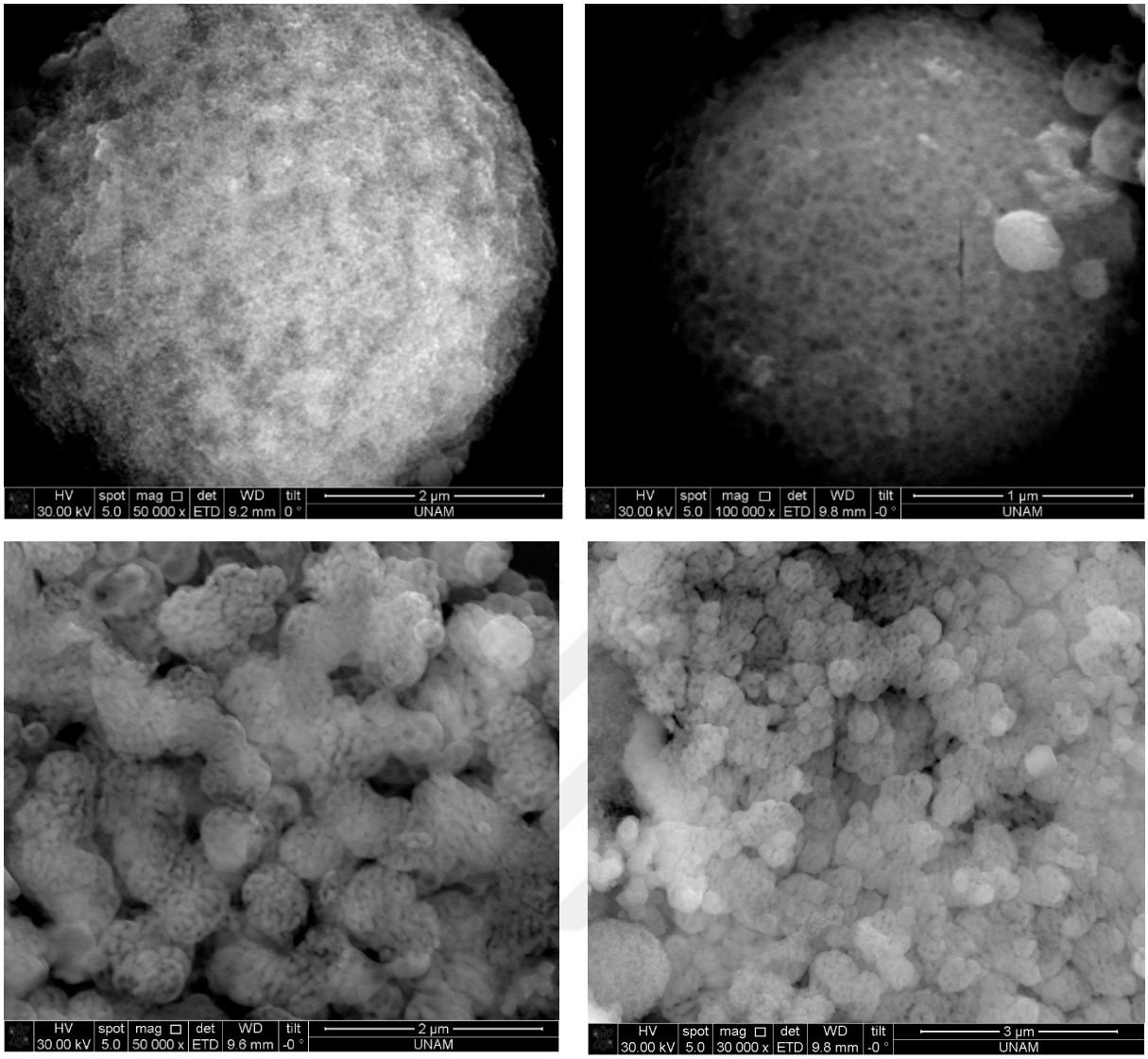

Figure 3.8.6 The SEM images of $LiMnPO_4$ samples, prepared from 6:1 mole ratio and calcined at 350^oC. Upper left; sample calcined for 2 hours. Upper right; sample calcined for 4 hours. Lower left; sample calcined for 8 hours. Lower right; sample calcined for 12 hours.

temperature, such as 250^oC, the particles and pores are well structured and have fine surfaces. As the calcination temperature increases the pores expand in the particles and cause deformation on the overall particle. These structural changes are clear result of the surfactant self-assembly. These investigations on the mesoporous $LiMnPO_4$ show that the porous structures are not stable at elevated temperatures that results a secondary and/or tertiary phase in the samples.

Samples, calcined at 350^oC, have kept their spherical shape. The pores are visible, and they have become more visible with increased calcination periods. Time lengths of 8 and 12 hours have almost worm like structures in particles. Although the structures look homogenous, from XRD results we know that these structures are not entirely made from the same material. However, it is also worth noting that the lack observation of different structures on individual samples indicates that the materials form inside the ever-expending walls of particles.

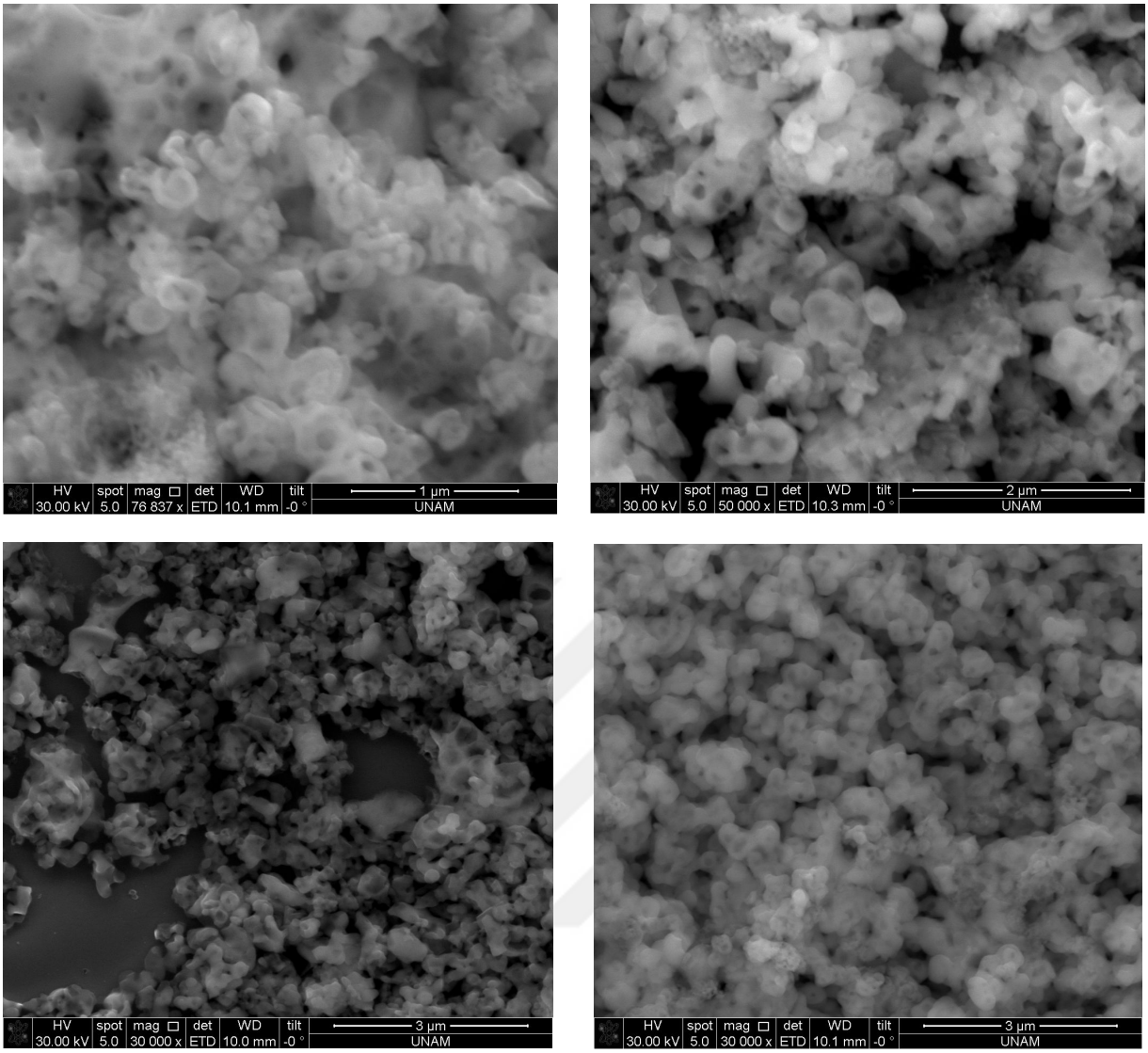

Figure 3.8.7 The SEM images of $LiMnPO_4$ samples, prepared from 6:1 mole ratio and calcined at 450^oC. Upper left; sample calcined for 2 hours. Upper right; sample calcined for 4 hours. Lower left; sample calcined for 8 hours. Lower right; sample calcined for 12 hours.

Calcinations conducted at 450^oC, do not have their spherical shape anymore. These samples are either circular or a bit cylindrical and others are short worm like, bent rods with holes on them, which also indicate that these structures could be hollow. From the XRD data, it is known that multiple compounds are present in these homogenous samples.

EDX spectrum shows that there are no impurities from outside. Though it cannot provide details on the compositions of the compounds within the sample, from there it is certain that the sample did not contain other transition metals. A bit of sodium present in the sample, however, with an atomic ratio of 1.73%, whereas, phosphate was 23.3%., likely due to some contamination during sample storage in the laboratory. The silicon signal comes from the silicon wafer, which was used as the sample holder in SEM imaging.

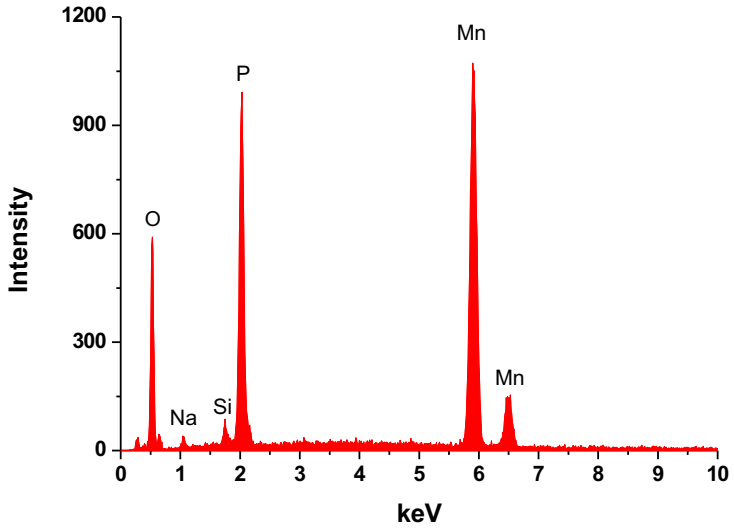

Figure 3.8.8 EDAX data gathered from the sample calcined at 350°C for 2 hours.

N_2 (77K) adsorption-desorption measurements were also conducted to elucidate the pore structure, and results have shown a correlation with the earlier claims. The H1 [23] hysteresis loop in isotherm of the sample, prepared at 250°C, shows that there are spherical pores, homogeneously distributed. This loop also shows that the pores are large with a thicker pore-walls, which in the end, is an indication of low surface area. Consisting with the isotherm, the BJH pore size distribution plot of the sample is heterogeneous. This has multiple reasons. First one being the aggregation of spherical particles in groups of four or five, which create a pseudo pore outside the particle that can hold N_2 molecules as if it was a pore. The latter is the actual pores inside the spheres themselves. Size of these pores are not precisely known however, they are around 3-5 nm diameter. Reason for low precision is the lack of data points around those values.

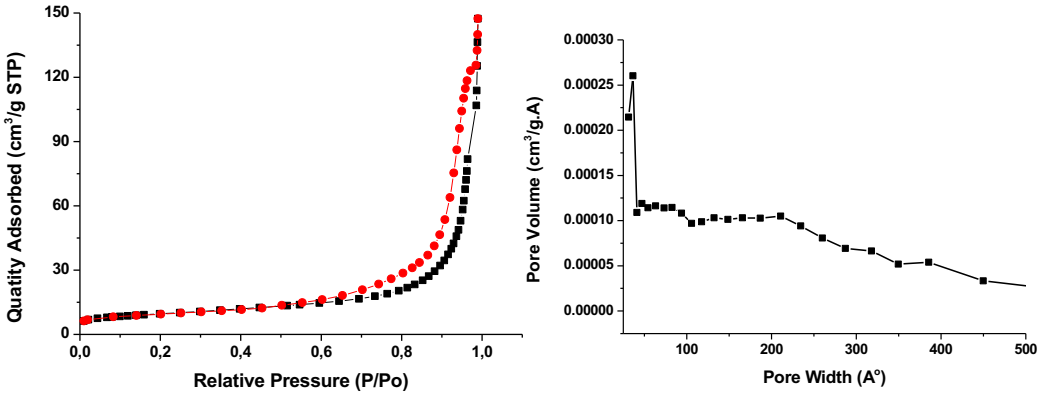

Figure 3.8.9 Linear isotherm plot of $LiMnPO_4$ sample (left) calcined at 250°C for 2 hours and pore size distribution (right).

At 250°C, this material has shown a BET surface area of 13 m^2/g. The BET surface area was considered since it is the only model that considers multi-layer adsorption. Later, the samples calcined at 350°C were used to measure the N_2-adsorption-desorption isotherm, see Figure 3.8.10. The isotherm shows a similar H1 [23] loop, with a better pore size distribution. At this temperature, the pores are, mostly, around 6-8 nm in diameter. However, they are still shallow and average size is affected by the pore imitating holes created b y adjacent spherical particles.

The BET surface area is 12 m^2/g. This is not an important change giving the assumptions made in the BET modelling. This states that the temperature has not affected the surface area, while almost the hysteria loop disappeared. The adsorption isotherm is type III, which indicates that there are, possibly, cylindrical pores and large pore diameter, allowing multi-layer adsorption to a level that the measurement would give the same surface area as the previous, measurement.

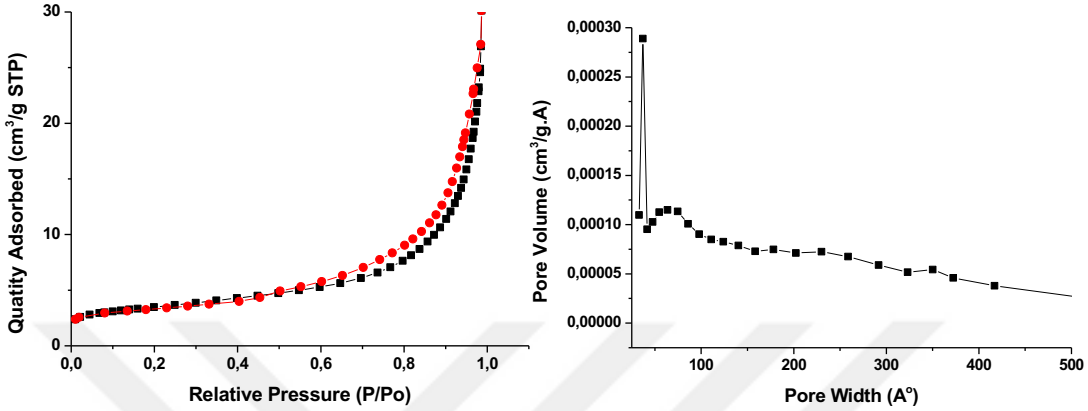

Figure 3.8.10 Linear isotherm plot of $LiMnPO_4$ sample (left) calcined at 350°C for 2 hours and pore size distribution (right).

Overall, though with low surface area, mesoporous $LiMnPO_4$ synthesised with quite high purity, according to our XRD measurements. The measurements of FT-IR, examinations under SEM, and N_2 adsorption-desorption measurements correlated each other. After the study of $LiMnPO_4$, other lithium metal phosphates were also prepared using 6:1 mole ratios of salts/surfactant and acid surfactant.

3.9 Mesoporous Lithium Iron Phosphate

After the synthesis of $LiMnPO_4$, lithium iron phosphate ($LiFePO_4$) was synthesised. The conditions for the synthesis kept the same as the ones used for the $LiMnPO_4$. The samples were synthesised from 6:1 mole ratio of clear Fe(II) solution (6:6:6:1, Li(I):Fe(II):H_3PO_4:$C_{12}E_{10}$). The samples were calcined at 250, 350, and 450°C for 2, 4, 8, and 12 hours. Figure 3.9.1 shows a set of XRD pattern of the samples calcined at 250°C and 350°C over time.

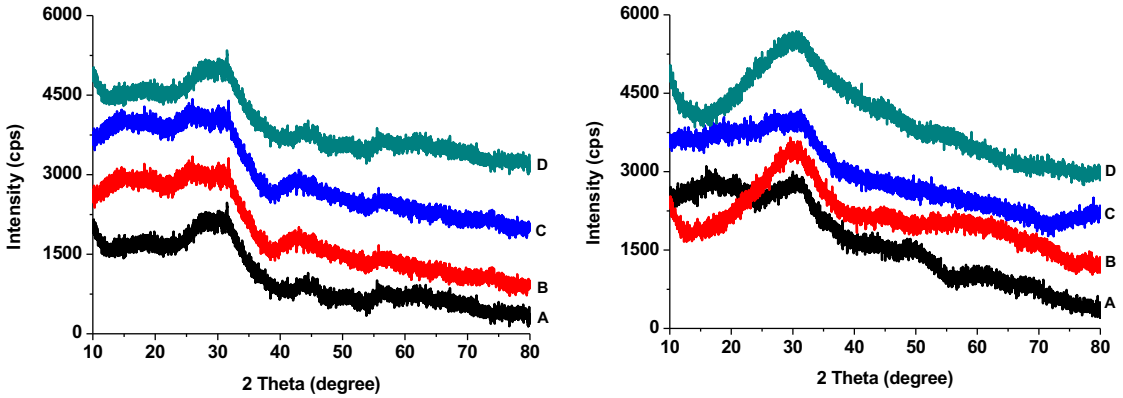

Figure 3.9.1 The XRD patterns of the 6:1 mole ratio Fe(II) samples, calcined at 250°C and 350°C with different durations. (A) sample calcined for 2 hours. (B) sample calcined for 4 hours. (C) sample calcined for 8 hours. (D) sample calcined for 12 hours.

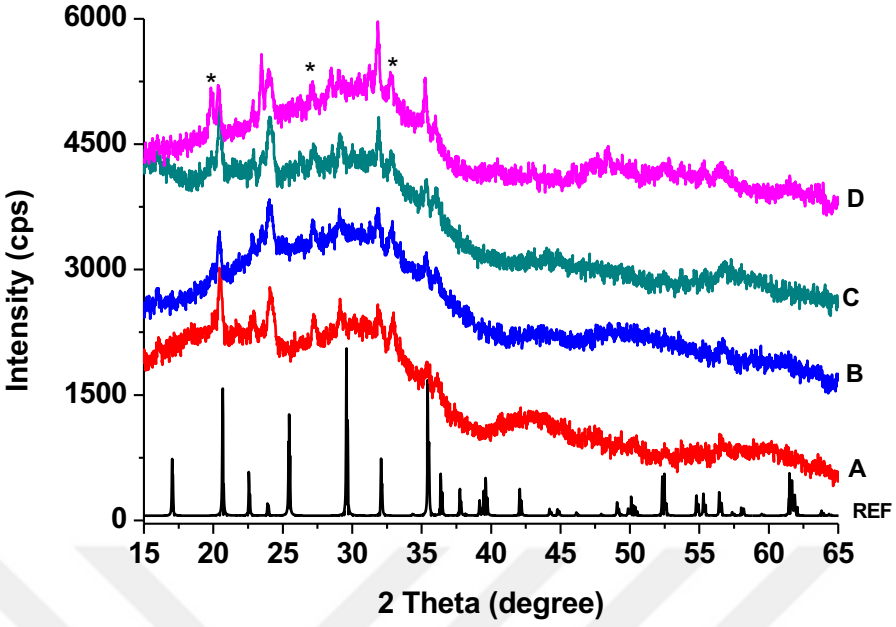

Figure 3.9.2 The XRD patterns of the 6:1 mole ratio Fe(II) samples, calcined at 450°C with different durations. (A) sample calcined for 2 hours. (B) sample calcined for 4 hours. (C) sample calcined for 8 hours. (D) sample calcined for 12 hours. Reference data shown in black for samples calcined at 450°C. (*) labels signals those do not belong to $LiFePO_4$. Reference is of LFP (PDF Card No.00-040-1499).

Signal diffraction line with very low intensity emerges at 31.52°, 2θ, at 250°C, the origin of this line is unknown. The XRD patterns of the Fe(II) samples show that at 250°C and 350°C, that samples are amorphous, Figure 3.9.1. However, they crystallize above 450°C, Figure 3.9.2. The patterns are indexed to $LiFePO_4$ with an exception of two lines, at 27.15, and 32.97°, 2θ. After calcination for 8h and 12h, some signals emerge without a significant elevation in the intensities of the signals already formed. However, most of the sample is still amorphous. The diffraction signals formed with increased calcination duration are; 19.88, 28.44, and 31.23°, 2θ. These do not belong to $LiFePO_4$. Therefore, the samples are abbreviated as LFP and will be used as LFP from this point on. The XRD diffraction pattern of LFP also states that we have reached the crystallization temperature, but a sizeable portion of the sample was still amorphous. This shows that the transition metal inside the lithium metal phosphate

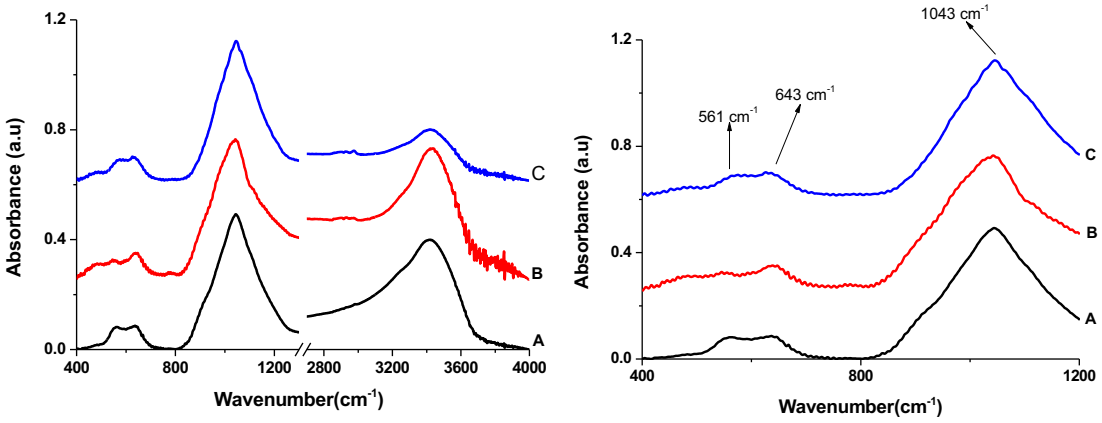

Figure 3.9.3 FTIR spectra of $LiMnPO_4$, prepared with 6:1 ratio, calcined at different temperatures. (A) 250°C, (B) 350°C, and (C) 450°C.

is really a determining factor in terms of crystallization temperature. The inability to assign the three diffraction signals to a certain compound and most of the samples being amorphous, limits the discussion on the crystal structure. The samples are mostly pure at the start. The second phase forms with temperature. This claim is from the trend of the second phase's diffractions line intensities. The diffraction line at 19.88^{o}, 2θ, was not even present until calcination length reached 12 hours. Intensity of this phase enhanced with increased time lengths for calcination. Hence, it can be said that these particles were not present at the start, formed later and then the initial phase started to act as precursor for this phase, under given temperature. Figure 3.9.3 display FT-IR spectra of the LFT samples, calcined at three different temperatures. The signal belonging to bulk water at 3400 cm^{-1} loses intensity as the calcination temperature increases. The phosphate signals are quite broad, which indicates that they are amorphous even at 450^{o}C. The peak at 1043 cm^{-1}, due to phosphate asymmetric stretching, dominates to the spectra. The bending signals at 561 and 643 cm^{-1} are also resolved in the spectra. Although the temperatures are quite high, there is a lack of highly resolved bending and stretching signals which indicates that on a small portion of the sample is crystalline and the rest of the sample is amorphous.

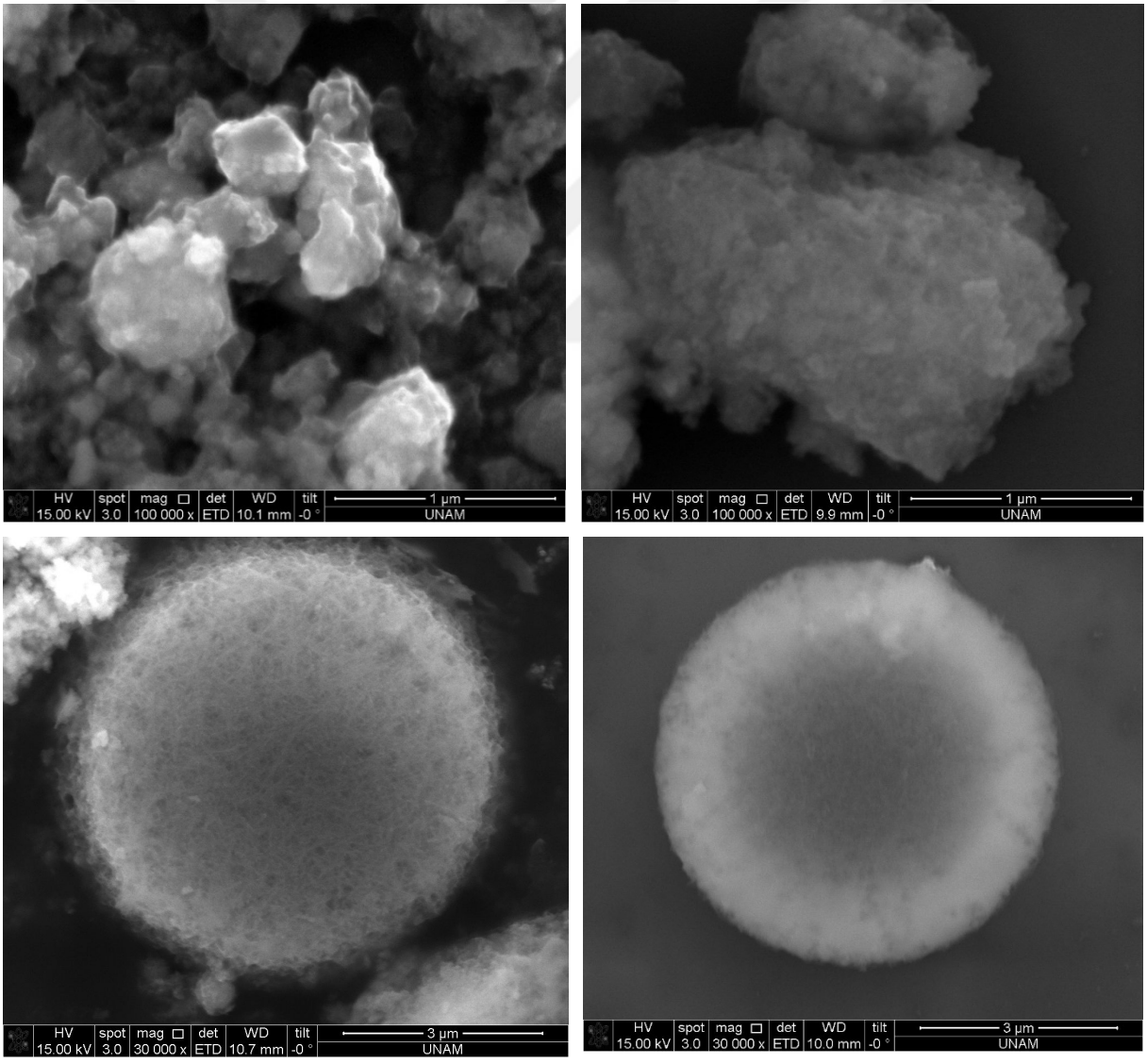

Figure 3.9.4 The SEM images of LFP samples, prepared from 6:1 mole ratio and calcined at 250^{o}C. Upper left; sample calcined for 2 hours. Upper right; sample calcined for 4 hours. Lower left; sample calcined for 8 hours. Lower right; sample calcined for 12 hours.

Samples of LFP that are calcined at 250^{o}C, adopt spherical shape as the duration of calcination elongates. Besides from the shape change the pore structure also changes and it is observed as time length changes. However, unlike the case of $LiMnPO_4$, the spheres of Fe(II), are more like a ball of yarn. Rather than holes in them, there are rod like particles aggregated into the shape of sphere. However, these particles form their defined shapes, well after the removal of surfactant. The removal of surfactant also confirmed by the FT-IR measurement.

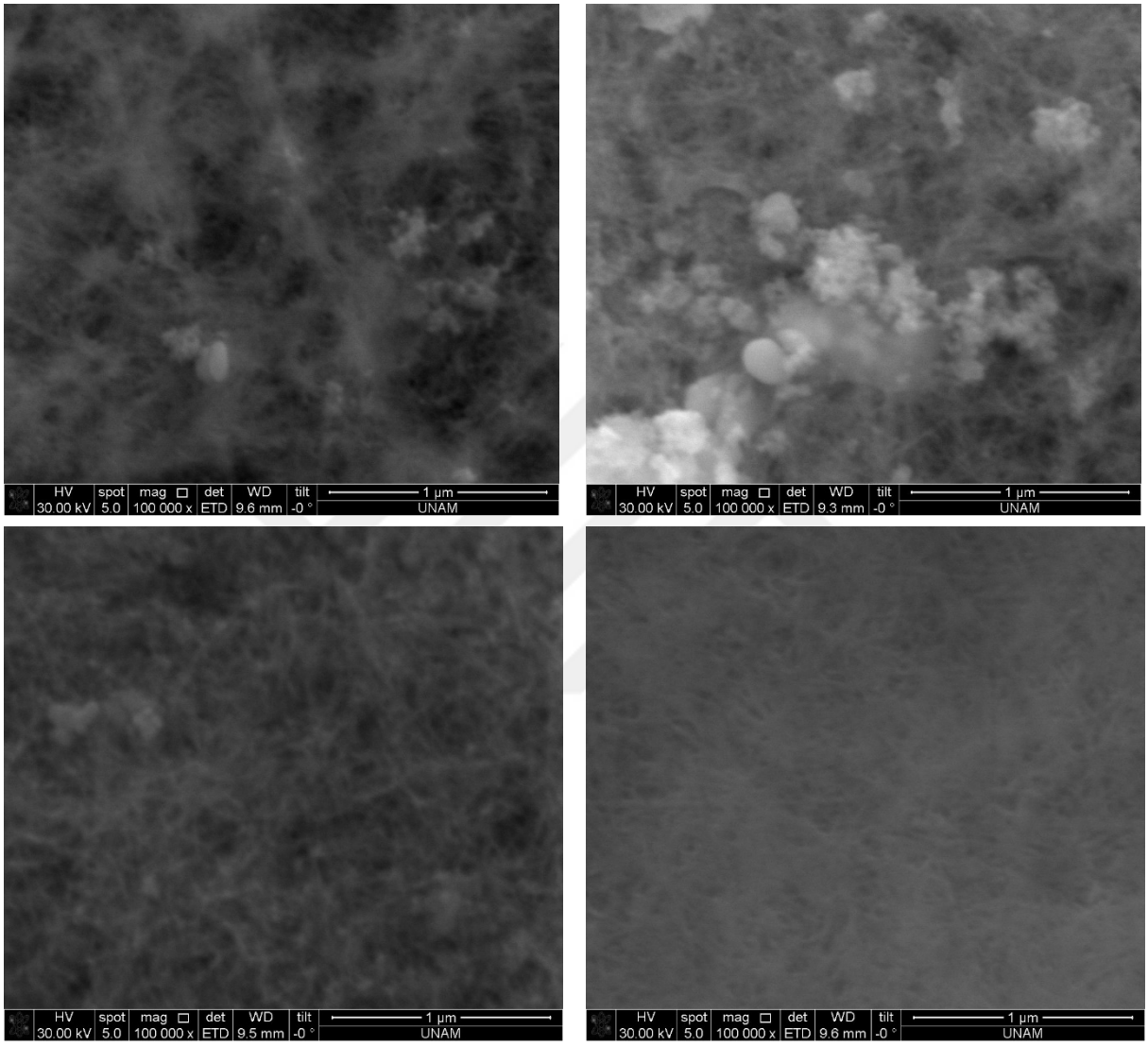

Figure 3.9.5 The SEM images of LFP samples, prepared from 6:1 mole ratio and calcined at 350^{o}C. Upper left; sample calcined for 2 hours. Upper right; sample calcined for 4 hours. Lower left; sample calcined for 8 hours. Lower right; sample calcined for 12 hours.

Samples calcined at 350^{o}C also shown fibre like threads is their structure. In the sample calcined for 2 hours, there is a significant volume of empty space present, this space gets contacted as the time length of calcination increases. This also shows the surfactant was not able to form the usual sphere like particles for the LFP.

After temperature reaches 450^{o}C, the samples go into a drastic change with calcination duration. At first, there is a film like structure with quite large holes on it. As duration changes, these holes start to disappear, and aggregation of very small particles take place. Further calcination, then, creates very smooth film like structure, however, the

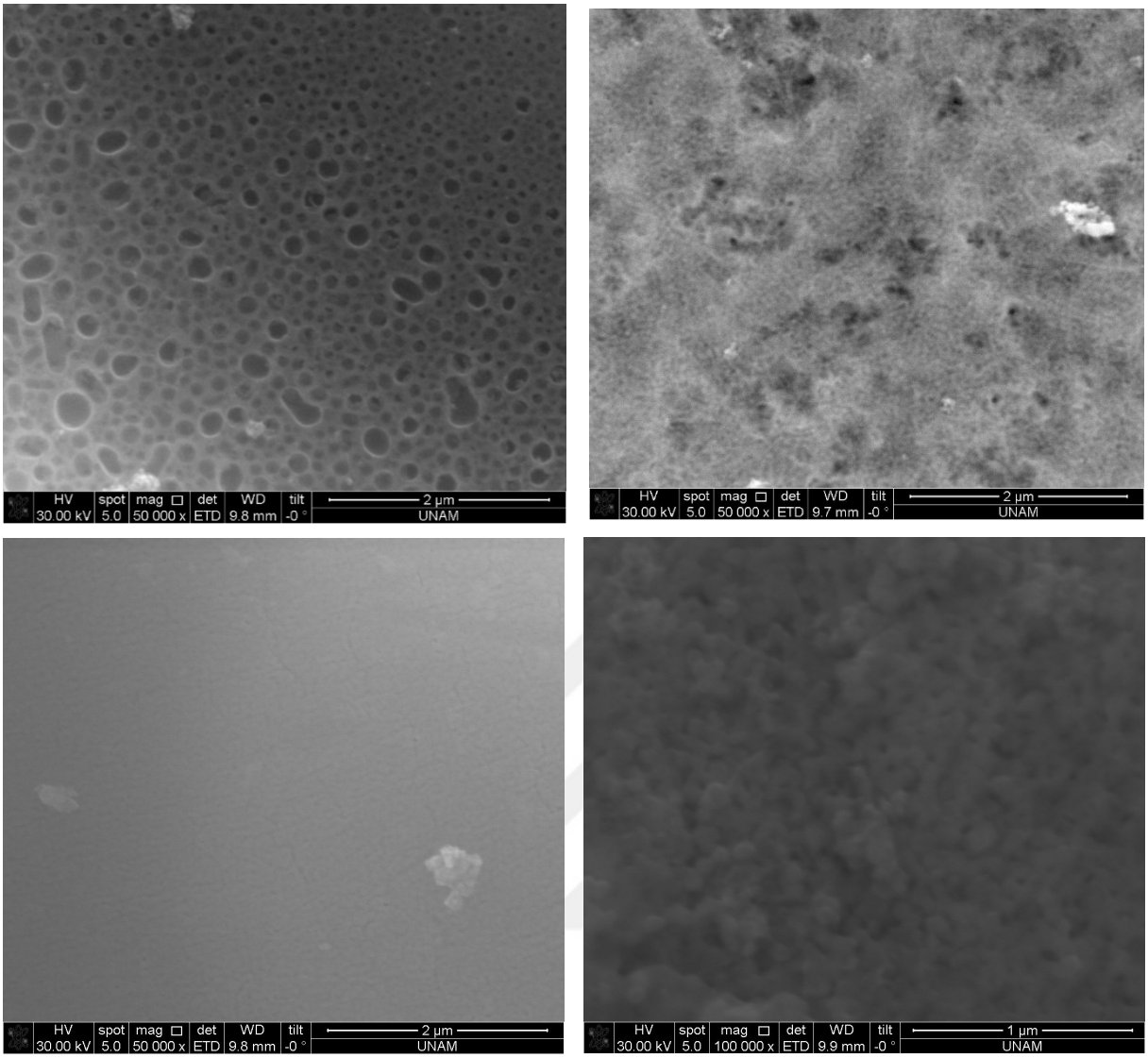

Figure 3.9.6 The SEM images of LFP samples, prepared from 6:1 mole ratio and calcined at 450^{o}C. Upper left; sample calcined for 2 hours. Upper right; sample calcined for 4 hours. Lower left; sample calcined for 8 hours. Lower right; sample calcined for 12 hours.

aggregated particles are still visible. In final sample where the calcination duration has reached to 12 hours, this film like structure further aggregates into larger particles. These particles are sphere like, but heterogeneous.

The EDX data provides information on evolution of carbon and chlorine, change in phosphor - oxygen ratio and sodium contamination. Starting with carbon evolution, this was an expected case as it was confirmed many times, here confirmed once again, carbon species removed with temperature. The 15.4% atomic ratio of carbon drops to undetectable levels after raising temperature to 350^{o}C. The chlorine removal is also a very important point in this study since the iron (II) chloride was the source. The 1.8% of chlorine ratio drops to 1.1% as temperature is raised from 250 to 350^{o}C. Then chlorine disappears completely. There is a notable change in the signals of oxygen and phosphor atoms.

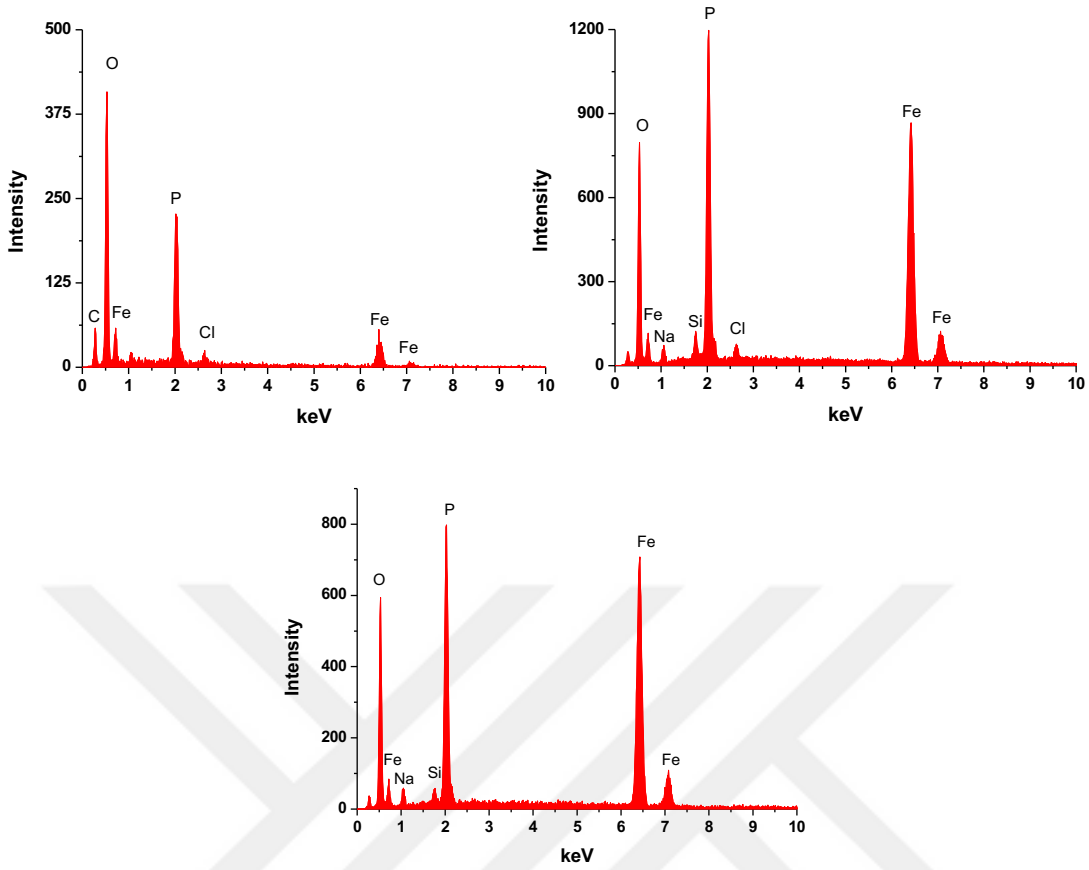

Figure 3.9.7 EDX data gathered from LFP samples calcined at 250 (upper left), 350 (upper right), 450°C (bottom).

The N_2 adsorption-desorption isotherms provide surface properties. The H3 [23] type pores**,** which are slit like structures formed by aggregated or plate like particles are present in the sample. The pore size distribution also correlates well with it. It is heterogeneous, and most pores are larger than 10 nm. The sample is mesoporous at this temperature, with a surface area of 56 m^2/g.

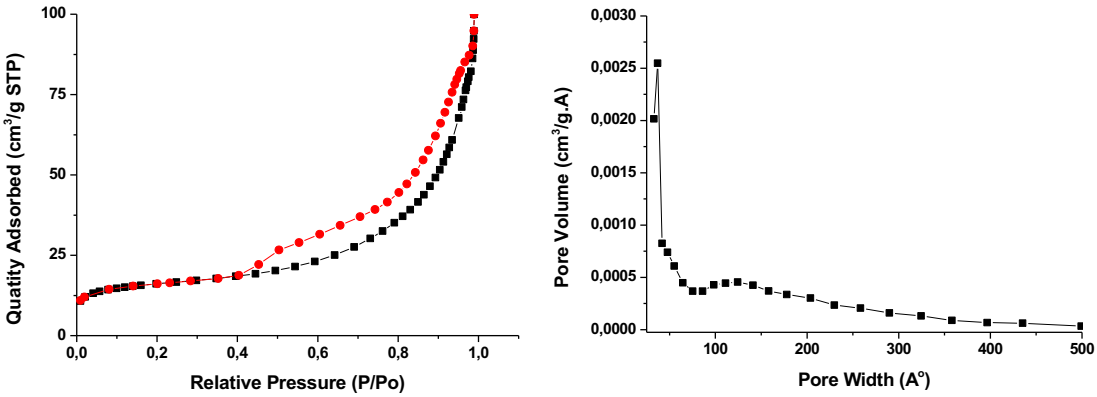

Figure 3.9.8 Linear isotherms of LFP sample, calcined at 250°C for 2 hours. Isotherm (left) and pore size distribution plot (right).

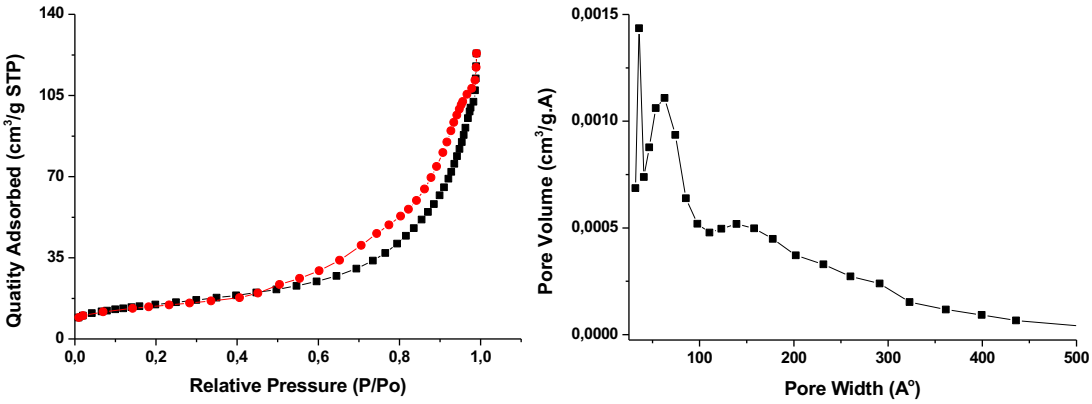

Figure 3.9.9 Linear isotherm plot of the LFP sample, calcined at 350°C for 2 hours. Isotherm (left) and pore size distribution plot (right).

At 350°C, sample keeps its classification and stays in H3 [23] type hysteria loop, but the pore size converges around 6-7 nm. This sample has a surface area of 53 m^2/g. Like $LiMnPO_4$, LFP also stands robust towards temperature. This sample has shown even more thread like structures than the previous one. But the unification pore may indicate that the 350°C is a better option to make mesoporous LFPs.

3.10 Mesoporous Lithium Cobalt Phosphate

For the synthesis of $LiCoPO_4$, clear solutions of 6:1 mole ratio (6:6:6:1, Li(I):Co(II):H_3PO_4:$C_{12}E_{10}$) were used. The conditions for the synthesis was kept the same as the ones used for the Mn(II). The drop-casted samples were calcined at 250, 350, and 450°C for 2, 4, 8, and 12 hours' durations and analysed using XRD, SEM, and FTIR techniques.

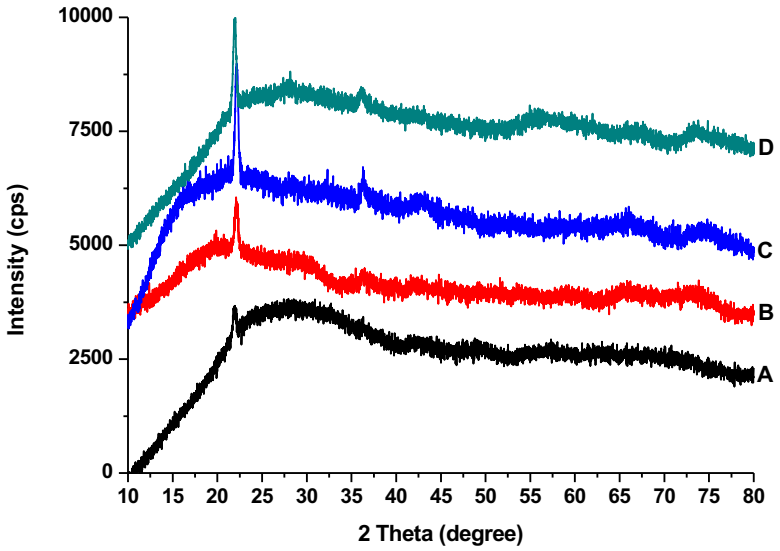

Figure 3.10.1 The XRD patterns of the 6:1 mole ratio Co(II) samples, calcined at 250°C for different durations. (A) sample calcined for 2 hours. (B) sample calcined for 4 hours. (C) sample calcined for 8 hours. (D) sample calcined for 12 hours.

Samples, calcined at 250°C, display a diffraction line at 22.15°, 2θ, see Figure 3.10.1. The origin of this line is unknown. There is no other signal to assign the crystal structure of this unknown specie. At the calcination durations of 8 and 12 hours, there is another diffraction line, emerging at 36.32°, 2θ, though it is still not enough to make a satisfactory assignment. Crystallinity emerges at 350°C, see Figure 3.10.2. The diffraction lines from the samples, calcined at 350°C, can be indexed to olivine $LiCoPO_4$ (PDF Card No. 00-032-0552). However, there are four other lines that are not matching the reference data. Two of these lines at 20.09 and 35.29°, 2θ, emerges starting from the calcination duration of 2 hours. After 12 hours of calcination two more lines appear, at 24.08 and 29.02°, 2θ. The diffraction pattern shows that the 4 hours' calcination provides the highest yield of the crystalline $LiCoPO_4$. The samples, calcined at 450°C, have even higher crystallinity, however there is also more unidentified lines emerging, indicating that the product is changing from $LiCoPO_4$ to unknown specie(s), see Figure 3.10.3. The origin of the change can be either due to decomposition of $LiCoPO_4$ or crystallization of the secondary phases during annealing.

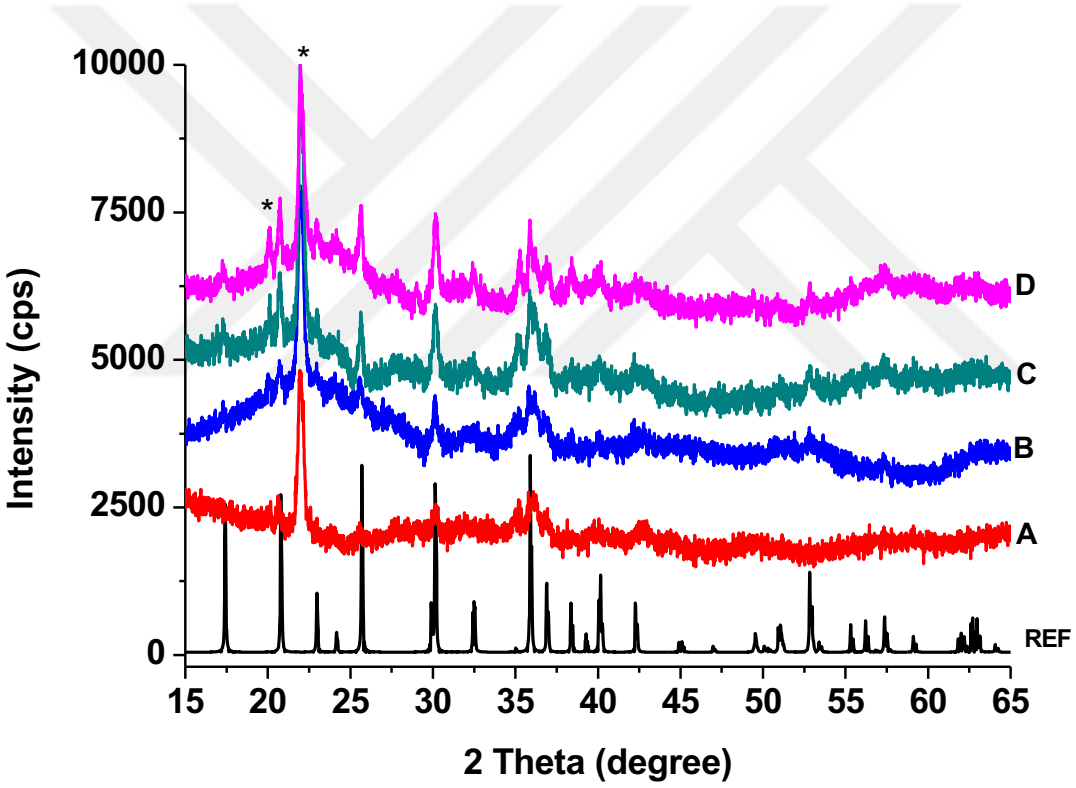

Figure 3.10.2 The XRD patterns of the 6:1 mole ratio Co(II) samples, calcined at 350oC for different durations. (A) sample calcined for 2 hours. (B) sample calcined for 4 hours. (C) sample calcined for 8 hours. (D) sample calcined for 12 hours. Reference is of $LiCoPO_4$ (PDF Card No. 00-032-0552).

The $LiCoPO_4$ samples were further analysed using FT-IR spectroscopy. The samples were calcined at 3 different temperatures and their KBR pellets were used to collect the spectra, see Figure 3.10.4. At 450°C, the signals are well-resolved to identify them. The peaks at 1147, 1103, and 1062 cm^{-1} are originating from the asymmetric stretching mode of the phosphate, others at 1001 and 945 cm^{-1} are from the symmetric stretching, see Figure 3.10.4. The asymmetric bending modes of phosphate are observed at 644, 580, and 548 cm^{-1}. The symmetric bending

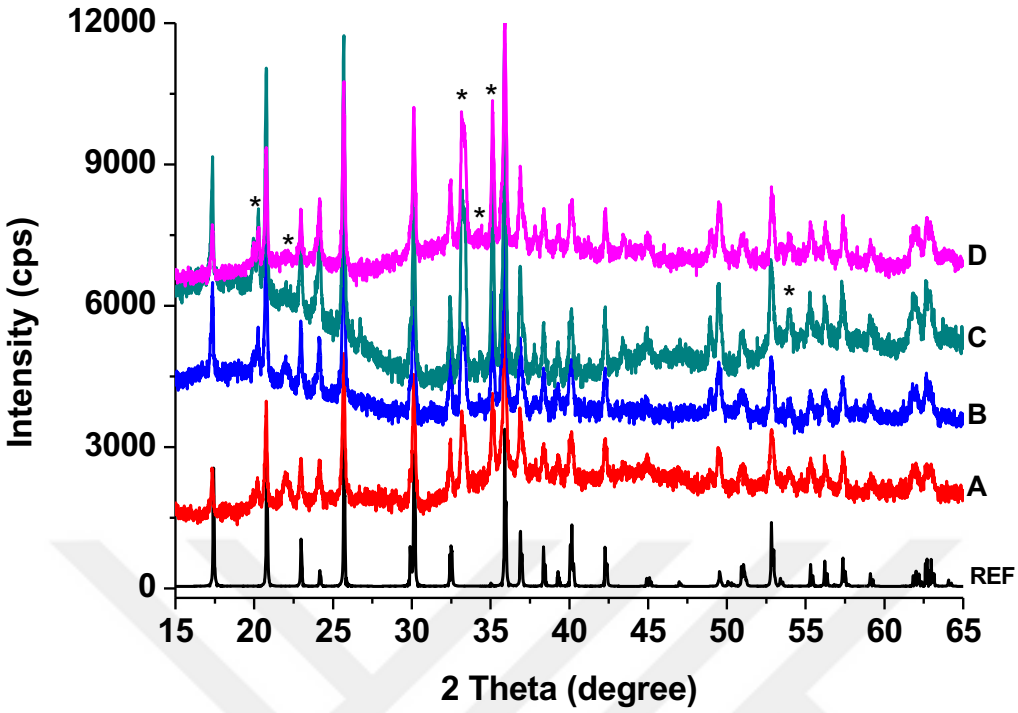

Figure 3.10.3 The XRD patterns of the 6:1 mole ratio Co(II) samples, calcined at 450°C for different durations. The black patterns are from ICDD data base (PDF Card No. 00-032-0552).

mode is observed at 471 cm^{-1}. Very much like the FT-IR studies conducted before, the asymmetric bending and stretching peaks are dominating the spectra of the samples. Moreover, the symmetric stretching modes, at 945 and 1001 cm^{-1} and symmetric bending mode at 471 cm^{-1} emerge at the 450°C. The water peaks around 3400 cm^{-1} can be the adsorbed water after cooling the samples. The peaks around 2800-3000 cm^{-1} are due to unburned surfactant molecules, indicating that there are carbon species in the samples as contamination at lower calcination temperatures. There is a trade-off between the surface area and the remaining carbon species. With the increased temperature, carbon species originating from the surfactant burn out from the samples. However, increased temperature lowers the surface area due to further crystallization and growth of the pore-walls.

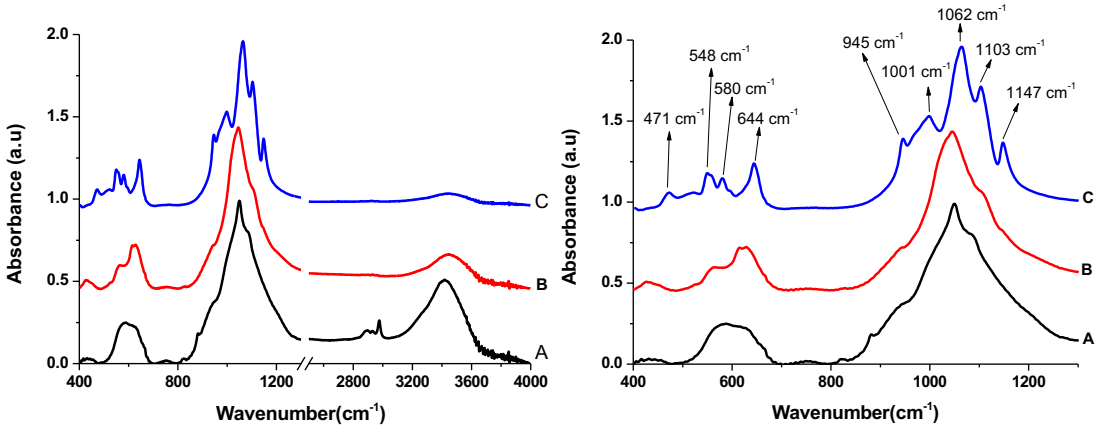

Figure 3.10.4 FTIR spectra of $LiMCoPO_4$, prepared with 6:1 ratio, calcined at different temperatures. (A) 250°C, (B) 350°C, and (C) 450°C.

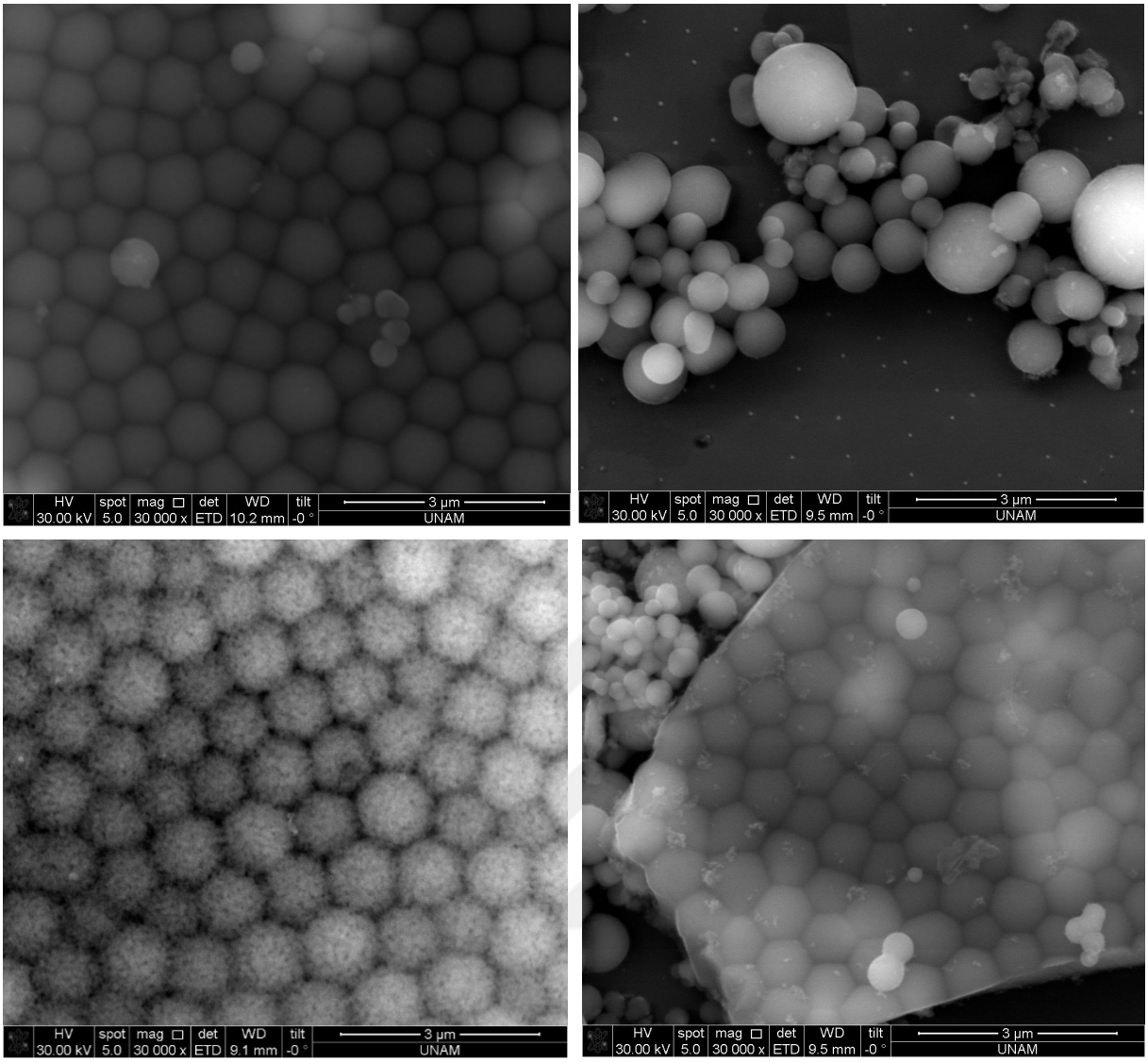

Figure 3.10.5 The SEM images of $LiCoPO_4$ samples, prepared from 6:1 mole ratio and calcined at 250^{o}C. Upper left; sample calcined for 2 hours. Upper right; sample calcined for 4 hours. Lower left; sample calcined for 8 hours. Lower right; sample calcined for 12 hours.

Figures 3.10.5-7 display SEM images of the samples, calcined at three different temperatures. The images clearly show that the particles are spherical and quite uniform in size. With increasing the calcination temperature, the spherical shapes are preserved but the pores become larger. This is also consistent with the observed enhancement of the crystalline phases in the samples.

Morphology of the samples, calcined at 250^{o}C, show that the surfactant could form uniform spherical particles. Increased duration of calcination time does not cause a notable change in the shape of the particles; however, the particles start to crumble and lose their initial smooth surfaced shapes. This continues as time length increases.

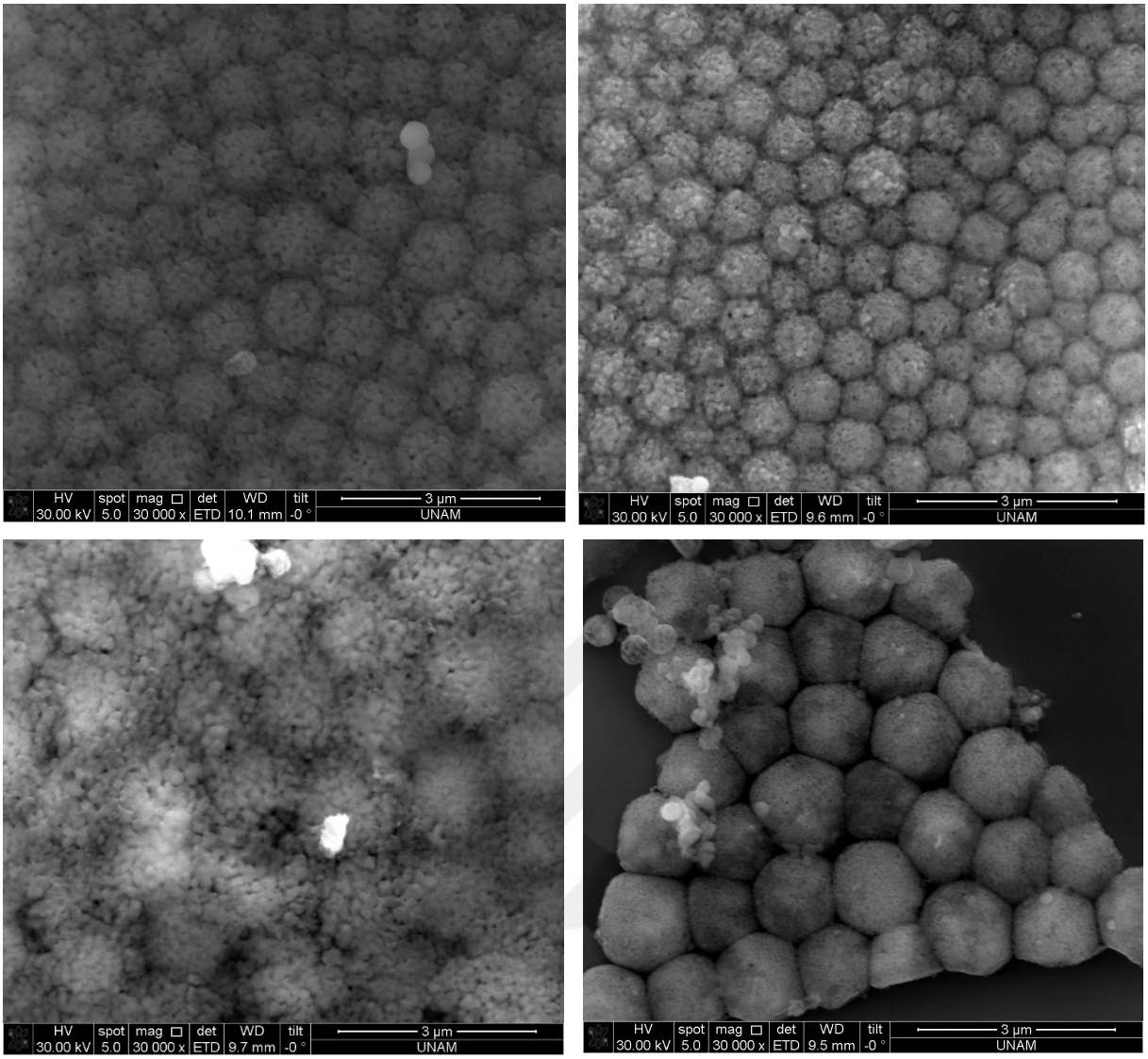

Figure 3.10.6 The SEM images of $LiCoPO_4$ samples, prepared from 6:1 mole ratio and calcined at 350^{o}C. Upper left; sample calcined for 2 hours. Upper right; sample calcined for 4 hours. Lower left; sample calcined for 8 hours. Lower right; sample calcined for 12 hours.

There is a thin film of an unknown origin on top of the particles in the image of the sample calcined for 12 hours. This film is thin enough for electrons to go through it to observe the particles under. Samples calcined at 350^{o}C, also display a similar thermal behaviour apart from particles being crumbled even after 2 hours of calcination. The structure appears almost melted. The empty space inside and around the particles are quite visible and these empty spaces expand with the duration of calcination.

Particles calcined at 450^{o}C lose their shape in even more visible manner. These samples initially keep their shapes and have visible pores, which are clearly above the mesoporous pore size range. These structures then crumble further to a point where they no longer have the spherical shape. After calcination for 12 hours at 450^{o}C, the particles are melted down and aggregated to a level that they appear to be smaller, separate structures without any resemblance to their former selves.

The EDX data gathered at 350^{o}C shows that the sample is pure in terms of elemental composition and there is no sodium contamination. Silicon is from the wafer used as substrate to place the sample.

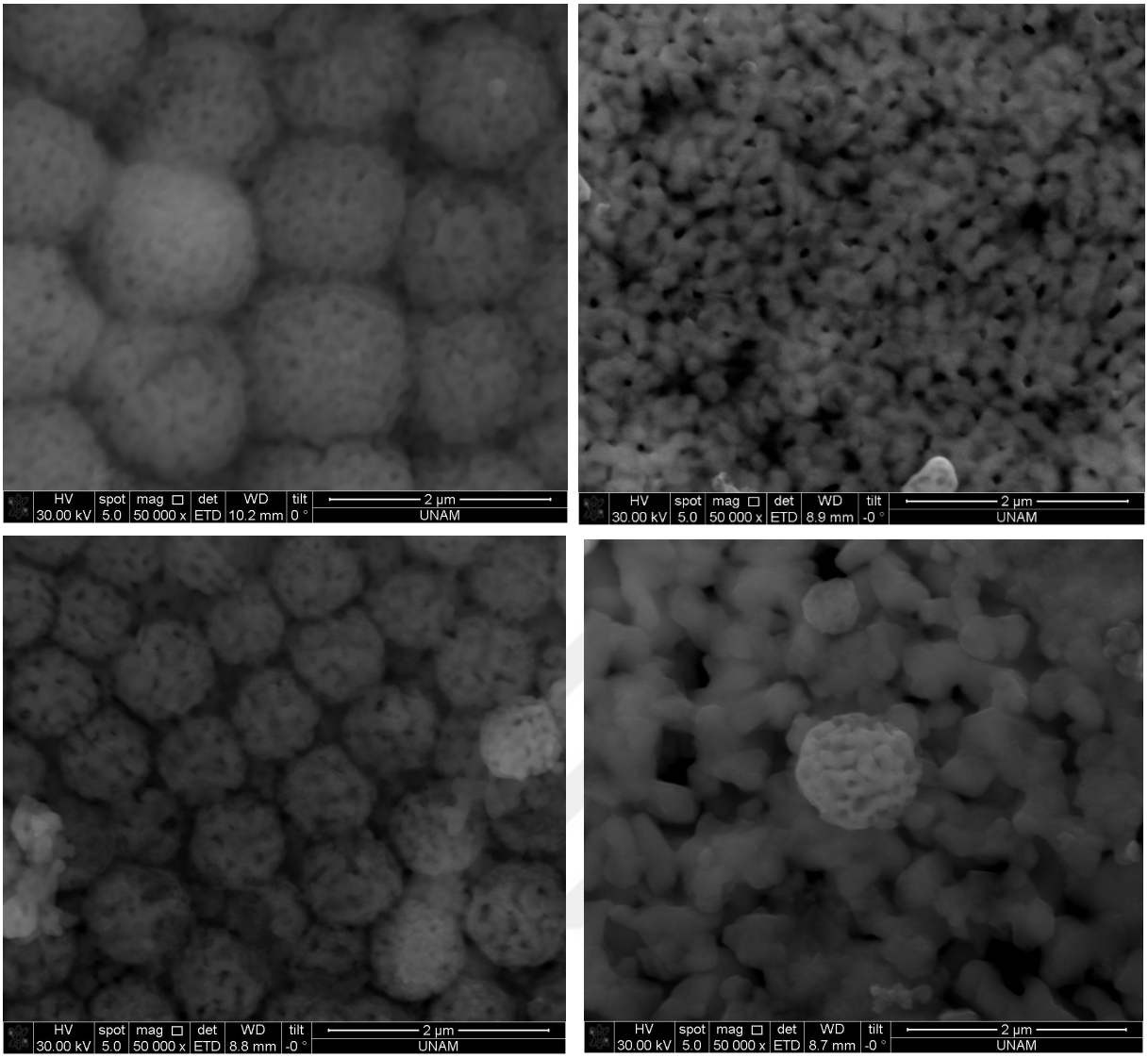

Figure 3.10.7 The SEM images of $LiCoPO_4$ samples, prepared from 6:1 mole ratio and calcined at 450°C. Upper left; sample calcined for 2 hours. Upper right; sample calcined for 4 hours. Lower left; sample calcined for 8 hours. Lower right; sample calcined for 12 hours.

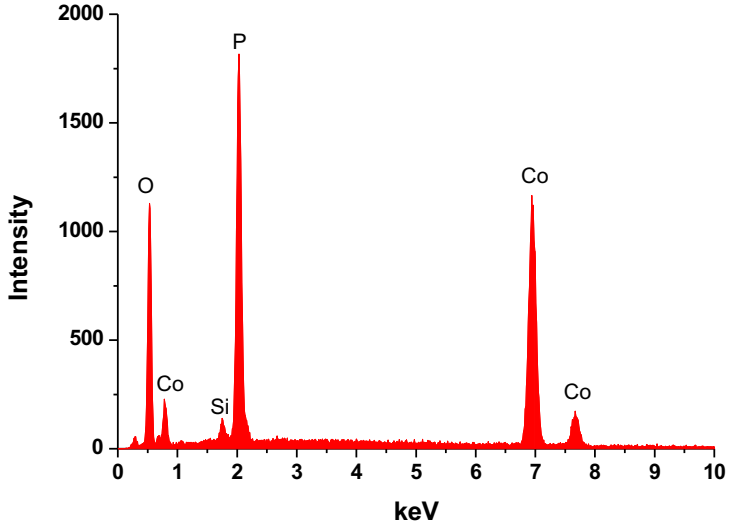

Figure 3.10.8 EDX spectrum of the $LiCoPO_4$ sample calcined at 350°C for 2 hours.

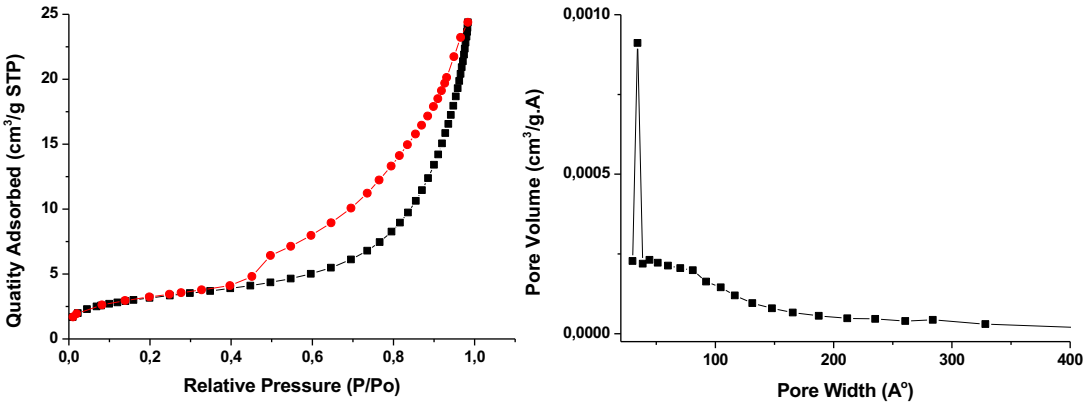

Figure 3.10.9 Linear isotherm plot of $LiCoPO_4$ sample (left) calcined at 250°C for 2 hours and pore size distribution (right).

N_2 adsorption-desorption isotherm display hysteresis characteristic for the porous materials. The hysteria of the $LiCoPO_4$ sample at 250°C, is H3 [23] type and the pore size distribution shows that the pore diameters are non-uniform two type, small and large, peaked at around 3-4 nm and 6-10 nm, see Figure 3.10.9. This sample has a BET surface area of 11 m^2/g. The hysteria, which was also seen in the case of Fe(II) is due to the spherical particles aggregated in a way that they have created holes, which are imitating as pores.

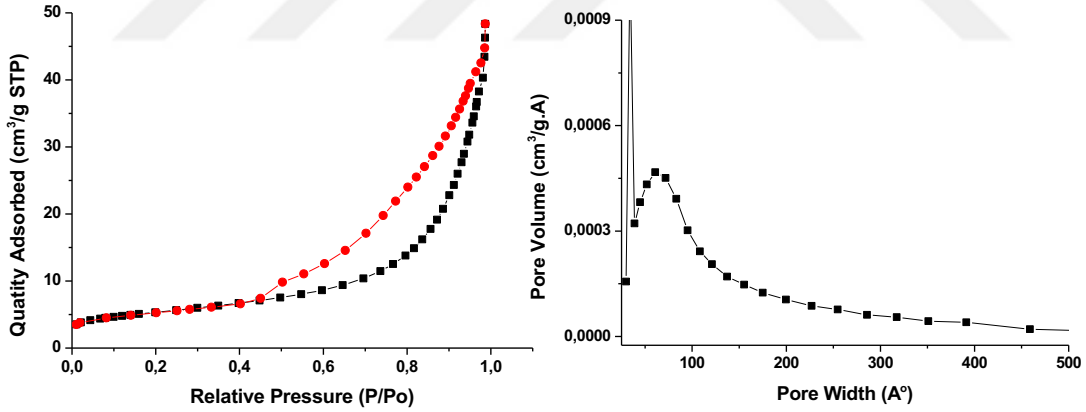

Figure 3.10.10 Linear isotherm plot of $LiCoPO_4$ sample (left) calcined at 350°C for 2 hours and pore size distribution (right).

Sample calcined at 350°C show the similar hysteresis loop, however, with a more converged pore size within the sample, see Figure 3.10.10. The pore size of this sample is around 5-6 nm and it has a surface area of 18 m^2/g. This sample has gained surface area with heat treatment. Overall, pure mesoporous $LiCoPO_4$ was fabricated with a surface area that has reached 18 m^2/g with a pore size of 5-6 nm.

3.11 Mesoporous Lithium Nickel Phosphate

As the last metal, Ni(II) salt has been used to prepare $LiNiPO_4$ using the same method. The conditions for the synthesis was kept the same as the ones used for the Mn(II). The lithium nickel phosphates (LNPs) were synthesised from 6:1 ratio of clear Ni(II) solution upon calcination at 250, 350, and 450^{o}C for 2, 4, 8, and 12 hours' durations to elucidate t he structural details of the samples.

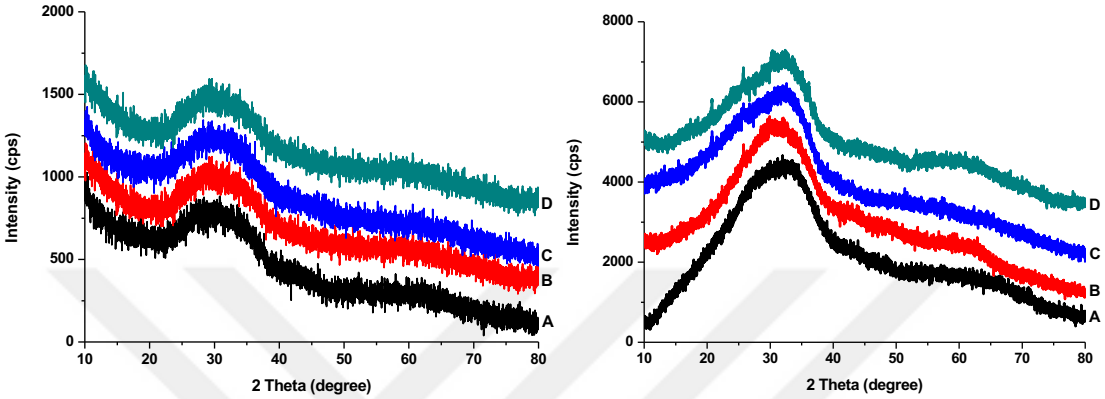

Figure 3.11.1. The XRD patterns of the 6:1 mole ratio Ni(II) samples, calcined at 250 and 350^{o}C for different durations, as marked in the patterns. (A) sample calcined for 2 hours. (B) sample calcined for 4 hours. (C) sample calcined for 8 hours. (D) sample calcined for 12 hours.

The Ni(II) samples, calcined at 250^{o}C is amorphous, see Figures 3.11.1. Samples, calcined at 350^{o}C, however, after a calcination with 12 hours duration four lines emerge at 20.71, 25.73, 30.21, and 36.19 ^{o}, 2θ. The rest of the sample is still amorphous. The patterns of the samples, calcined at 450^{o}C, clearly show that there is an unidentified by-product with a high yield, compared to $LiNiPO_4$ phase, see Figure 3.11.2.

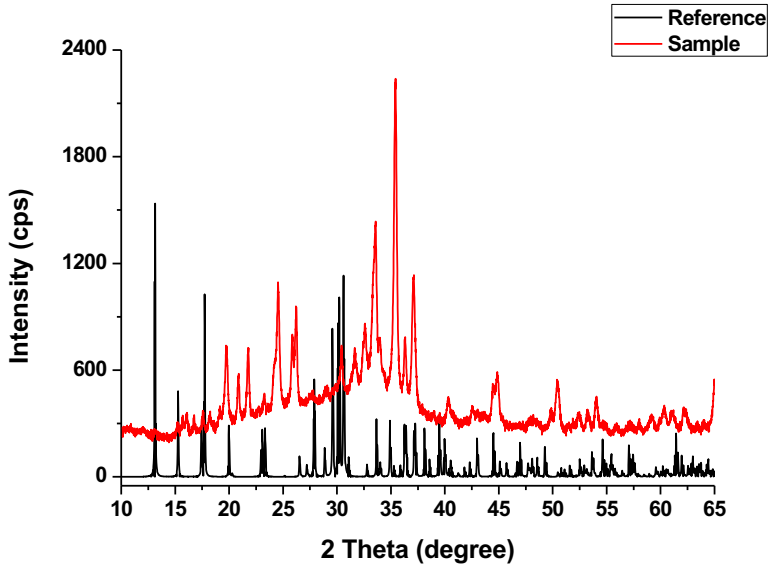

Figure 3.11.2 XRD pattern of nickel sample calcined at 450^{o}C for 12 hours compared with $Li_2Ni_3(P_2O_7)_2$. (PDF Card No: 04-011-4128).

The impurity present was compared to the both phosphate and pyrophosphate references, see Figure 3.11.2-3. It was thought that the difference in time required for the reaction of Ni(II), compared to Mn(II) and Fe(II), with the phosphate ion it was possible that the phosphate could form pyrophosphate and react with the transition metal afterwards. This was not the case for this sample and the impurity remains unidentified.

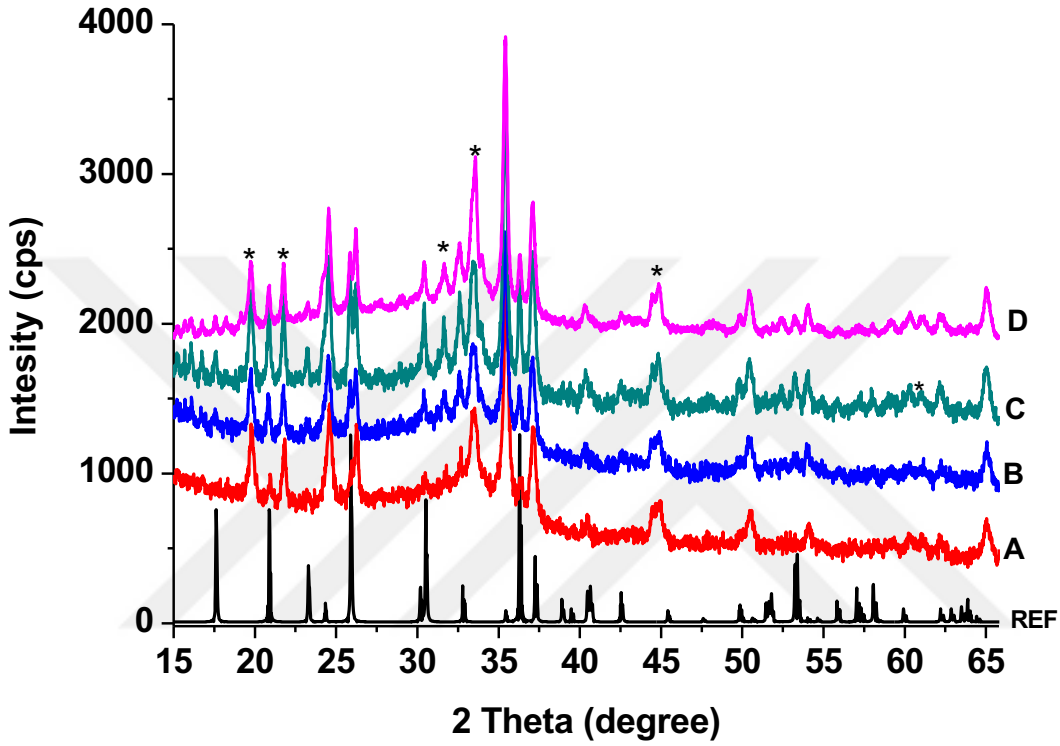

Figure 3.11.3 The XRD patterns of the 6:1 mole ratio Ni(II) samples, calcined at 350oC and 450oC for different durations, as marked on the patterns. (A) sample calcined for 2 hours. (B) sample calcined for 4 hours. (C) sample calcined for 8 hours. (D) sample calcined for 12 hours. Reference is of LiNiPO4. (PDF Card No: 00-032-0578)

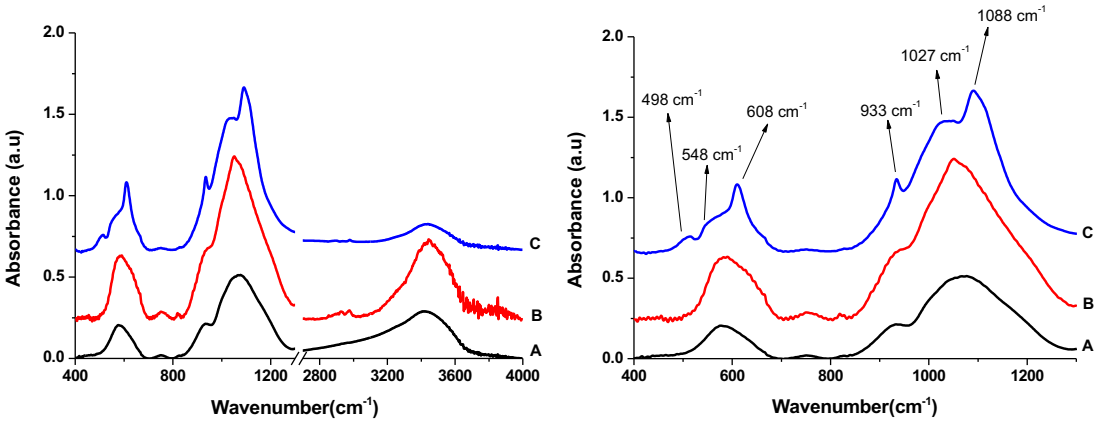

Figure 3.11.3 FTIR spectra of $LiNiPO_4$, prepared with 6:1 ratio, calcined at different temperatures. (A) 250°C, (B) 350°C, and (C) 450°C.

We also collected the FT-IR spectra of the samples, calcined at three different temperatures. As the calcination temperature goes up, both stretching and bending modes of phosphate get more pronounced and the symmetric modes for both stretching and bending modes emerge at 450^{o}C, see Figure 3.11.3. The surfactant peaks disappear after calcination even at 250^{o}C. Water peak intensities relative to the phosphate is significantly reduced at 450^{o}C. If we assume high intensity of water is due to high surface area in the samples the surface area is reduced at 450^{o}C. This states a single statement, which was already made for other samples, these samples are significantly porous and there is a good chance that they are not clogged. One thing that grabs attention is the sample diffraction lines in XRD patterns are quite sharp, indicating well-crystallization, but FT-IR absorption spectra do not seem to be indicating a crystalline material. This contradiction may be showing the presence of more than one phase in the samples at 450^{o}C. Further investigations are required to fully characterize the samples.

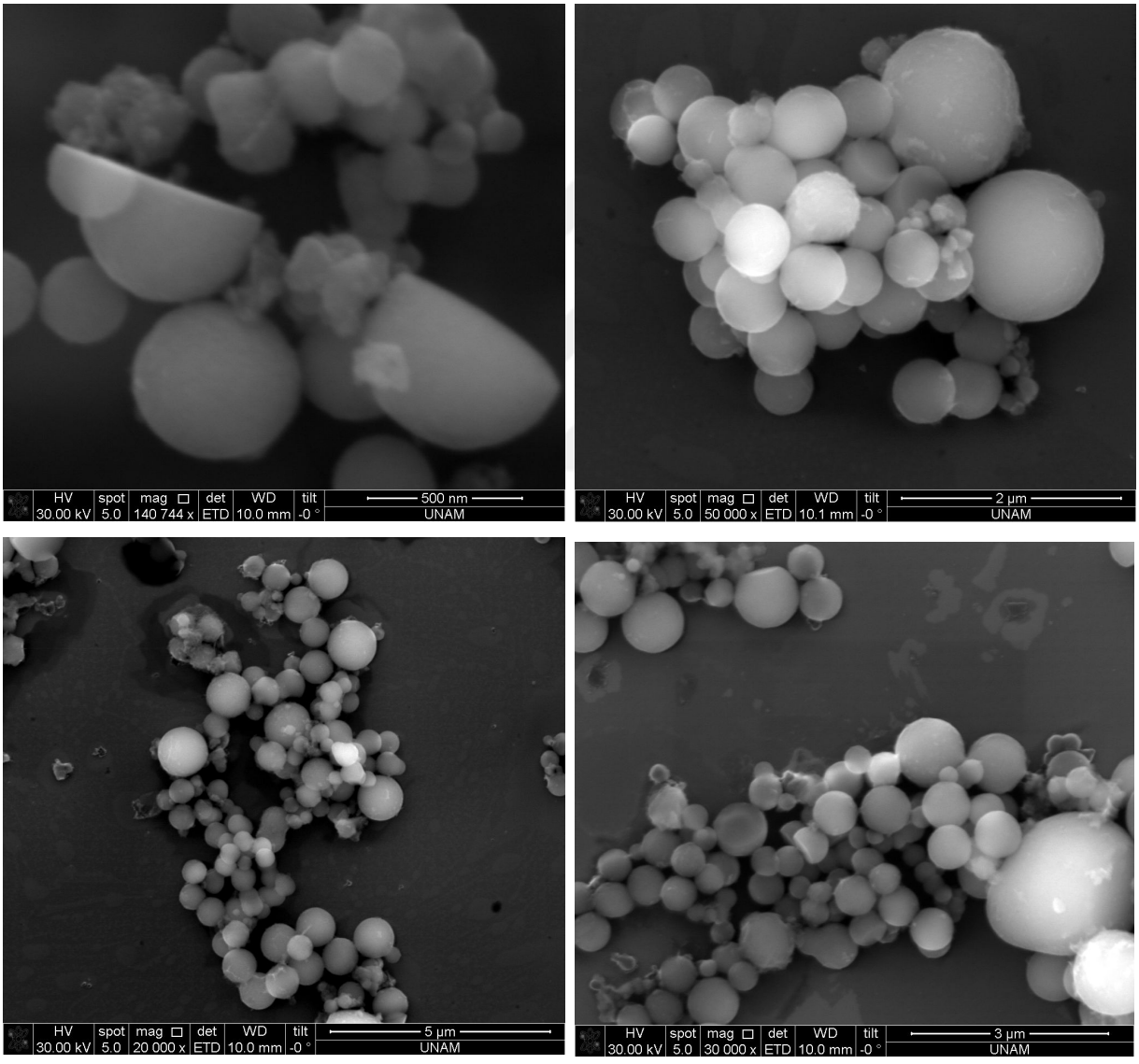

Figure 3.11.4 The SEM images of $LiNiPO_4$ samples, prepared from 6:1 mole ratio and calcined at 250^{o}C. Upper left; sample calcined for 2 hours. Upper right; sample calcined for 4 hours. Lower left; sample calcined for 8 hours. Lower right; sample calcined for 12 hours.

The SEM images show that the samples are spherical and the distribution of these particles are variant in size, Figure 3.11.4. Morphology of the sample is homogeneous and it does not change with increasing calcination duration. The particle sizes range from 100 nm to 1 μm. Notice also that there are also smaller particles over the large ones, indicating the presence of a second phase. These smaller particles emerge with heating the samples to 350^{o}C, see Figure 3.11.5. The images do not show any porosity at these two calcination temperatures. However, the samples, calcined at 450^{o}C show porous features over the spherical particles.

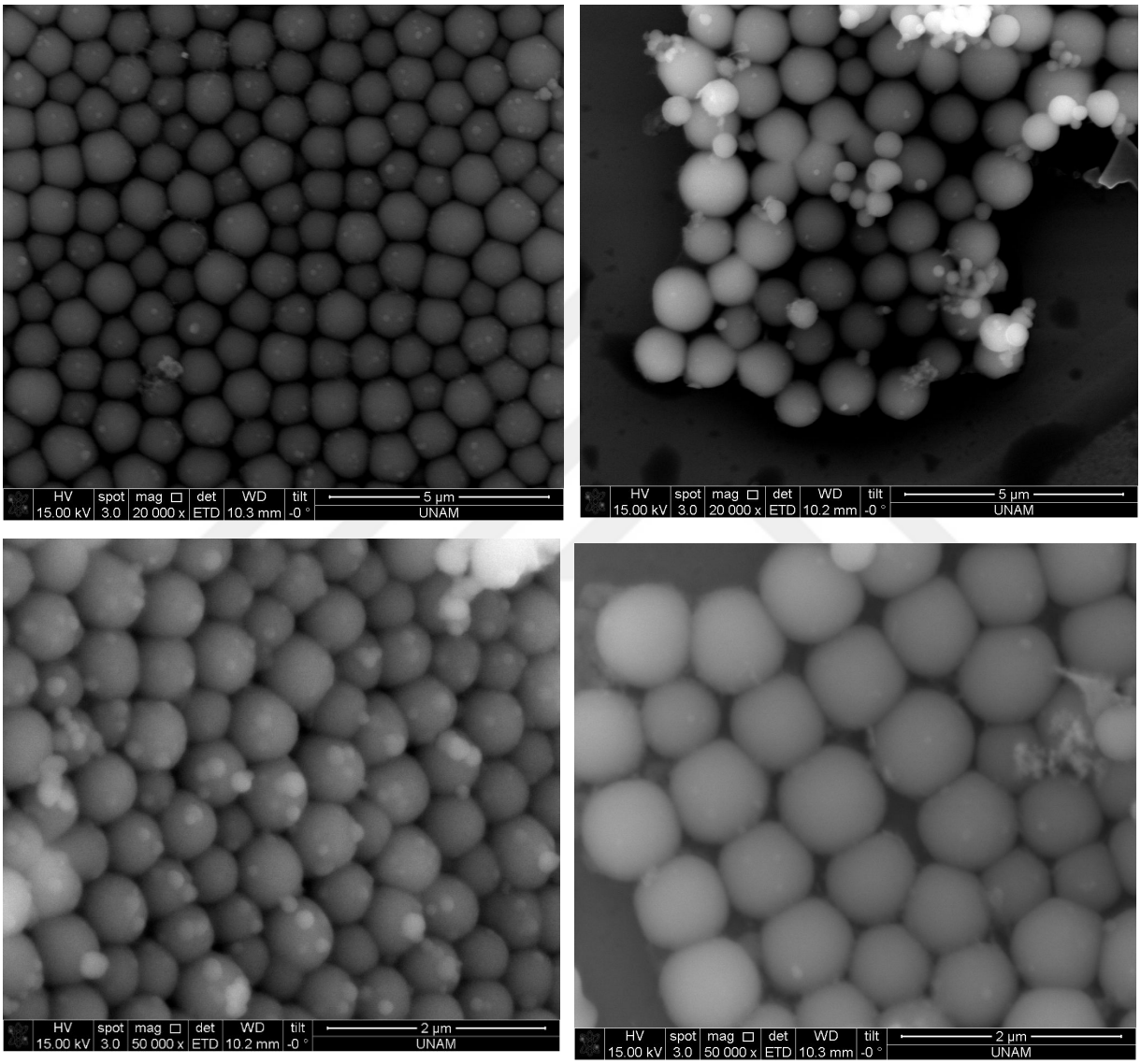

Figure 3.11.5 The SEM images of $LiNiPO_4$ samples, prepared from 6:1 mole ratio and calcined at 350^{o}C. Upper left; sample calcined for 2 hours. Upper right; sample calcined for 4 hours. Lower left; sample calcined for 8 hours. Lower right; sample calcined for 12 hours.

The samples, calcined at 450^{o}C show a remarkable change with increasing calcination duration, see Figure 3.11.6. During this annealing process, walls of the pores get wider and larger, as walls get thicker pores crumble and surface area diminishes.

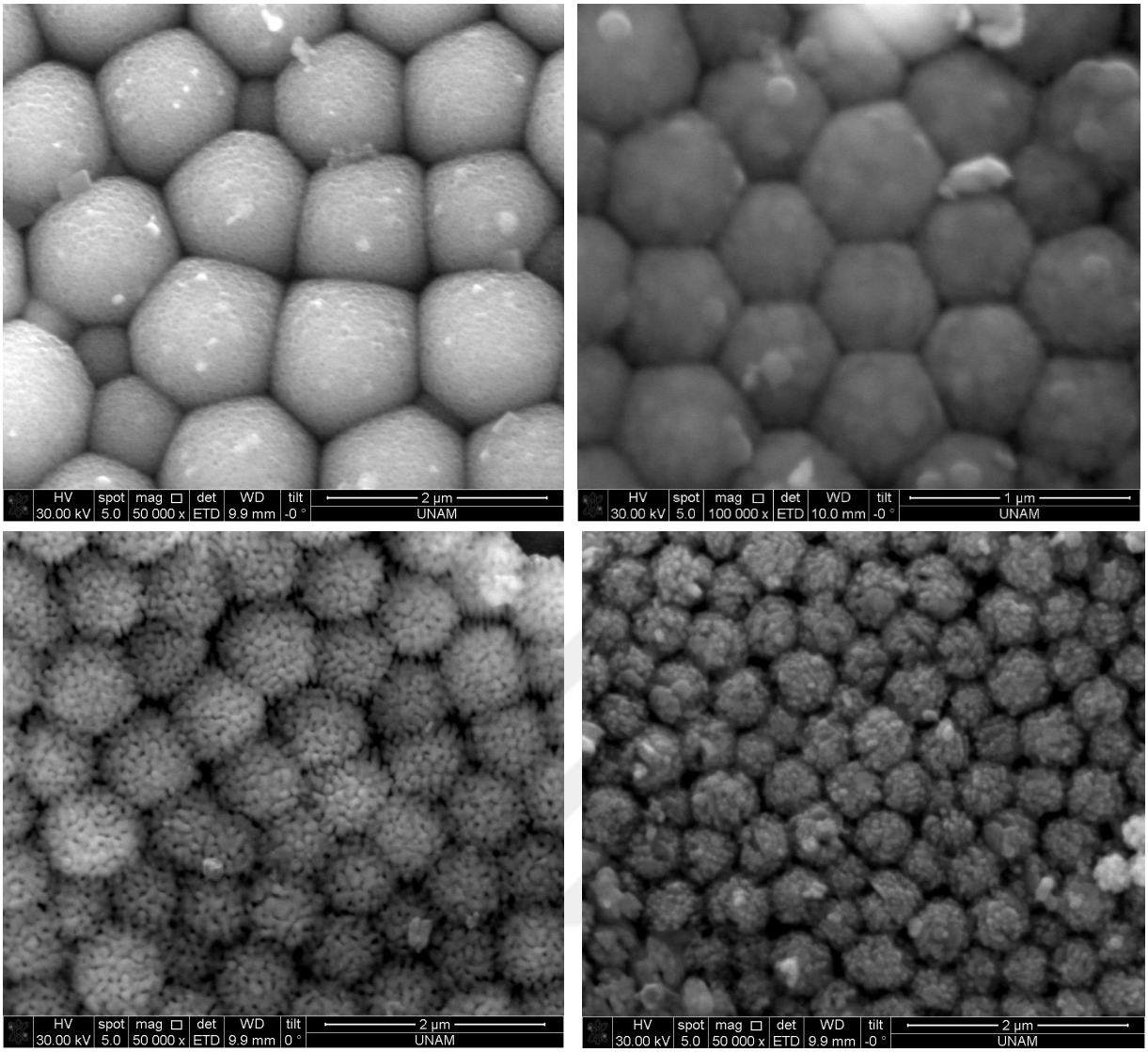

Figure 3.11.6 The SEM images of $LiNiPO_4$ samples, prepared from 6:1 mole ratio and calcined at 450°C. Upper left; sample calcined for 2 hours. Upper right; sample calcined for 4 hours. Lower left; sample calcined for 8 hours. Lower right; sample calcined for 12 hours.

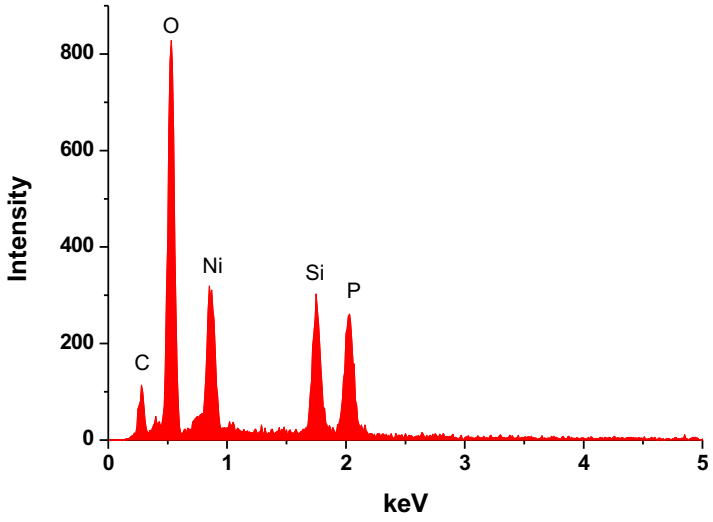

Figure 3.11.7 EDAX data gathered from the $LiNiPO_4$ sample calcined at 350°C for 2 hours.

The pores collapse on each other forming larger pores with thicker walls to the point that there is an empty space between walls. Since the diffraction lines of these samples are quite different than targeted $LiNiPO_4$ further studies are required to identify the product and possible transformation mechanism during annealing the samples.

EDX shows that the sample is pure nickel phosphate. The silicon signal comes from the wafer, which was used as substrate.

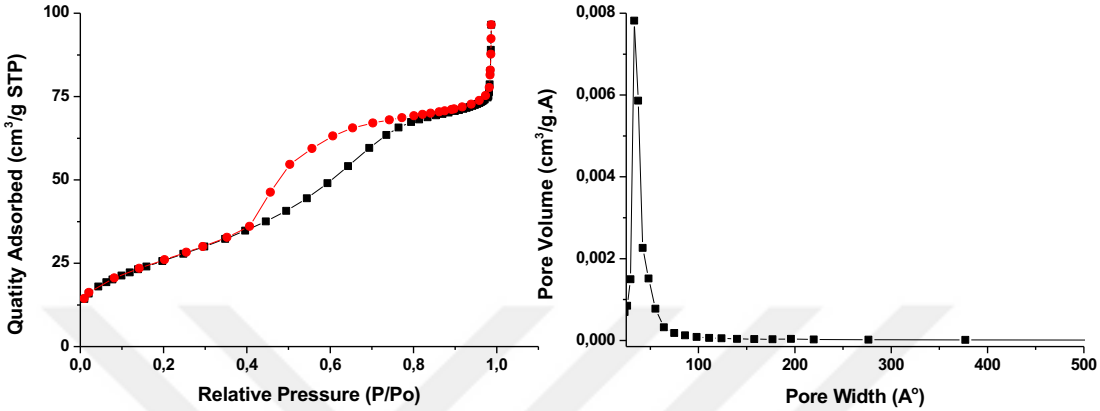

Figure 3.11.8 Linear isotherm plot of $LiNiPO_4$ sample (left) calcined at 250°C for 2 hours and pore size distribution (right).

N_2 adsorption-desorption isotherm displays a typical type IV branch, typical for mesoporous materials. The hysteria loop type of the sample calcined at 250°C is H2 [23]. This type occurs because of the narrow openings of pores with uniform channels, connected to each other. This sample has small and narrow pore diameter compared to previous samples, around 3 nm and it has a surface area of 95 m^2/g. Connectivity of pores inside the particles cannot be confirmed by SEM imaging, but there are visible pores on the surface of the spheres.

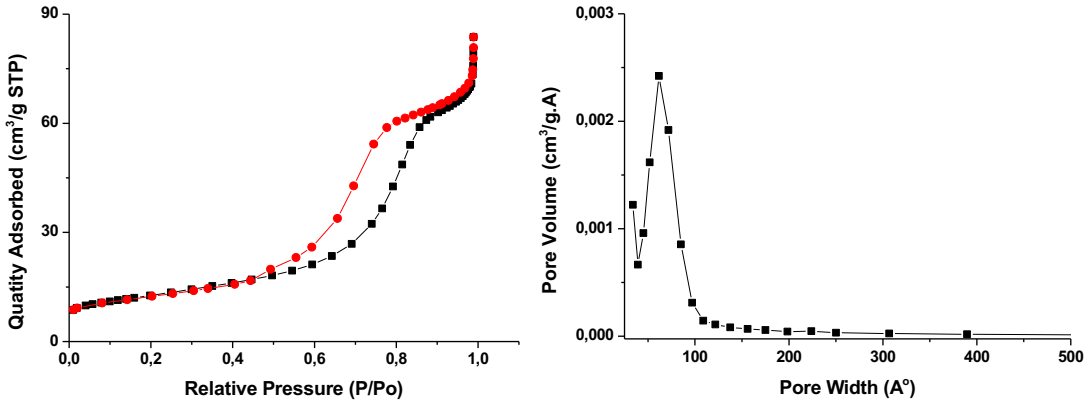

Figure 3.11.9 Linear isotherm plot of $LiNiPO_4$ sample (left) calcined at 350°C for 2 hours and pore size distribution (right).

Sample calcined at 350°C display a type IV isotherm. The pores size distribution shows the pore diameter increased from 3 to 6-7 nm at 350°C. Also,surface area dropped from 95 to 44 m^2/g. The LNP sample has an undefined structure. However, the nickel samples are mesoporous with a uniform pore distribution and high surface area compared all previous samples.

CHAPTER 4

4 CONCLUSION

This study encompasses the synthesis and characterization of mesoporous $LiMPO_4$ (M= Mn(II), Fe(II), Co(II), Ni(II)) by using a modified MASA approach using 10-lauryl ether as structure directing surfactant. These minerals are to be used as cathode materials for lithium ion batteries. This method employs LLC mesophases to form mesoporous materials. The process starts as a clear solution of salts (lithium nitrate and transition metal nitrate), phosphoric acid, surfactant ($C_{12}EO_{10}$) and a volatile solvent (water). The clear solution can be spin or drop-cast coated over a substrate for further treatments. All ten solutions (ranging from 1:1 to 10:1), prepared to test the resilience of the solutions in terms of time and pH and mesophase stability over time, form stable mesophases. The Mn(II) and Fe (II) solutions have shown to be unstable at high concentration overtime. On the other hand, Co(II) and Ni(II) solutions, even at high concentrations, have been extremely stable. It was found that the pH affects the stability and it is inversely proportional to the solution concentration. At high concentrations, the system was able to handle the evaporation of water by keeping the mesophase, however, low concentrations lost their ordered mesophases. The investigation was further carried using 3 ratios, 3:1, 6:1, 9:1 selected to represent low, mid, and high concentrations. These mesophases display x-ray diffractions at small angles and time and temperature dependent changes that can be monitored by using x-ray diffractometer. The mesophase is destroyed at elevated temperatures but stable at low temperatures for a long time. Water and nitrate species are mostly lost at relatively low temperatures, but surfactant started burn around 160^oC. Each of these species tend to disappear around 230-250^oC. The drop-cast method is more applicable to obtain the desired $LiMnPO_4$ product at large quantities, however spin coating formed a completely different material; those samples need to be further characterized. Optimization studies showed that 6:1 ratio is best for the synthesis. Materials appeared to be mesoporous and the morphology of samples found to be metal cation and temperature dependent. $LiMnPO_4$ formed spherical particles with pinkish colour and it was crystallized at 350^oC with little impurity, and it crystallized with shallow pores at 250^oC and the pore structure remained even after heating up to 350^oC, with a heterogeneous pore size distribution. $LiMnPO_4$ has around 13 m^2/g surface area. $LiFePO_4$ formed red coloured, thread like particles, which have aggregated into spheres at 250^oC, then formed film like structures at 350^oC and 450^oC. $LiFePO_4$ crystallized after annealing at 450^oC with some undefined impurity phase. The mesoporous $LiFePO_4$ displays slit like pores with a heterogeneous pore size distribution and a BET surface are of 56 m^2/g at 250^oC. A more uniformed pore size distribution, gathered around 6-7 nm with a BET surface are of 53 m^2/g, is observed at 350^oC. Mesoporous $LiCoPO_4$ was synthesised with little impurity, it is blue coloured, and it crystallize at 350^oC. It had formed shallow cylindrical pores with a heterogeneous pore distribution at 250^oC, which then gathered around 6-7 nm at 350^oC. The surface area at 250^oC is 11 m^2/g and 18 m^2/g at 350^oC. Mesoporous lithium nickel phosphate, coloured yellow, is synthesised with an undefined phase. The new phase is fully crystalline at 450^oC. The nickel sample provided small and uniform pores, around 3-4 nm at 250^oC and 6-7 nm at 350^oC. The surface area of the nickel samples is the largest among all lithium metal phosphates, investigated in this thesis, with a BET surface area of 96 m^2/g at 250^oC and 44 m^2/g at 350^oC. Overall, it has been shown that the MASA approach in the presence of weak acid is a useful and effortless method to synthesise mesoporous lithium metal phosphate materials.

Bibliography

[1] P. G. d. Gennes, *The physics of liquid crystals*. 1993.

[2] S. Chandrasekhar, *Liquid Crystals*. 1992.

[3] J. H. R. Dong, "Complex Fluids of Poly(oxyethylene) Monoalkyl Ether Nonionic Surfactants," *Chem. Rev.*, vol. 9, no. 110, pp. 4978–5022, 2010.

[4] C. Seguin, J. Eastoe, R. Clapperton, R. K. Heenan, and I. Grillo, "Alternative non-aqueous water-miscible solvents for surfactants," *Colloids Surfaces A*, vol. 283, pp. 134–142, 2006.

[5] M. U. Araos and G. G. Warr, "Self-Assembly of Nonionic Surfactants into Lyotropic Liquid Crystals in Ethylammonium Nitrate , a Room-Temperature Ionic Liquid," *J. pd Phys. Chem. B*, vol. 109, no. 30, pp. 14275–14277, 2005.

[6] Ö. Celik and O. Dag, "A new lyotropic liquid-crystalline phase is formed from oligo- (ethylene oxide) surfactants and M(H 2 O)," *Angew. Chem.*, vol. 40, no. 20, pp. 3799–3803, 2001.

[7] F. M. Balci, S. Balci, C. Kocabas, and O. Dag, "Lyotropic Liquid-Crystalline Mesophase of Lithium Triflate−Nonionic," *J. pd Phys. Chem. C*, vol. 121, no. 21, pp. 11194–11200, 2017.

[8] G. G. Warr and M. U. Araos, "Self-Assembly of Nonionic Surfactants into Lyotropic Liquid Crystals in Ethylammonium Nitrate, a Room-Temperature Ionic Liquid," *J. Phys. Chem B*, vol. 30, no. 109, pp. 14275–14277, 2005.

[9] J. S. Beck, K. D. Schmitt, J. B. Higgins, and J. L. Schlenkert, "New Family of Mesoporous Molecular Sieves Prepared with Liquid Crystal Templates," *J. Am. Chem. Soc.*, vol. 114, pp. 10834–10843, 1992.

[10] G. S. Attard, C. Glyde, and C. G. Göltner, "Liquid cryatalline phases as templates for the synthesis of mesoporous silica," *Nature*, vol. 378, pp. 366–368, 1995.

[11] B. E. Eser, A. F. Demirors, and O. Dag, "Liquid Crystalline Mesophases of Pluronics (L64 , P65 , and P123) and Transition Metal Nitrate Salts ([M (H 2 O) 6](NO 3) 2)," *Langmuir*, vol. 21, no. 3, pp. 4156–4162, 2005.

[12] S. Leyva-García, D. Lozano-Castelló, E. Morallón, and D. Cazorla-Amorós, "Silica-templated ordered mesoporous carbon thin films as electrodes for micro-capacitors," *J. Mater. Chem. A*, vol. 4, no. 12, pp. 4570–4579, 2016.

[13] C. Albayrak, N. Özkan, and O. Dag, "Origin of Lyotropic Liquid Crystalline Mesophase

Formation and Liquid Crystalline to Mesostructured Solid Transformation in the Metal Nitrate Salt−Surfactant Systems MASA.pdf," *Langmuir*, vol. 27, no. 3, 2010.

[14] C. Karakaya, Y. Türker, C. Albayrak, and Ö. Dag, "Assembly of molten transition metal salt-surfactant in a confined space for the synthesis of mesoporous metal oxide-rich metal oxide-silica thin films," *Chem. Mater.*, vol. 23, no. 12, pp. 3062–3071, 2011.

[15] Y.-F. Lee, K.-H. Chang, C.-Y. Chu, H.-L. Chen, and C.-C. Hu, "Microstructure tuning of mesoporous silica prepared by evaporation-induced self-assembly processes: interactions among solvent evaporation, micelle formation/packing and sol condensation," *RSC Adv.*, vol. 1, no. 3, p. 401, 2011.

[16] T. Brezesinski, M. Groenewolt, A. Gibaud, N. Pinna, M. Antonietti, and B. M. Smarsly, "Evaporation-induced self-assembly (EISA) at its limit: Ultrathin, crystalline patterns by templating of micellar monolayers," *Adv. Mater.*, vol. 18, no. 17, pp. 2260–2263, 2006.

[17] C. J. Brinker, Y. F. Lu, A. Sellinger, and H. Y. Fan, "Evaporation Induced Self-Assembly: Nanostructures Made Easy," *Adv. Mater.*, vol. 11, no. 7, pp. 579–585, 1999.

[18] N. S. Norberg and R. Kostecki, "FTIR spectroscopy of a LiMnPO4 composite cathode," *Electrochim. Acta*, vol. 56, no. 25, pp. 9168–9171, 2011.

[19] C. Karakaya, Y. Türker, and Ö. Dag, "Molten-Salt-Assisted Self-Assembly (MASA) -Synthesis of Mesoporous Metal Titanate-Titania , Metal Sulfi de-Titania , and Metal Selenide-Titania Thin Films," *Adv. Funct. Mater.*, vol. 23, pp. 4002–4010, 2013.

[20] C. Karakaya, T. Yurdanur, C. Albayrak, and O. Dag, "Assembly of Molten Transition Metal Salt À Surfactant in a Confined Space for the Synthesis of Mesoporous Metal Oxide-Rich Metal Oxide À Silica Thin Films," *Chem. Mater.*, vol. 23, pp. 3062–3071, 2011.

[21] C. Avc *et al.*, "Molten Salt Assisted Self Assembly (MASA): Synthesis of Mesoporous Metal Titanate (CoTiO3, MnTiO3, and Li4Ti5O12) Thin Films and Monoliths," *Chem. Mater.*, vol. 26, pp. 6050–6057, 2014.

[22] Z. Zhang, F. Zuo, and P. Feng, "Hard template synthesis of crystalline mesoporous anatase TiO2 for photocatalytic hydrogen evolution," *J. Mater. Chem.*, vol. 20, no. 11, p. 2206, 2010.

[23] M. Tiemann, "Porous metal oxides as gas sensors," *Chem. - A Eur. J.*, vol. 13, no. 30, pp. 8376–8388, 2007.

[24] A. Rumplecker, F. Kleitz, E. L. Salabas, and F. Schüth, "Hard templating pathways for the

synthesis of nanostructured porous Co 3O4," *Chem. Mater.*, vol. 19, no. 3, pp. 485–496, 2007.

[25] W. Shen, X. Dong, Y. Zhu, H. Chen, and J. Shi, "Mesoporous CeO2and CuO-loaded mesoporous CeO2: Synthesis, characterization, and CO catalytic oxidation property," *Microporous Mesoporous Mater.*, vol. 85, no. 1–2, pp. 157–162, 2005.

[26] E. Rossinyol *et al.*, "Nanostructured metal oxides synthesized by hard template method for gas sensing applications," *Sensors Actuators, B Chem.*, vol. 109, no. 1, pp. 57–63, 2005.

[27] K. M. Shaju, F. Jiao, A. Débart, and P. G. Bruce, "Mesoporous and nanowire Co_3O_4 as negative electrodes for rechargeable lithium batteries," *Phys. Chem. Chem. Phys.*, vol. 9, no. 15, pp. 1837–1842, 2007.

[28] C. Dickinson, W. Zhou, R. P. Hodgkins, Y. Shi, D. Zhao, and H. He, "Formation mechanism of porous single-crystal Cr2O3 and Co3O4 templated by mesoporous silica," *Chem. Mater.*, vol. 18, no. 13, pp. 3088–3095, 2006.

[29] B. Tian *et al.*, "General Synthesis of Ordered Crystallized Metal Oxide Nanoarrays Replicated by Microwave-Digested Mesoporous Silica," *Adv. Mater.*, vol. 15, no. 16, pp. 1370–1373, 2003.

[30] M. Imperor-clerc, D. Bazin, M. Appay, P. Beaunier, and A. Davidson, "Crystallization of β-MnO2 Nanowires in the Pores of SBA-15 Silicas : In Situ Investigation Using Synchrotron Radiation," *Chem. Mater.*, vol. 16, no. 11, pp. 1813–1821, 2004.

[31] S. Zhu, Z. Zhou, D. Zhang, and H. Wang, "Synthesis of mesoporous amorphous MnO2from SBA-15 via surface modification and ultrasonic waves," *Microporous Mesoporous Mater.*, vol. 95, no. 1–3, pp. 257–264, 2006.

[32] T. Brezesinski, M. Groenewolt, M. Antonietti, and B. Smarsly, "Crystal-to-crystal phase transition in self-assembled mesoporous iron oxide films," *Angew. Chemie - Int. Ed.*, vol. 45, no. 5, pp. 781–784, 2006.

[33] D. Grosso, C. Boissière, L. Nicole, and C. Sanchez, "Preparation, treatment and characterisation of nanocrystalline mesoporous ordered layers," *J. Sol-Gel Sci. Technol.*, vol. 40, no. 2–3, pp. 141–154, 2006.

[34] C. J. Brinker, A. J. Hurd, G. C. Frye, K. J. Ward, and C. S. Ashley, "Sol-gel thin film formation," *J. Non. Cryst. Solids*, vol. 121, no. 1–3, pp. 294–302, May 1990.

[35] M. Takagi, "Electron-Diffraction Study of Liquid-Solid Transition of Thin Metal Films," *J. Phys.*

Soc. Japan, vol. 9, no. 3, pp. 359–363, 1954.

[36] G. L. Allen, R. A. Bayles, W. W. Gile, and W. A. Jesser, "Small Particle Melting of Pure Metals," *Thin Solid Filmsİlms*, vol. 144, pp. 297–308, 1986.

[37] S. K. Gupta, M. Talati, and P. K. Jha, "Shape and Size Dependent Melting Point Temperature of Nanoparticles," *Mater. Sci. Forum*, vol. 570, no. January, pp. 132–137, 2008.

[38] A. K. Padhi, K. S. Nanjundaswamy, and J. B. Goodenough, "Phospho-olivines as Positive-Electrode Materials for Rechargeable Lithium Batteries," *J. Electrochem. Soc.*, vol. 144, no. 4, pp. 1188–1194, 1997.

[39] E. Stura and C. Nicolini, "New nanomaterials for light weight lithium batteries," *Anal. Chim. Acta*, vol. 568, no. 1–2, pp. 57–64, 2006.

[40] S. Okada *et al.*, "Cathode properties of phospho-olivine LiMPO4 for lithium secondary batteries," *J. Power Sources*, vol. 97–98, pp. 430–432, 2001.

[41] J. L. Tirado, "Inorganic materials for the negative electrode of lithium-ion batteries: State-of-the-art and future prospects," *Mater. Sci. Eng. R Reports*, vol. 40, no. 3, pp. 103–136, 2003.

[42] K. Rissouli, K. Benkhouja, J. R. Ramos-barrado, and C. Julien, "Electrical conductivity in lithium orthophosphates," *Mater. Sci. Eng. B*, vol. 98, pp. 185–189, 2003.

[43] M. Piana, B. L. Cushing, J. B. Goodenough, and N. Penazzi, "A new promising sol-gel synthesis of phospho-olivines as environmentally friendly cathode materials for Li-ion cells," *Solid State Ionics*, vol. 175, no. 1–4, pp. 233–237, 2004.

[44] F. Zhou, K. Kang, T. Maxisch, G. Ceder, and D. Morgan, "The electronic structure and band gap of LiFePO4and LiMnPO4," *Solid State Commun.*, vol. 132, no. 3–4, pp. 181–186, 2004.

[45] J. M. Osorio-Guillén, B. Holm, R. Ahuja, and B. Johansson, "A theoretical study of olivine LiMPO4cathodes," *Solid State Ionics*, vol. 167, no. 3–4, pp. 221–227, 2004.

[46] J. Wolfenstine and J. Allen, "LiNiPO4-LiCoPO4 solid solutions as cathodes," *J. Power Sources*, vol. 136, no. 1, pp. 150–153, 2004.

[47] N. Penazzi, M. Arrabito, M. Piana, S. Bodoardo, S. Panero, and I. Amadei, "Mixed lithium phosphates as cathode materials for Li-Ion cells," *J. Eur. Ceram. Soc.*, vol. 24, no. 6, pp. 1381–1384, 2004.

[48] D. Wang, Z. Wang, X. Huang, and L. Chen, "Continuous solid solutions LiFe1−xCoxPO4 and its

electrochemical performance," *J. Power Sources*, vol. 146, pp. 580–583, 2005.

[49] T. Nakamura *et al.*, "Electrochemical study on Mn2+-substitution in LiFePO4olivine compound," *J. Power Sources*, vol. 174, no. 2, pp. 435–441, 2007.

[50] C. Delacourt, P. Poizot, M. Morcrette, J. M. Tarascon, and C. Masquelier, "One-Step Low-Temperature Route for the Preparation of Electrochemically Active LiMnPO4 Powders," *Chem. Mater.*, vol. 16, no. 1, pp. 93–99, 2004.

[51] J. Chen, S. Wang, and M. S. Whittingham, "Hydrothermal synthesis of cathode materials," *J. Power Sources*, vol. 174, no. 2, pp. 442–448, 2007.

[52] T. R. Kim *et al.*, "Synthesis of lithium manganese phosphate nanoparticle and its properties," *J. Phys. Chem. Solids*, vol. 68, no. 5–6, pp. 1203–1206, 2007.

[53] C. M. Julien, A. Ait Salah, F. Gendron, J. F. Morhange, A. Mauger, and C. V. Ramana, "Microstructure of LiXPO4(X = Ni, Co, Mn) prepared by solid state chemical reaction," *Scr. Mater.*, vol. 55, no. 12, pp. 1179–1182, 2006.

[54] T. J. Richardson, "Phosphate-stabilized lithium intercalation compounds," *J. Power Sources*, vol. 119–121, pp. 262–265, 2003.

[55] R. Dominko *et al.*, "Porous olivine composites synthesized by sol-gel technique," *J. Power Sources*, vol. 153, no. 2, pp. 274–280, 2006.

[56] M. Manickam, P. Singh, S. Thurgate, and K. Prince, "Redox behavior and surface characterization of LiFePO4 in lithium hydroxide electrolyte," *J. Power Sources*, vol. 158, no. 1, pp. 646–649, 2006.

[57] S. Okada *et al.*, "Cathode properties of phospho-olivine LiMPO4 for lithium secondary batteries," *J. Power Sources*, vol. 97, no. 8, pp. 430–432, 2001.

[58] K. Amine, H. Yasuda, and M. Yamachi, "Olivine LiCoPO4 as 4.8 V Electrode Material for Lithium Batteries," *Electrochem. Solid State Lett.*, vol. 3, no. 4, pp. 178–179, 2000.

[59] G. Li, H. Azuma, and M. Tohda, "LiMnPO4 as the Cathode for Lithium Batteries," *Electrochem. Solid State Lett.*, vol. 5, no. 6, pp. A135–A137, 2002.

[60] T. Drezen, N. H. Kwon, P. Bowen, I. Teerlinck, M. Isono, and I. Exnar, "Effect of particle size on LiMnPO4cathodes," *J. Power Sources*, vol. 174, no. 2, pp. 949–953, 2007.

[61] C. Delacourt, C. Wurm, L. Laffont, J. B. Leriche, and C. Masquelier, "Electrochemical and

electrical properties of Nb- and/or C-containing LiFePO4 composites," *Solid State Ionics*, vol. 177, no. 3–4, pp. 333–341, 2006.

[62] M. Gaberscek, R. Dominko, M. Bele, and M. Remskar, "Porous , carbon-decorated LiFePO 4 prepared by sol – gel method based on citric acid," *Solid State Ionics*, vol. 176, pp. 1801–1805, 2005.

[63] C. M. Burba and R. Frech, "Local structure in the Li-ion battery cathode material Lix(MnyFe1-y)PO4 for 0 < x ??? 1 and y = 0.0, 0.5 and 1.0," *Journal of Power Sources*, vol. 172, no. 2. pp. 870–876, 2007.

[64] C. H. Mi, X. G. Zhang, X. B. Zhao, and H. L. Li, "Synthesis and performance of LiMn0.6Fe0.4PO4/nano-carbon webs composite cathode," *Mater. Sci. Eng. B Solid-State Mater. Adv. Technol.*, vol. 129, no. 1–3, pp. 8–13, 2006.

[65] J. Moskon, R. Dominko, R. Cerc-Korosec, M. Gaberscek, and J. Jamnik, "Morphology and electrical properties of conductive carbon coatings for cathode materials," *J. Power Sources*, vol. 174, no. 2, pp. 683–688, 2007.

[66] J. Wolfenstine, J. Read, and J. L. Allen, "Effect of carbon on the electronic conductivity and discharge capacity LiCoPO4," *J. Power Sources*, vol. 163, no. 2, pp. 1070–1073, 2007.

[67] J. Ma and Q. Qin, "Electrochemical performance of nanocrystalline LiMPO 4 thin-films prepared by electrostatic spray deposition," *J. Power Sources*, vol. 148, pp. 66–71, 2005.

[68] J. Yao *et al.*, "Characterisation of olivine-type LiMnxFe1-xPO4 cathode materials," *J. Alloys Compd.*, vol. 425, no. 1–2, pp. 362–366, 2006.

[69] M. V. V. M. S. Kishore and U. V Varadaraju, "Influence of isovalent ion substitution on the electrochemical performance of LiCoPO 4," *Mater. Res. Bul.*, vol. 40, pp. 1705–1712, 2005.

[70] J. Wolfenstine, "Electrical conductivity of doped LiCoPO4," *J. Power Sources*, vol. 158, no. 2 SPEC. ISS., pp. 1431–1435, 2006.

[71] A. Yamada *et al.*, "Olivine-type cathodes: Achievements and problems," *J. Power Sources*, vol. 119–121, pp. 232–238, 2003.

[72] J. M. Tarascon and M. Armand, "Issues and challenges facing rechargeable lithium batteries," *Nature*, vol. 414, no. 6861, pp. 359–367, 2001.

[73] P. Health and M. Complete, "Water at hydrophobic surfaces : Weak hydrogen bonding and strong orientation effects," *Science (80-.).*, vol. 292, no. May, pp. 908–913, 2001.

[74] D. E. Irish, “Infrared and Raman Spectroscopic Studies of Solid Alkali Metal Nitrites,” no. 23, 1970.

[75] C. M. Burba and R. Frech, “Vibrational spectroscopic investigation of structurally-related LiFePO4, NaFePO4, and FePO4compounds,” *Spectrochim. Acta - Part A Mol. Biomol. Spectrosc.*, vol. 65, no. 1, pp. 44–50, 2006.

[76] A. Fujita, F. Isobe, T. Kodera, and T. Ogihara, “Synthesis and Electrochemical Properties of C/$LiMnPO_4$ Cathode Materials by Complex Polymerized Method,” *Key Eng. Mater.*, vol. 485, pp. 115–118, 2011.

[77] G. Yang, C. Sau, W. Lai, J. Cichon, and W. Li, “Non-linear infrared spectroscopy of the water bending mode: Direct experimental evidence of hydration shell reorganization?,” *HHS Public Access*, vol. 344, no. 6188, pp. 1173–1178, 2015.

[78] S. K. Martha *et al.*, “LiMnPO[sub 4] as an Advanced Cathode Material for Rechargeable Lithium Batteries,” *J. Electrochem. Soc.*, vol. 156, no. 7, p. A541, 2009.

[79] D. Fujimoto, N. Kuwata, Y. Matsuda, J. Kawamura, and F. Kang, “Fabrication of solid-state thin-film batteries using LiMnPO4thin films deposited by pulsed laser deposition,” *Thin Solid Films*, vol. 579, no. February, pp. 81–88, 2015.